Bielefeld University
Faculty of Physics

Investigation of Néel-order spin-orbit torque switching in dc-sputtered CuMnAs thin films and identification of a parasitic contribution in the electrical readout

Doctoral Dissertation in Physics
Tristan Matalla-Wagner

Advisor:
Prof. Dr. Markus Meinert

2$^{\text{nd}}$ referee:
Prof. Dr. Thomas Huser

July 4, 2021

UNIVERSITÄT BIELEFELD
FAKULTÄT FÜR PHYSIK

Hiermit erkläre ich, dass die vorliegende Dissertation von mir persönlich verfasst wurde. Einige Textpassagen und Abbildungen sind in abgewandelter Form aus von mir erstellten Publikationen übernommen. Ich habe keine anderen Quellen als die angegebenen benutzt und habe die Stellen der Arbeit, die anderen Werken entnommen sind – einschließlich verwendeter Tabellen und Abbildungen – unter Angabe der Quelle als Entlehnung kenntlich gemacht.

Bielefeld, 4. Juli 2021

(Tristan Matalla-Wagner)

> „So eine Arbeit wird eigentlich nie fertig, man muß sie für fertig erklären, wenn man nach Zeit und Umständen das möglichste getan hat.“
>
> – *Johann Wolfgang von Goethe* [1]

Vorwort und Danksagung

Diese Arbeit ist eine Ausarbeitung zu meinen in den letzten drei Jahren gewonnenen Erkenntnissen über das elektrische Schalten von antiferromagnetischen dünnen Schichten mit speziellen Symmetrieeigenschaften. Auch wenn die Forschung zu diesem Thema bei Weitem nicht abgeschlossen ist, liefern meine Resultate erste fundamentale Bausteine zum Verständnis der physikalischen Mechanismen, die bei diesem Phänomen relevant sind. Im Geiste Goethes lässt sich daher sagen, dass nach Zeit und Umständen meine Promotion das angestrebte Ziel erreicht hat. Belegen lässt sich diese Aussage durch Veröffentlichungen, zu denen ich signifikante Beiträge [2, 3] erbracht habe, beziehungsweise deren Autor [4, 5] ich bin. Darüber hinaus habe ich in der Zeit dieser Promotion zu fünf weiteren Publikationen Zuarbeiten geleistet [6–10]. Die maßgeblich von mir entwickelte Methodik zur quantitativen Untersuchung des elektrischen Schaltens kann auch in Experimenten angewandt werden, die mittels Heterostrukturen möglicherweise beliebige Antiferromagneten manipulieren können. Aus diesem Grund ist zu erwarten, dass das in dieser Arbeit aufgebaute *Know How* auch in Zukunft Anwendung findet und förderlich für den wissenschaftlichen Fortschritt über den von mir untersuchten Spezialfall hinaus sein wird.

An dieser Stelle möchte ich mich bei meinem Doktorvater Prof. Dr. Markus Meinert für die außergewöhnlich umfangreiche Betreuung bedanken. Die wöchentlichen Gruppenbesprechungen sowie der bedarfsorientierte Austausch zu aktuellen experimentellen Ergebnissen und auftretenden Problemen haben den Verlauf dieser Promotion entschieden positiv beeinflusst. Des Weiteren bedanke ich mich bei Prof. Dr. Günter Reiss für die Finanzierung meiner Stelle, der Möglichkeit an internationalen Konferenzen teilzunehmen, die Bereitstellung von Laborgeräten und Verbrauchsmaterialien, als auch für Diskussionen über physikalische Fragestellungen. Bei Dr. Jan-Michael Schmalhorst möchte ich mich vor allem für kritische und meist sehr direkte Fragen bedanken, da diese mich stets dazu angehalten haben, meine Resultate zu hinterfragen und letztendlich zu korrekten Schlussfolgerungen zu gelangen. Für technische Hilfe bei der Umsetzung von Experimenten möchte ich mich bei Dr. Karsten Rott sowie dem gesamten Personal der mechanischen und elektronischen Werkstatt bedanken. Aggi Windmann danke ich für die Unterstützung bei administrativen Aufgaben. Weiterhin möchte ich mich bei allen aktiven und ehemaligen Promovierenden, Masteranden und Bacheloranden für das angenehme Arbeitsklima und die gehaltvollen Diskussionen, insbesondere zur mittäglichen Kaffeepause, bedanken. Das „Logo“ auf dem Deckblatt dieser Arbeit wurde von Jan Krieft entworfen, wofür ich ebenfalls sehr dankbar bin.

Abschließend möchte ich meiner Dankbarkeit gegenüber Freunden und Familie, insbesondere meinen Eltern Alfons und Christiane, besonderen Platz einräumen. Ohne ihre konsequente und bedingungslose Unterstützung im Studium hätte ich diese Promotion wohl nicht begonnen und mein Lebensweg wäre ein anderer.

Zum leichteren Verständnis für Leserinnen und Leser außerhalb des deutschsprachigen Raumes sowie zur Steigerung der internationalen Sichtbarkeit, ist der Textkörper dieser Dissertation auf Englisch verfasst.

Publications included in this thesis

- *Electrical Néel-Order Switching in Magnetron-Sputtered CuMnAs Thin Films*
  T. Matalla-Wagner, M.-F. Rath, D. Graulich, J.-M. Schmalhorst, G. Reiss, and M. Meinert
  Phys. Rev. Appl., 12(6):064003, 2019
  DOI: `https://doi.org/10.1103/PhysRevApplied.12.064003`

- *Resistive contribution in electrical-switching experiments with antiferromagnets*
  T. Matalla-Wagner, J.-M. Schmalhorst, G. Reiss, N. Tamura, and M. Meinert
  Phys. Rev. Research, 2(3):033077, 2020
  DOI: `https://doi.org/10.1103/PhysRevResearch.2.033077`

Conference contributions

- *Current induced Néel-order switching in antiferromagnetic CuMnAs deposited by magnetron sputtering*
  T. Matalla-Wagner, M. Rath, J.-M. Schmalhorst, G. Reiss, and M. Meinert
  DPG Frühjahrstagung, Regensburg (2019), Talk, MA 4.12

- *Current induced Néel-order switching in antiferromagnetic CuMnAs deposited by magnetron sputtering*
  T. Matalla-Wagner, J.-M. Schmalhorst, G. Reiss, and M. Meinert
  DPG Frühjahrstagung, Berlin (2018), Talk, MA 54.3

- *Key role of thermal activation in electrical Néel-order switching of antiferromagnets*
  T. Matalla-Wagner, D. Graulich, G. Reiss, and M. Meinert
  62nd Annual Conference on Magnetism and Magnetic Materials, Pittsburgh (2017), Talk, HB-07

- *Thin films of the room temperature antiferromagnet CuMnAs deposited by magnetron sputtering*
  T. Matalla-Wagner, D. Linsen, J.-M. Schmalhorst, T. Kuschel, M. Meinert, and G. Reiss
  DPG Frühjahrstagung, Dresden (2017), Poster, MA 64.31

Contents

Introduction 1

The phenomenon investigated in this doctoral thesis is a part of the new research field called *antiferromagnetic spintronics*. This subcategory of the well-established field of *spintronics* has generated a large interest among the magnetism community up to the point where *Nature Physics* dedicated its March 2018 issue to that topic [11, 12]. To outline why this field is of high interest for contemporary science it is important to follow the history of antiferromagnets and their domain in spintronics and information technology, respectively.

Brief history of antiferromagnets in information technology

In 1932 Louis Néel, who was awarded the Nobel prize in physics in 1970 [13], published an article where he points out that systems may exist in which an antiparallel ordering of neighboring spins minimizes the total energy [14]. Antiparallel ordered spins do not generate a macroscopic magnetization which makes the interaction with an antiferromagnet, and therefore the detection of its magnetic state as well, nontrivial. Hence, the experimental validation of Néel's prediction took roughly a decade and was eventually validated by a local probe neutron scattering experiment in 1942 [15].

The relevance of antiferromagnets for applications became evident in 1956 after the discovery of the exchange bias effect [16, 17]. Exchange bias describes an induced anisotropy in a ferromagnet that couples to an adjacent antiferromagnet, enhancing the coercivity of the ferromagnet. However, if the induced anisotropy is unidirectional the ferromagnet establishes a magnetic easy direction. The coupling phenomena is an interface effect and, thus, has only a significant magnitude in thin film devices and nanoparticles. It allows the engineering of multilayer systems in which magnetically separated ferromagnets have arbitrary easy directions or where one layer's magnetization is significantly harder to rotate. These properties can be used to build magnetoresistive sensors or information storage devices with precisely tunable characteristics. Hence, antiferromagnets are widely spread in modern information technology and have, contrary to the initial conception of the pioneering scientists, an immense value for practical applications [18–20].

In magnetoresistive devices with exchange bias the antiferromagnet is a crucial component but it remains a passive element. It is configured by the fabrication process and remains invariant during normal operation of the device. The research field of *antiferromagnetic spintronics* is a step forward and utilizes the antiferromagnet as active element in which information can be stored. The concept of writing information directly into an antiferromagnet has multiple benefits compared to a ferromagnetic memory [12]:

1. Antiferromagnets have no net magnetization
   → robustness against perturbations and no stray field
   → high memory cell density possible

2. Antiferromagnetic magnetization dynamics are much faster compared to ferromagnetic dynamics
   → faster writing speed possible

3. Certain read & write mechanisms do not require heterostructures
   → (in principle) easy to fabricate

While the lack of a net magnetization in an antiferromagnet provides substantial benefits in regard of information storage technologies, it also restricts possibilities to manipulate its properties.

A new mechanism to manipulate the antiferromagnetic state, also referred to as Néel order, was proposed by Železný *et al.* in 2014 [21]. The predicted Néel-order spin-orbit torque occurs if an electrical current is driven through an antiferromagnet that obeys specific symmetry requirements. It allows to electrically reorient the Néel order, i.e., switch between different stable antiferromagnetic states. In 2016 the feasibility to rotate the Néel order using electrical currents has been validated experimentally by Wadley *et al.* in a tetragonal CuMnAs thin film which was grown by molecular beam epitaxy [22]. The possibility, to reorient the Néel order electrically in a single layer of antiferromagnetic material, paves the way to design an antiferromagnetic memory device retaining the advantages emphasized above.

Thesis outline

As outlined above it has been proven already that an electrical current passing trough a CuMnAs thin film of high crystalline quality rotates the Néel order. However, the fabrication of antiferromagnetic memory devices by molecular beam epitaxy is not feasible for a large scale production. Thus, the first question that will be answered within this thesis is whether tetragonal CuMnAs thin films can be grown in sufficient quality, using dc-magnetron sputtering as well [cf. Sec. 4.1].

Secondly, the Néel-order spin-orbit torque is investigated using intense currents pulses that manipulate the Néel order in those sputtered samples of tetragonal and highly oriented, but nonepitaxial, CuMnAs films. The switching is examined with a focus on the effect of successive pulsing and the time stability of the switched state [cf. Sec. 4.2]. Deviations from Železný's prediction are analyzed using a thermal activation model [cf. Sec. 4.3] and the switching is simulated by a Monte Carlo code [cf. Sec. 4.4], eventually drawing a consistent picture of the switching mechanism that goes significantly beyond the initial proposed theory.

Finally, this thesis questions whether the high current densities, necessary to observe Néel-order spin-orbit torque switching, induce effects of nonmagnetic origin that superpose with the magnetic response in transport experiments. The experimental investigation is done by microdiffraction experiments on reference systems. Then, the findings obtained from those experiments are used to create a numerical model using the Finite-Element-Method which allows the determination of the nonmagnetic contribution in a Néel-order spin-orbit torque switching experiment [cf. Chap. 5].

Chap. 2, placed prior to the presentation and discussion of the experimental results of this work, serves to convey basic knowledge about magnetism and the Néel-order spin-orbit torque theory. The experimental methods are described in Chap. 3.

The findings imparted in Chap. 4 and 5 are summarized in their respective summary sections 4.5 and 5.6 separately and consolidated in Chap. 6 to display a coherent conclusion of this work.

Other directions of antiferromagnetic spintronics

Electrical switching by the Néel-order spin-orbit torque is limited to antiferromagnets that follow a very specific symmetry and, up to now, only two materials have been identified to fulfill those requirements. Although this thesis focuses especially on the Néel-order spin-orbit torque it is important to note that within the *antiferromagnetic spintronics* community other means to electrically rotate the Néel order have been discovered as well [23].

One mechanism I would like to highlight in particular is the rotation of the Néel order in bilayer systems of the type antiferromagnet / heavy metal. The typically strong spin-orbit interaction in heavy metals can be used to electrically generate a spin-orbit torque in the antiferromagnet which drives the magnetization dynamics. The spin current generating that spin-orbit torque is created solely in the heavy metal and, thus, allegedly any antiferromagnet / heavy metal system with sufficiently spin-transparent interface should be switchable. This becomes especially interesting since this also works with insulation antiferromagnets, such as NiO [24, 25]. The thermal activation physics that is essential for Néel-order spin-orbit torque switching, as pointed out by this thesis, is relevant for this spin-orbit torque induced switching as well [3]. Hence, the results of this work finds broad application within the *antiferromagnetic spintronics* community.

Fundamentals 2

This chapter starts with a basic introduction into magnetism. The given information is well known to the condensed matter community and can be found in several textbooks [26–31]. Still, I intent to establish a common ground of knowledge and a distinct nomenclature regarding the physics that is of relevance within this thesis. Throughout Sec. 2.1, information that cannot be found in one of the cited textbooks are referenced individually. If more specialized literature was used for a certain text passage, although the information could be found in one of the mentioned textbooks as well, the reference is given anyway at the appropriate position.

Theoretical predictions that motivate my experimental work, and extensions of this description developed in the course of this dissertation, will be discussed in Sec. 2.2 and 2.3.

2.1 Magnetism

A commonly used method to partition materials regarding their magnetic properties is to divide them into two groups, nonmagnetic and magnetic. In fact, however, all materials show a response if exposed to a magnetic field $\boldsymbol{H}$. This feedback can be described by the magnetic flux density

$$\boldsymbol{B} = \mu_0 \left(\boldsymbol{M} + \boldsymbol{H} \right) \tag{2.1}$$

with the vacuum permeability $\mu_0 = 4\pi \times 10^{-7}\,\mathrm{N/A^2}$ and magnetization

$$\boldsymbol{M} = \chi \, \boldsymbol{H}. \tag{2.2}$$

The magnetic susceptibility χ is a dimensionless quantity that characterizes the magnetic response. Due to the superposition of different forms of magnetism it is not always visible, but a fundamental physical property of all matter is to be diamagnetic. Purely diamagnetic materials are characterized by $-1 \leq \chi < 0$ and, thus, $\boldsymbol{M} \upharpoonleft\downharpoonright \boldsymbol{H}$. $\chi = -1$ describes perfect diamagnetism which occurs in superconductors. Paramagnetic materials are characterized by $\chi > 0$. There are various forms of paramagnetism, i.e. Langevin-, Pauli-, and Van-Vleck-paramagnetism. Langevin-paramagnetism has its root in the magnetic moments of atoms. Pauli-paramagnetism originates from the magnetic moments carried by the conduction electrons and Van-Vleck-paramagnetism is caused by exited atoms. Regarding their relative contribution, to the total paramagnetic behavior of a material, the Langevin-paramagnetism is by far the most relevant. Hence, the following passage will focus on Langevin-paramagnetism exclusively. Langevin-paramagnetic materials possess uncoupled permanent magnetic dipole moments $\boldsymbol{m}$ that can minimize their energy by aligning parallel to an external magnetic field. The resulting magnetization

$$\boldsymbol{M} = \frac{1}{V} \sum_{i}^{N} \boldsymbol{m}_i = \frac{N}{V} \langle \boldsymbol{m} \rangle \tag{2.3}$$

is the sum over the mean orientation of those N moments per Volume V. The alignment $\boldsymbol{M} \parallel \boldsymbol{H}$ is countered by the thermal fluctuations with an energy scale of $k_B T$, which leads to Curie's law

$$\chi = \frac{C}{T} \tag{2.4}$$

with the material specific Curie constant $C > 0$ and, hence, $\chi > 0$. At low temperatures the thermal fluctuations become negligible which means that all $\boldsymbol{m}_i$ are parallel. Consequently, the magnetization $|\boldsymbol{M}|$ saturates at a finite value. Eq. (2.4) does not capture this effect and is, therefore, not applicable for low T.

If exclusively those forms of magnetism are present in a material, it is labeled as nonmagnetic, which means that a spontaneous magnetic order is absent and no magnetization is observed without an external magnetic field.

2.1.1 Collective magnetism

In contrast, in magnetic materials the permanent magnetic moments are coupled and, therefore, form a spontaneous magnetic order. This coupling primarily results from the exchange interaction which is due to the overlap of wave functions ψ of indistinguishable particles. This interaction is described by the exchange integral

$$J = \int \psi_a^*(\boldsymbol{r}_1)\psi_b^*(\boldsymbol{r}_2)\, \hat{\mathcal{H}}\, \psi_a(\boldsymbol{r}_2)\psi_b(\boldsymbol{r}_1)\, \mathrm{d}\boldsymbol{r}_1 \mathrm{d}\boldsymbol{r}_2 \tag{2.5}$$

where the Hamiltonian $\hat{\mathcal{H}}$ contains the quantum mechanical origin of this interaction. The resulting exchange constant J includes the information that the total wave function of fermions, e.g. electrons, has to be antisymmetric following the Pauli exclusion principle. This can be realized by either an antisymmetric spatial wave function or an antisymmetric spin wave function. It manifests in J being positive or negative. Which configuration is energetically favorable depends on the individual system. J will be used in the following without going into detail regarding its quantum mechanical origin. In the Heisenberg model, the exchange energy

$$E_{\mathrm{xc}}^{1,2} = -2\,J\,\boldsymbol{s}_1 \cdot \boldsymbol{s}_2 \tag{2.6}$$

of two localized spins $\boldsymbol{s}_1$ and $\boldsymbol{s}_2$ is given by the relative orientation of the interacting spins and their exchange constant. The spins minimize their energy by ordering parallel if $J > 0$ and antiparallel if $J < 0$. For a single spin $\boldsymbol{s}$, e.g. embedded in the crystal lattice of a solid, its exchange energy depends on the interaction with all other spins. If only the interaction with the nearest neighbors is considered the exchange energy becomes:

$$E_{\mathrm{xc}} = -2J \sum_{j=1}^{z} \boldsymbol{s} \cdot \boldsymbol{s}_j \tag{2.7}$$

Here, z is the number of nearest neighbors that are assumed to have an identical exchange constant J. Typical values for the exchange energy are in the order of $E_{\mathrm{xc}} = 10\ldots100\,\mathrm{meV}$ [26]. Fe for example has an exchange energy[1] of $E_{\mathrm{xc}}^{\mathrm{Fe}} \approx 17\,\mathrm{meV}$. With a lattice constant of $2.86\,\mathrm{Å}$ [27] and 2 atoms per unit cell this calculates to an exchange energy density of

$$\frac{2 \cdot E_{\mathrm{xc}}^{\mathrm{Fe}}}{\left(2.86\,\mathrm{Å}\right)^3} \approx 200\,000\,\frac{\mathrm{kJ}}{\mathrm{m}^3}. \tag{2.8}$$

The phenomenon of collective magnetism is partitioned into ferro-, ferri- and antiferromagnetism to classify the different ordering types of spins. In a ferromagnet (FM) the moments couple to favor a parallel orientation, as seen in Fig. 2.1 (a), which allows for a magnetization at zero magnetic field. In the ferromagnetic state an expression for χ cannot be found analytically and, thus, the phenomenological differential susceptibility

$$\chi = \frac{\partial M}{\partial H} \tag{2.9}$$

is used, whereas $M = |\boldsymbol{M}|$ and $H = |\boldsymbol{H}|$. Magnetizations in FMs are usually large compared to other forms of magnetism which concludes to $\chi \gg 0$ in most circumstances. In antiferromagnets (AFMs) and ferrimagnets (FiMs) the moments align antiparallel. To highlight the difference, it is

---

[1] Estimated by mean-field theory with $T_C = 1044\,\mathrm{K}$ and $|\boldsymbol{m}| = 2.22\,\mu_B$ [26].

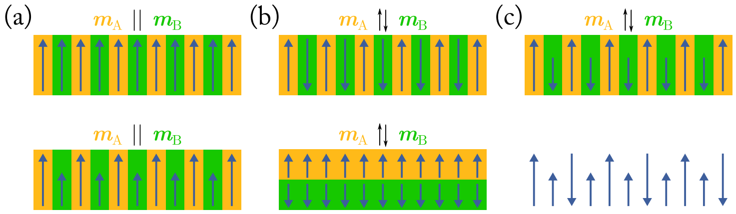

Figure 2.1: Illustration of collective magnetism with different ordering. (a) All magnetic moments are ordered parallel in FMs. (b) In AFMs the moments compensate each other by ordering antiparallel and, thus, have zero net magnetization. (c) FiMs show (fractional) antiparallel ordering but without full compensation of moments. Figure inspired by Ref. [26].

handy to divide the magnetic order into two sublattices A and B which are ferromagnetic if examined separately. Hence, the moments of each sublattice can be described by a single magnetic moment $\boldsymbol{m}_\mathrm{A}$ and $\boldsymbol{m}_\mathrm{B}$, respectively [cf. Fig. 2.1 (b), (c)]. In AFMs the magnitude of each sublattices moments is equal which results in a vanishing net magnetization. This magnetically highly ordered state is called the Néel order and is described by the Néel vector

$$\boldsymbol{L} = \boldsymbol{m}_\mathrm{A} - \boldsymbol{m}_\mathrm{B}. \tag{2.10}$$

The susceptibility of an AFM depends on the relative orientation of $\boldsymbol{L}$ and $\boldsymbol{H}$. It is small due to the strong exchange interaction of neighboring moments that enforces an antiparallel orientation. $\chi_\perp > 0$ results from a canting of the magnetic moments and is independent of the temperature while $\chi_\parallel$, with $0 \leq \chi_\parallel \leq \chi_\perp$, is not. The temperature dependence of $\chi_\parallel$ originates from thermally induced fluctuation in the antiparallel ordering and, thus, $\chi_\parallel\,(T = 0\,\mathrm{K}) = 0$. FiMs can have an arbitrary order of moments but with some of them being antiparallel to each other which includes an AFM like order but with $|\boldsymbol{m}_\mathrm{A}| \neq |\boldsymbol{m}_\mathrm{B}|$. They behave similar to FMs regarding their response to an external magnetic field. This classification of magnetic materials suffices to acknowledge the important differences. However, note that more complex spin configurations that go beyond this simplistic view, like chiral spin structures, exist in nature as well.

Likewise to paramagnetism, the coupling of moments that results in collective magnetism competes against the temperature. As consequence, there is a critical temperature above which the spontaneous order collapses and the material becomes paramagnetic. For FMs and FiMs this temperature is called Curie temperature T_C, for AFMs it is called Néel temperature

T_N. High transition temperatures T_C and T_N result from a strong exchange interaction.

2.1.2 Magnetic anisotropy

Physical systems will always minimize their total energy E_{tot}, if possible and not countered by temperature. Regarding a ferri- or ferromagnetic material of volume V the energies that can be minimized by a change of the magnetic orientation add up to

$$E_{\text{tot}} = E_{\text{Zeeman}} + E_{\text{ani}} \tag{2.11}$$

with the Zeeman energy

$$E_{\text{Zeeman}} = -\mu_0 \int_V \mathrm{d}V \boldsymbol{M} \cdot \boldsymbol{H} \tag{2.12}$$

and the anisotropy energy

$$E_{\text{ani}} = E_{\text{shape}} + E_{\text{mc}} + E_{\text{ind}} + \ldots . \tag{2.13}$$

E_{Zeeman} results from the dipolar interaction of the magnetic moment with $\boldsymbol{H}$ and is minimized for $\boldsymbol{M} \parallel \boldsymbol{H}$. Its magnitude depends on the material and the magnetic field strength. For Fe with a magnetization $|\boldsymbol{M}| = 1750\,\text{kA/m}$ [26] in a magnetic field of $\mu_0\,|\boldsymbol{H}| = 1\,\text{T}$ the Zeeman energy density reads $\pm 1750\,\text{kJ/m}^3$. Therefore, the possible gain in energy density by aligning with the external field is $3500\,\text{kJ/m}^3$ in this example.

E_{ani} consists of various contributions. The explicitly given E_{shape}, E_{mc} and E_{ind} are the shape, magnetocrystalline and induced anisotropy energy, respectively. Their origin will be discussed in the following subsections. Note that the anisotropy energy E_{ani} can be represented as the so called anisotropy field $\boldsymbol{H}_{\text{ani}}$ which translates to an energy via Eq. (2.12). In many cases it is more convenient to use $\boldsymbol{H}_{\text{ani}}$ instead of E_{ani}.

2.1.2.1 Shape anisotropy

The root of E_{shape} can be found in the stray field $\boldsymbol{H}_{\text{stray}}$ emitted by a magnetized material. $\boldsymbol{H}_{\text{stray}}$ holds the energy

$$E_{\text{stray}} = \frac{\mu_0}{2} \int_{\text{outside}} \mathrm{d}V \boldsymbol{H}_{\text{stray}}^2 \tag{2.14}$$

where the spatial appearance of $\boldsymbol{H}_{\text{stray}}$, and therefore E_{stray}, depends on $\boldsymbol{M}$ and the shape of the material. The shape anisotropy energy E_{shape} is the maximum difference of $E_{\text{stray}}(\boldsymbol{M})$ one can find for a given shape. For a thin film, these extrema are found for $\boldsymbol{M}$ being out of plane (oop) or in plane (ip). Hence,

$$E_{\text{shape,film}} = E_{\text{stray}}(\boldsymbol{M} \parallel \hat{\boldsymbol{n}}) - E_{\text{stray}}(\boldsymbol{M} \perp \hat{\boldsymbol{n}}) \approx \frac{\mu_0}{2} \int_V \mathrm{d}V \boldsymbol{M}^2 \tag{2.15}$$

is obtained which results in $K_{\text{shape,film}} \approx 400\,\mathrm{kJ/m^3}$ for a magnetization of $\mu_0 |\boldsymbol{M}| = 1\,\mathrm{T}$. $\hat{\boldsymbol{n}}$ is the normal vector of the film.

2.1.2.2 Magnetocrystalline anisotropy

The magnetocrystalline anisotropy energy E_{mc} links the crystallographic structure of a material to magnetic easy and hard axes or planes, respectively. The coupling mechanism between the magnetic order and the crystal lattice is based on the spin-orbit interaction (SOI) which gives rise to an energy contribution

$$E_{\text{so}} = \lambda \, (\boldsymbol{\ell} \cdot \boldsymbol{s}) \tag{2.16}$$

that depends on the angle between an electron's angular momentum $\boldsymbol{\ell}$ and its spin $\boldsymbol{s}$. λ is the spin-orbit coupling constant containing information of the electron's quantum numbers and its radial wave function.

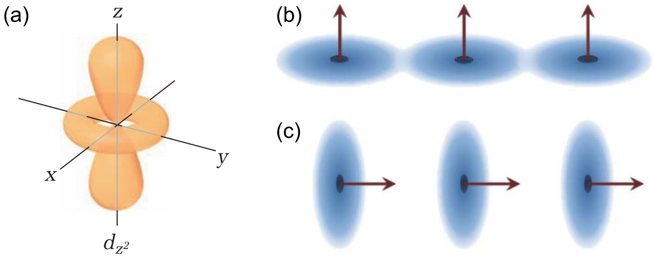

FIGURE 2.2: (a) Contour plot of the atomic orbital with quantum numbers $n = 3$, $\ell = 2$ and $m = 0$. (b) The blue areas depict a nonspherical electron distribution and the arrows represent the orientation of the respective angular momentum vector $\boldsymbol{\ell}$. (c) A rotation of $\boldsymbol{\ell}$ leads to a rotation of the electron distribution which can reduce their overlap. Figure merged from Ref. [32] (a) and Ref. [26] (b) & (c).

The spatial extension of an atom's localized electrons is described by the atomic orbitals. The shape of an orbital is determined by the main, orbital and magnetic quantum number n, ℓ and m, respectively. In Fig. 2.2 (a) an illustration of a d-orbital ($\ell = 2$) with magnetic quantum number $m = 0$ is shown. This orbital, and all orbitals with $l \neq 0$, do not obey spherical symmetry. Their orientation depend on the direction of $\boldsymbol{\ell}$ which is sketched in Fig. 2.2 (b) & (c). Hence, a lattice of atoms with atomic orbitals that are non-spherical has configurations with minimal orbital overlap and, therefore, minimal energy. Those configurations correspond to a preferred orientation of $\boldsymbol{\ell}$ and, thus, of $\boldsymbol{s}$.

The coupling mechanism acts on individual atoms and results in easy axes or planes where the energies for $\pm\boldsymbol{s}$ are identical. Therefore, the deduction is valid for FMs and AFMs alike. For AFMs with collinear sublatties E_mc can be translated into an anisotropy field $\boldsymbol{H}_\mathrm{mc}$ via Eq. (2.12) analog to FMs by replacing $\boldsymbol{M}$ with $\boldsymbol{L}$.

A phenomenological description of magnetocrystalline anisotropies can be established by the expansion of

$$\frac{E_\mathrm{mc}}{V} = K_\mathrm{mc} = K_0 + \sum_{i=1}^{\infty} K_i\, f_i(\boldsymbol{m}) \tag{2.17}$$

into a series of functions $f_i(\boldsymbol{m})$ and coefficients K_i. The $f_i(\boldsymbol{m})$ depend on the orientation of the magnetic moment $\boldsymbol{m}$ and the crystallography of the respective system. For a uniaxial symmetry Eq. (2.17) becomes

$$K_\mathrm{mc}^\mathrm{uni} = K_0^\mathrm{uni} + K_1^\mathrm{uni} \sin^2 \vartheta + K_2^\mathrm{uni} \sin^4 \vartheta + \dots \tag{2.18}$$

with ϑ being the angle between $\boldsymbol{m}$ and the anisotropy axis. In case of a cubic symmetry Eq. (2.17) reads:

$$\begin{aligned} K_\mathrm{mc}^\mathrm{cub} = K_0^\mathrm{cub} &+ K_1^\mathrm{cub} \left(m_x^2 m_y^2 + m_y^2 m_z^2 + m_z^2 m_x^2\right) \\ &+ K_2^\mathrm{cub} \left(m_x^2 m_y^2 m_z^2\right) + \dots \end{aligned} \tag{2.19}$$

A visualization of the three dimensional energy landscape given by Eqs. (2.18) and (2.19) is shown in Fig. 2.3. A uniaxial anisotropy can create either a magnetic easy axis or a magnetic easy plane if $K_\mathrm{mc}^\mathrm{uni} < 0$ or $K_\mathrm{mc}^\mathrm{uni} > 0$, respectively. A cubic anisotropy leads to three or four easy axes dependent on the sign of $K_\mathrm{mc}^\mathrm{cub}$ [cf. Fig. 2.3 (c) & (d)]. Different types of magnetocrystalline anisotropies can occur simultaneously. In a tetragonal system for example, the anomalous axis c would typically induce a uniaxial anisotropy. This anisotropy can lead to an easy axis that dominates other contributions to E_mc. Alternatively, the uniaxial anisotropy can enforce a magnetic easy

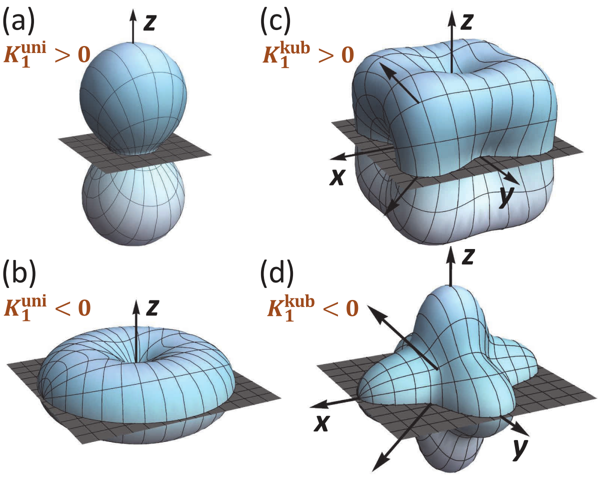

FIGURE 2.3: The contour plots show surfaces of constant magnetic energy density in dependence of the orientation of $\boldsymbol{m}$. Only contributions of first order are considered. In (a) & (b) Eq. (2.18) is used for the plot and the anisotropy axis is parallel to the z axis. A positive anisotropy constant results in an easy plane while a negative value leads to an easy axis. For (c) & (d) Eq. (2.19) is used and the easy axes are parallel to the basis vectors if K_1^{cub} is positive. If the sign of K_1^{cub} becomes negative the basis vectors become hard axes which results in four easy axes. Figure taken from Ref. [26].

plane. In this case a two-dimensional fourfold symmetry may superpose the easy plane. For $c \parallel z$ this can be described by Eq. (2.19) with $m_z = 0$ and results in the fourfold magnetocrystalline anisotropy energy density

$$\begin{aligned} K_{\text{mc}}^{\text{ff}} &= K_1^{\text{cub}} \left(m_x m_y\right)^2 && (2.20)\\ &= K_1^{\text{cub}} \left(m^2 \sin\varphi \cos\varphi\right)^2 && (2.21)\\ &= K_1^{\text{cub}} \frac{m^4}{4} \sin^2 2\varphi && (2.22)\\ &= K_{4\|} \sin^2 2\varphi && (2.23) \end{aligned}$$

with φ being the angle between $\boldsymbol{m}$ and one of the easy axes x or y. The constant offset K_0^{cub} has no physical relevance and can be omitted. $K_{4\|}$ summarizes all constant factors.

Typical magnetocrystalline anisotropy energy densities are in the order of $K_{\text{mc}} = 5 \ldots 800\,\text{kJ/m}^3$ [26].

2.1.2.3 Induced anisotropy

The induced anisotropy energy E_{ind} respects extrinsic contributions to the anisotropy arising from elastic deformation, strain, chemical disorder or exchange coupling. Its magnitude can be comparable to E_{mc} and E_{shape}. Induced anisotropies can affect FMs and AFMs.

2.1.3 Magnetic domains

A rectangular cuboid of magnetic material with homogeneous magnetization, shown in Fig. 2.4 (a), minimizes E_{stray} if $\boldsymbol{M}$ aligns with its long edge. E_{stray} can be further reduced by the formation of magnetic domains that are separated by the domain walls which on their part cost the energy E_{wall} [cf. Fig. 2.4 (b)-(d)]. Thus, the particular orientation of each individual magnetic moment $\boldsymbol{m}$ in a magnetic material is nontrivial. The energetic landscape associated to different arrangements of moments can have multiple local minima which give rise to a hysteresis in external field loops, as depicted in Fig. 2.5.

The lack of a net magnetization suggests that E_{shape} and E_{Zeeman} should be zero in AFMs. They are, however, small but nonzero due to uncompensated moments at the surfaces, interfaces, defects and induced ferromagnetic moments. Induced moments may result from thermal excitations or canting due to an external magnetic field. Nevertheless, the domain pattern of an AFM is primarily given by E_{mc}, E_{ind} and the granularity of the material. In contrast to the ferromagnetic order, the Néel order cannot be stabilized by long range dipole interactions that can overcome, e.g., grain boundaries. Naively this raises the expectation that the antiferromagnetic domain size is

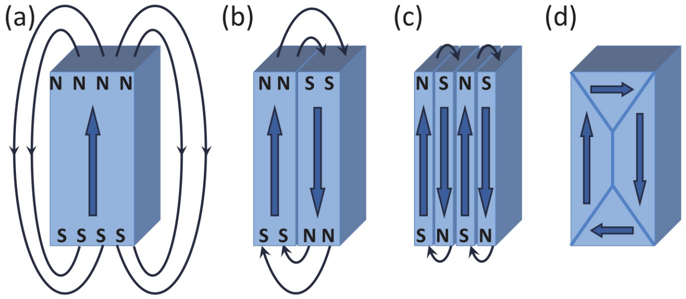

FIGURE 2.4: Formation of ferromagnetic domains. The stray field energy E_{stray} reduces from (a) to (d) while the domain wall energy increases. Figure taken from Ref. [26].

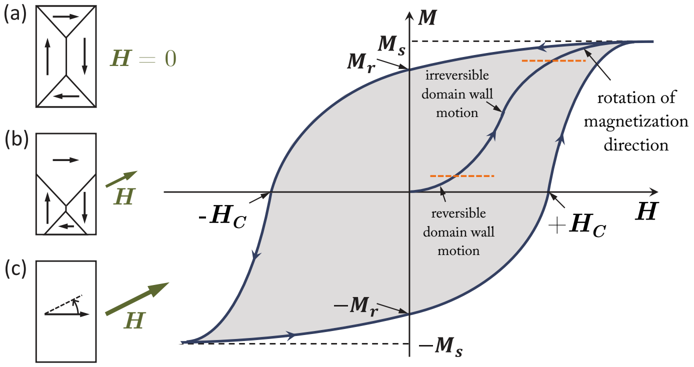

FIGURE 2.5: Magnetization curve of a ferromagnet in a magnetic field $\boldsymbol{H}$. (a) The loop stars at $\boldsymbol{M}(\boldsymbol{H} = 0) = 0$ which corresponds to a multidomain state with $E_{\text{stray}} \approx 0$. (b) Increasing $\boldsymbol{H}$ leads to a domain wall movement that enlarges the domain with lowest E_{Zeeman}. This movement is reversible for small fields but eventually becomes irreversible. (c) A single domain state is formed in which $\boldsymbol{M}$ is not fully aligned with $\boldsymbol{H}$. For high fields, $\boldsymbol{M}$ and $\boldsymbol{H}$ become parallel and the projection $\boldsymbol{M} \cdot \boldsymbol{H} = M_s$ is maximal. M_s is the saturation magnetization. Once the sample is magnetized and $\boldsymbol{H}$ is set to zero again, one obtains the remanent magnetization $|\boldsymbol{M}_r| \leq M_s$ being oriented to minimize E_{tot}. The field necessary to achieve $\boldsymbol{M}\,(\boldsymbol{H}_C) = 0$ is the the coercive field H_C with $\boldsymbol{H}_C \upharpoonleft\downharpoonright \boldsymbol{M}_r$. Figure adapted from Ref. [26].

limited by the crystallographic grain size of the AFM, which is true in most cases. Within a grain E_{mc} and E_{ind} determine the magnetic easy axes and planes. For thin film samples, E_{ind} can be tuned by varying the deposition conditions and, therefore, a desired magnetic anisotropy can be tailored.

The size limitation of an antiferromagnetic domain to the size of its hosting grain can be overcome by an indirect coupling mechanism. Grains that exhibit a collective magnetic order characterized by $\boldsymbol{M}$ or $\boldsymbol{L}$ elastically deform with usually constant volume due to the magnetostriction effect and, as consequence, can exert compressive strain to neighboring grains. If the distortion of a grain is countered, e.g., from a neighboring grain that deforms as well, the total energy is minimized by a rotation of $\boldsymbol{M}$ or $\boldsymbol{L}$ to relief the stress. Thus, this so called magnetoelastic coupling can facilitate antiferromagnetic domains that span over multiple grains where the change of $\boldsymbol{L}$ in one grain affects the others [33].

A final remark regarding the Néel order deals with the influence of $\boldsymbol{H}$ on $\boldsymbol{L}$. In the presence of a magnetic field the rotation of $\boldsymbol{L}$ has no effect on E_{tot} due to $\boldsymbol{M} = 0$. However, the canting of neighboring moments result in an induced magnetization $\delta\boldsymbol{M} \parallel \boldsymbol{H}$ leading to $E_{\mathrm{Zeeman}} < 0$ [c.f. Eq. (2.12)]. Likewise, the canting disrupts the antiparallel ordering which is adverse for E_{tot} and restricts $\delta\boldsymbol{M}$ to be small. The energy gain achievable through canting depends on the angle $\angle(\boldsymbol{H}, \boldsymbol{L})$ and is maximized for $\boldsymbol{H} \perp \boldsymbol{L}$. For $\boldsymbol{H} \parallel \boldsymbol{L}$, and $T = 0\,\mathrm{K}$, canting cannot decrease the total energy of the system. In this case, a rotation of $\boldsymbol{L}$ to facilitate canting can reduce E_{tot} which occurs at usually high magnetic fields. This so called spin-flop transition happens at the spin-flop field [34, 35]

$$H_{\mathrm{sf}} = \sqrt{\frac{2H_{\mathrm{xc}}H_{\mathrm{ani}}}{1 - \chi_{\parallel}/\chi_{\perp}}}. \tag{2.24}$$

H_{xc} is the exchange field and H_{ani} is the anisotropy field. Eq. (2.24) demands for $\chi_{\perp} > \chi_{\parallel}$ which is true if $T < T_N$. Hence, the divergence of Eq. (2.24) for $T \geq T_N$ and, therefore, $\chi_{\perp} = \chi_{\parallel}$, has no physical meaning.

2.1.4 Anisotropic magnetoresistance

There are plenty transport phenomena related to magnetic materials. Most of them are linear in $\boldsymbol{M}$ and, therefore, of minor interest for AFMs. This is especially true for this thesis since $\boldsymbol{H} = 0$ in all presented experiments. The anisotropic magnetoresistance (AMR), however, is quadratic with respect to each magnetic moments $\boldsymbol{m}$ and therefore correlates with the Néel order without the need of heterostructures [36, 37]. It describes the effect of the magnetic order on the electrical resistivity ρ. The orbitals of a magnetic atom with associated moment $\boldsymbol{m}$ are not spherically symmetric [cf. Sec. 2.1.2.2]. Hence, the scattering cross-section for the conduction electrons depends on the relative orientation of $\boldsymbol{m}$ and the electron flow direction. The effect is identical for $\pm\boldsymbol{m}$ and, thus, present in FMs, FiMs and AFMs. Macroscopically the orientation of the magnetic order is given by $\boldsymbol{M}$ or $\boldsymbol{L}$ and the electron flow direction is characterized by the electrical current density $\boldsymbol{j}$. The highest/lowest resistivities are found for $\boldsymbol{j}$ being parallel/perpendicular to $\boldsymbol{M}$ and $\boldsymbol{L}$, respectively. Hence, these extremum values are labeled as $\rho_{\parallel}$ and $\rho_{\perp}$. Typically one finds $\rho_{\parallel} > \rho_{\perp}$ for the AMR whereas the case $\rho_{\parallel} < \rho_{\perp}$ is regarded as anomalous.

To establish a macroscopic mathematical description of the AMR I will adapt the derivation from Thompson *et al.* [38, 39]. We consider a two dimensional magnetic material, sketched in Fig. 2.6, with all quantities being in plane (ip). $\boldsymbol{j} = (j, 0)^{\intercal}$ defines the reference axis and the arrangement of magnetic moments is characterized by $\theta = \angle(\boldsymbol{j}, \boldsymbol{L}) = \angle(\boldsymbol{j}, \boldsymbol{M})$ for AFM

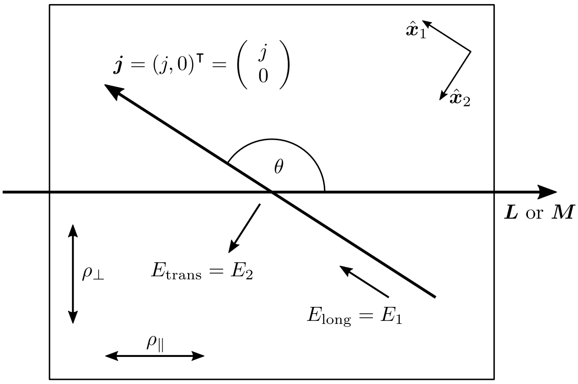

FIGURE 2.6: Schematic of the electrical fields resulting from the AMR. The coordinate system with base $\hat{\boldsymbol{x}}_1$ and $\hat{\boldsymbol{x}}_2$ is defined by the current density direction $\boldsymbol{j}$. Different resistivities for $\boldsymbol{j}$ being parallel or perpendicular to the magnetic order, characterized by $\boldsymbol{L}$ or $\boldsymbol{M}$, give rise to electrical fields that are longitudinal E_{long} and transverse E_{trans} to $\boldsymbol{j}$ as derived in the text.

and FM/FiM, respectively. The electrical field

$$\boldsymbol{E} = \tilde{\boldsymbol{\rho}}\,\boldsymbol{j} \tag{2.25}$$

follows Ohm's law with the resistivity tensor $\tilde{\boldsymbol{\rho}}$. Knowing how ρ depends on the relative orientation of the magnetic order and $\boldsymbol{j}$, we can write

$$\tilde{\boldsymbol{\rho}} = \tilde{\boldsymbol{R}}(\theta) \begin{pmatrix} \rho_{||} & 0 \\ 0 & \rho_\perp \end{pmatrix} \tilde{\boldsymbol{R}}(-\theta) \tag{2.26}$$

using the rotation matrix

$$\tilde{\boldsymbol{R}}(\theta) = \begin{pmatrix} \cos\theta & -\sin\theta \\ \sin\theta & \cos\theta \end{pmatrix} \tag{2.27}$$

and obtain

$$\boldsymbol{E} = \begin{pmatrix} \rho_{||}\cos^2\theta + \rho_\perp \sin^2\theta & \cos\theta\sin\theta\left(\rho_{||} - \rho_\perp\right) \\ \cos\theta\sin\theta\left(\rho_{||} - \rho_\perp\right) & \rho_\perp\cos^2\theta + \rho_{||}\sin^2\theta \end{pmatrix} \begin{pmatrix} j \\ 0 \end{pmatrix} \tag{2.28}$$

$$= j \begin{pmatrix} \rho_{||}\cos^2\theta + \rho_\perp \sin^2\theta \\ \cos\theta\sin\theta\left(\rho_{||} - \rho_\perp\right) \end{pmatrix}. \tag{2.29}$$

The electric field longitudinal to $\boldsymbol{j}$ becomes

$$E_{\text{long}} = E_1 = j\,\left[\rho_\perp + \left(\rho_{||} - \rho_\perp\right)\cos^2\theta\right] \tag{2.30}$$

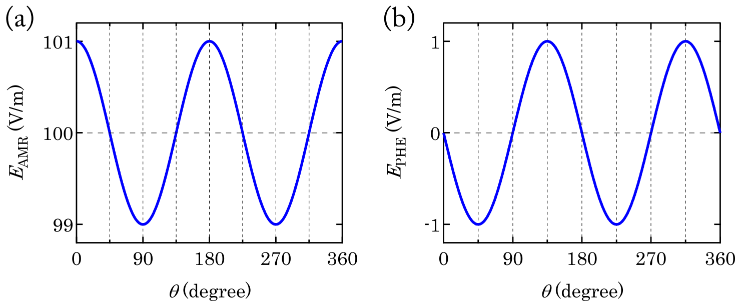

FIGURE 2.7: Simulation of the angular dependence of (a) AMR and (b) planar Hall effect (PHE) for perfectly arranged contacts. The data is calculated using Eqs. (2.30) and (2.31) with the parameters $j = 1\,\mathrm{A/m^2}$, $\rho = 100\,\Omega\mathrm{m}$ and $\Delta\rho/\rho = 2\%$. The curves show a phase shift by $\pi/4$ with respect to each other and have twofold symmetry. (a) The AMR occurs on top of an ohmic contribution which is adverse regarding the experimental realization. (b) The PHE is by design symmetric around zero.

using the identity $\sin^2\theta + \cos^2\theta = 1$ and the transversal component resolves to

$$E_{\mathrm{trans}} = E_2 = j\,\sin 2\theta\,\frac{\rho_{\parallel} - \rho_{\perp}}{2} \tag{2.31}$$

with $2\cos\theta\sin\theta = \sin 2\theta$. Typically, the longitudinal component is associated with the term AMR while the transverse component is commonly known as PHE. Hence, the nomenclature $E_{\mathrm{AMR}} = E_{\mathrm{long}}$ and $E_{\mathrm{PHE}} = E_{\mathrm{trans}}$ is used. The effect size is given by the AMR amplitude

$$A_{\mathrm{AMR}} = \frac{\rho_{\parallel} - \rho_{\perp}}{2} \tag{2.32}$$

or the AMR ratio

$$\frac{\Delta\rho}{\rho} = \frac{2\,A_{\mathrm{AMR}}}{\rho_{\perp}} = \frac{\rho_{\parallel} - \rho_{\perp}}{\rho_{\perp}}. \tag{2.33}$$

$\Delta\rho/\rho$ is typically less than one percent but can reach a couple percent, e.g., in permalloy $\Delta\rho/\rho \approx 6\%$ [37]. The normalization done in Eq. (2.33) is reasonable for the AMR because the change in resistivity on top of the ohmic contribution $\rho \approx \rho_{\perp}$ is decisive to be detectable in a measurement. On the other hand, the PHE can be measured free from that ohmic resistivity and is, therefore, a more precise method to detect the anisotropy of the electrical resistance due to the thermal noise being proportional to temperature and resistance. A visualization of the angular dependence of AMR and PHE is shown in Fig. 2.7.

The electrical field $\boldsymbol{E}$ within a material is typically not evaluated in an experiment. Instead, the voltage $V \propto |\boldsymbol{E}|$ that arises either parallel ($\|$) or perpendicular ($\perp$) to a current I is measured with the respective resistances being defined as:

$$R_{\|} = \frac{V_{\|}}{I} \qquad\qquad R_{\perp} = \frac{V_{\perp}}{I} \tag{2.34}$$

2.1.5 Magnetization dynamics

So far, all considerations assume steady state conditions. To capture the magnetization dynamics the Landau-Lifshitz-Gilbert-Equation (LLGE)

$$\frac{\mathrm{d}\boldsymbol{M}}{\mathrm{d}t} = -\frac{\gamma}{1+\alpha^2 M_s^2}\boldsymbol{M}\times\boldsymbol{B}_{\mathrm{eff}} - \frac{\alpha\gamma}{1+\alpha^2 M_s^2}\boldsymbol{M}\times(\boldsymbol{M}\times\boldsymbol{B}_{\mathrm{eff}}) \tag{2.35}$$

is used. Here, γ is the gyromagnetic ratio, $\alpha = M_s/G$ is a parameter that respects dissipative damping with G as dimensionless Gilbert damping constant and M_s is the saturation magnetization [cf. Fig. 2.5]. Note that G and, thus, α are phenomenological quantities. The effective magnetic flux density

$$\boldsymbol{B}_{\mathrm{eff}} = \mu_0\boldsymbol{H}_{\mathrm{ext}} + \mu_0\boldsymbol{H}_{\mathrm{ani}} + \mu_0\boldsymbol{H}_{\mathrm{xc}} + \dots \tag{2.36}$$

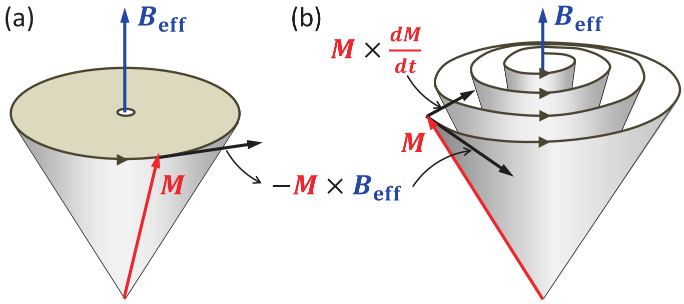

FIGURE 2.8: Magnetization dynamics following the LLGE [Eq. (2.35)]. (a) Only the precession term in considered (field-like). (b) Evolution of $\boldsymbol{M}$ respecting precession and damping. $\mathrm{d}\boldsymbol{M}/\mathrm{d}t \approx -\boldsymbol{M}\times\boldsymbol{B}_{\mathrm{eff}}$ is true for small damping α. Figure taken from Ref. [26].

consists of various contributions like the external magnetic field $\boldsymbol{H}_{\text{ext}}$ and fields that result, e.g., from the materials anisotropy (ani) or the exchange interaction (xc). Eq. (2.35) describes a superposition of two torques acting on $\boldsymbol{M}$ that point in different directions. The first one, being proportional to $\boldsymbol{M} \times \boldsymbol{B}_{\text{eff}}$, leads to a precession of the magnetization around $\boldsymbol{B}_{\text{eff}}$ as depicted in Fig. 2.8 (a). For $\boldsymbol{M}$ being in a steady state a change in $\boldsymbol{B}_{\text{eff}}$ is typically achieved by varying $\boldsymbol{H}_{\text{ext}}$. Thus, this precession is commonly considered as field driven and excitations that follow the same symmetry are therefore called field-like torques. The second term accounts for the damping of the precession and eventually enforces an alignment $\boldsymbol{M} \parallel \boldsymbol{B}_{\text{eff}}$. Contributions that follow this symmetry are called damping- or anti-damping-like torques. Damping goes with a positive sign $+\boldsymbol{M} \times (\boldsymbol{M} \times \boldsymbol{B}_{\text{eff}})$ and anti-damping refers to a negative sign $-\boldsymbol{M} \times (\boldsymbol{M} \times \boldsymbol{B}_{\text{eff}})$, respectively. The trajectory of $\boldsymbol{M}$ respecting both terms is visualized in Fig. 2.8 (b). The time necessary to orient $\boldsymbol{M}$ to a degree comparable with thermal fluctuations depends on the material and the magnitude of $\boldsymbol{B}_{\text{eff}}$ but is typically short (< 1 µs) compared to experiments that make use of external fields [40]. For electrically induced torques acting on FMs magnetization dynamics in the range of ps are achievable [41].

The formulation of the LLGE chosen in Eq. (2.35) relies on a macroscopic magnetization but it is valid for a single magnetic moments $\boldsymbol{m}$ as well. Hence, the LLGE can be used to describe the dynamics of AFMs by considering two sublattices A and B that are antiferromagnetically coupled via an exchange flux density $\boldsymbol{B}_{\text{xc}}$. This concludes into two coupled equations

$$\frac{\mathrm{d}\hat{\boldsymbol{m}}_{\text{A}}}{\mathrm{d}t} = \gamma_\alpha\, \hat{\boldsymbol{m}}_{\text{A}} \times \boldsymbol{B}_{\text{eff,A}} + \alpha\gamma_\alpha\, \hat{\boldsymbol{m}}_{\text{A}} \times \left(\hat{\boldsymbol{m}}_{\text{A}} \times \boldsymbol{B}_{\text{eff,A}}\right) \tag{2.37}$$

$$\frac{\mathrm{d}\hat{\boldsymbol{m}}_{\text{B}}}{\mathrm{d}t} = \gamma_\alpha\, \hat{\boldsymbol{m}}_{\text{B}} \times \boldsymbol{B}_{\text{eff,B}} + \alpha\gamma_\alpha\, \hat{\boldsymbol{m}}_{\text{B}} \times (\hat{\boldsymbol{m}}_{\text{B}} \times \boldsymbol{B}_{\text{eff,B}}) \tag{2.38}$$

for normalized magnetic moments $\hat{\boldsymbol{m}}_{\text{A,B}}$ with $\gamma_\alpha = -\gamma\left(1+\alpha^2\right)^{-1}$ and the effective flux densities:

$$\boldsymbol{B}_{\text{eff,A}} = \boldsymbol{B}_{\text{ext}} + \boldsymbol{B}_{\text{ani}} + B_{\text{xc}}\, \hat{\boldsymbol{m}}_{\text{B}} + \ldots \tag{2.39}$$

$$\boldsymbol{B}_{\text{eff,B}} = \boldsymbol{B}_{\text{ext}} + \boldsymbol{B}_{\text{ani}} + B_{\text{xc}}\, \hat{\boldsymbol{m}}_{\text{A}} + \ldots \tag{2.40}$$

The magnitude of the exchange flux density[2] $B_{\text{xc}} = \pm(100\ldots1000)$ T is determined by the exchange coupling strength. $B_{\text{xc}} < 0$ relates to antiferromagnetic coupling. Its direction depends on the orientation of the complementing magnetic moments.

---

[2] Estimated via Eq. (2.12) using typical values for the exchange energy E_{xc} and magnetic moment $|\boldsymbol{m}|$ [cf. Sec. 2.1.1].

One can further extend Eqs. (2.37) and (2.38) by adding terms that account for the interaction of the magnetic moments with spin(-polarized) currents, leading to spin-transfer torque (STT) and/or spin-orbit torque (SOT) [42, 43]. The relevant current-driven torque for this thesis is the Néel-order spin-orbit torque (NSOT), which will be discussed extensively in Sec. 2.2.

2.2 The Néel-order spin-orbit torque

The Néel-order spin-orbit torque (NSOT) describes a field-like torque that arises if an electrical current passes through an antiferromagnetic material that obeys certain crystallographic symmetries. More specific, the antiferromagnetically coupled atoms have to be structural inversion partners which concludes to combined $\mathcal{PT}$ symmetry. It was predicted in 2014 by Železný *et al.* as a mechanism to manipulate the Néel order, or respectively the Néel vector $\boldsymbol{L}$, in tetragonal Mn_2Au [21]. Prior to my work, the NSOT has been observed in Molecular Beam Epitaxy (MBE) grown tetragonal CuMnAs [22, 44, 45] and dc-sputtered tetragonal Mn_2Au [2, 46, 47]. The NSOT itself is a consequence of multiple more basic effects discussed in the coming sections.

2.2.1 The Rashba Effect

In systems with broken structural inversion symmetry the Rashba Effect adds a so called Rashba contribution to the SOI [26, 48]. The foundation of this effect lies in relativistic transport theory which will not be examined further in this work. The consequence of the Rashba Effect, however, is a spin-dependent $\boldsymbol{k}$-band splitting while complying with $\boldsymbol{s} \perp \boldsymbol{k}$. $\boldsymbol{s}$ is further limited by the remaining symmetry. In a thin film for example the inversion asymmetry is given by the confinement of the electrons to a two-dimensional plane, e.g. the xy-plane. Here, $\boldsymbol{s} \perp \boldsymbol{k}$ is accompanied by $\boldsymbol{s} \perp \boldsymbol{z}$. A dispersion with finite Rashba coupling and, thus, spin-momentum locking is illustrated in Fig. 2.9. For Mn_2Au and CuMnAs the tetragonal axis is analog to the surface normal of this thin film example.

2.2.2 The inverse Spin Galvanic Effect

In a system with Rashba coupling and, thus, $\boldsymbol{k}$-band splitting one can observe the inverse Spin Galvanic effect (iSGE) [50, 51]. A simple picture to get the idea of the iSGE is drawn by the help of Fig. 2.10. Note that Fig. 2.10 (b) is essentially the cross-section of Fig. 2.9 (a) for $k_y = 0$. Here,

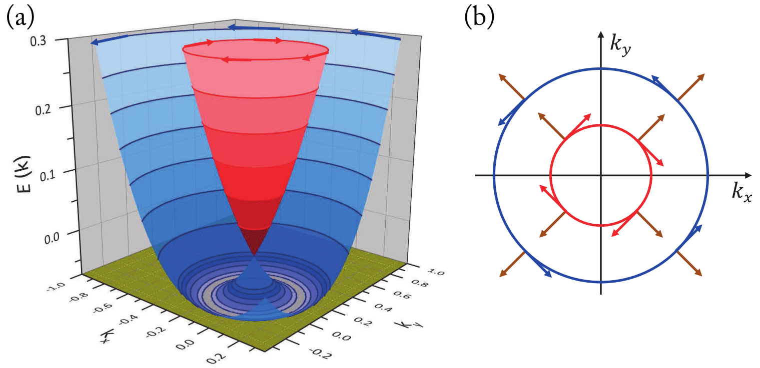

FIGURE 2.9: (a) Disperion relation of a 2D-electron gas with finite Rashba coupling. The $\boldsymbol{k}$-bands are split for antiparallel orientations of $\boldsymbol{s} \perp \boldsymbol{k}$. (b) Cross-section of (a) for a constant energy $E(\boldsymbol{k}) = constant$. $\boldsymbol{s}$ is indicated by the red and blue arrows while the brown arrows mark the direction of $\boldsymbol{k}$. Figure taken from Ref. [26].

the electron's dispersion relation follows

$$\varepsilon = \frac{\hbar^2 \boldsymbol{k}^2}{2m^*} \pm \beta \, |\boldsymbol{k}| \tag{2.41}$$

with $\hbar$ as the reduced Planck constant, m^* as the effective mass and β as the spin-orbit coupling strength. If an electric field $\boldsymbol{E}$ is applied to the material, the Fermi surface will move until an equilibrium between acceleration by the electric field and deceleration by scattering events is obtained. This results in a stationary current density $\boldsymbol{j} \parallel \boldsymbol{E}$. A projection of the Fermi surface for $\boldsymbol{E}$ pointing in x direction is shown in Fig. 2.10 (a) for spin-degenerated systems, i.e. $\beta = 0$. For $\beta \neq 0$ the parabolic energy band splits into two subbands with opposite spin polarization [cf. Fig. 2.10 (b)]. A scattering event can always include a spin-flip since the spin orientation is not a conserved quantity. For the given system, however, the spin-flips $|\uparrow\rangle \rightarrow |\downarrow\rangle$ and $|\downarrow\rangle \rightarrow |\uparrow\rangle$ involve different quasi-momentim transfers Δk. Hence, one process becomes more likely and the electrical current gets spin polarized. The direction of this local spin polarization $\boldsymbol{\sigma}$ depends on the symmetry of the Rashba coupling which itself depends on the local magnetic moment, i.e. $+\boldsymbol{\sigma} \rightarrow -\boldsymbol{\sigma}$ if $+\boldsymbol{m} \rightarrow -\boldsymbol{m}$. In AFMs with combined $\mathcal{PT}$ symmetry this local spin polarization creates a macroscopic spin polarization of the current due to the alternation of $\boldsymbol{\sigma}$ on each magnetic lattice site. Here, the term macroscopic deserves special attention since a material that exhibits

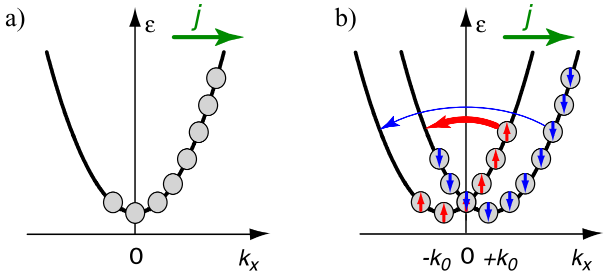

Figure 2.10: Plots of the dispersion relation of electrons according to Eq. (2.41). The occupation of states under the influence of an electric field is illustrated by circles located on the parabolic dispersion. (a) Without SOI and, thus, spin-degeneracy. (b) For $\beta \neq 0$ the dispersion relation splits in two subbands that are shifted in $\boldsymbol{k}$-space dependent on their spin orientation. Consequently, one type of spin-flip scattering becomes more likely. Figure adapted from Ref. [49].

inversion symmetry still can develop spin polarizations locally that cancel out in macroscopic systems.

2.2.3 Torques acting on the Néel order

In a two-dimensional AFM, where the antiparallel coupled magnetic sublattices form structural inversion partners, the iSGE can drive antiferromagnetic magnetization dynamics. Prominent examples for materials that comply with this prerequisites are, as statet before, tetragonal Mn_2Au and tetragonal CuMnAs thin films. The unit cell of CuMnAs is shown in Fig. 2.11 (a). Its magnetic structure can be abstracted with two normalized magnetic moments $\hat{\boldsymbol{m}}_\mathrm{A}$ and $\hat{\boldsymbol{m}}_\mathrm{B}$ representing each magnetic sublattice, respectively [cf. Fig. 2.11 (b)]. In such a system, the iSGE generates local spin polarizations that are different at each lattice site if a current density $\boldsymbol{j}$ is pushed through the materials plane. This local spin polarizations, characterized by the local spin polarization vector $\boldsymbol{\sigma}$, interact with the local magnetic moments $\boldsymbol{m}$ by exerting a field-like torque of the form

$$\boldsymbol{\Gamma} = \frac{\mathrm{d}\boldsymbol{m}}{\mathrm{d}t} \propto \boldsymbol{m} \times \boldsymbol{\sigma} \tag{2.42}$$

with $\boldsymbol{\sigma} \propto \boldsymbol{j} \times \boldsymbol{z}$ where $\boldsymbol{z}$ points out of plane (oop), i.e. parallel to the c axis of the CuMnAs unit cell [cf. Fig. 2.12 (a)]. The sign of $\boldsymbol{\sigma}$ depends on the direction of the local magnetic moment and, therefore, has an oppo-

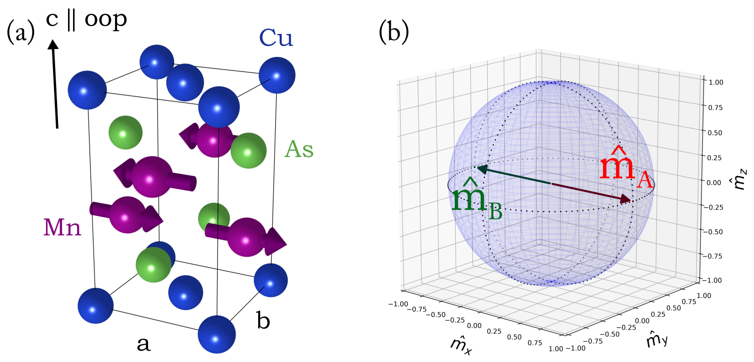

Figure 2.11: (a) The unit cell of tetragonal CuMnAs. The c axis points oop. The Mn atoms are structural inversion partners but with antiparallel orientation of their magnetic moments. (b) Simplified representation of the magnetic structure in CuMnAs. Here, the normalized magnetic moments $\hat{\boldsymbol{m}}_{\mathrm{A,B}}$ represent each sublattice, respectively. x, y and z correspond to a, b and z in (a), respectively. Subfigure (a) was created in VESTA [52] and subfigure (b) was made with a Python script.

site sign on lattice sites that are structural inversion partners. The antiferromagnetic sublattices A and B are characterized by the magnetic moments $\boldsymbol{m}_{\mathrm{A}} = -\boldsymbol{m}_{\mathrm{B}}$. If these magnetic moments are exposed to the local spin polarizations $\boldsymbol{\sigma}_{\mathrm{A}} = -\boldsymbol{\sigma}_{\mathrm{B}}$ they will experience a parallel torque

$$\boldsymbol{\Gamma}_{\mathrm{A}} \parallel \boldsymbol{m}_{\mathrm{A}} \times \boldsymbol{\sigma}_{\mathrm{A}} \parallel (-\boldsymbol{m}_{\mathrm{A}}) \times (-\boldsymbol{\sigma}_{\mathrm{A}}) \parallel \boldsymbol{m}_{\mathrm{B}} \times \boldsymbol{\sigma}_{\mathrm{B}} \parallel \boldsymbol{\Gamma}_{\mathrm{B}} \tag{2.43}$$

on each sublattices magnetic moments [cf. Fig. 2.12 (a)]. This torque induces a small ferromagnetic moment $\delta\boldsymbol{m}_z \parallel \boldsymbol{\Gamma}_{\mathrm{A,B}}$ in oop direction which is countered by the exchange interaction. Eventually, this results in an exchange torque

$$\boldsymbol{\Gamma}^{\mathrm{xc}}_{\mathrm{A,B}} = \boldsymbol{m}_{\mathrm{A,B}} \times \delta\boldsymbol{m}_z \propto \boldsymbol{m}_{\mathrm{A,B}} \times \left(\boldsymbol{m}_{\mathrm{A,B}} \times \boldsymbol{\sigma}_{\mathrm{A,B}}\right). \tag{2.44}$$

$\boldsymbol{\Gamma}^{\mathrm{xc}}_{\mathrm{A,B}}$ has the form of a damping-like torque acting on the Néel vector $\boldsymbol{L}$ that drives a rotation [cf. Fig. 2.12 (b)]. The magnetic damping slows down the rotation and results in an equilibrium state in which the torque $\boldsymbol{\Gamma}_{\mathrm{A,B}}$ and, thus, $\boldsymbol{\Gamma}^{\mathrm{xc}}_{\mathrm{A,B}}$ becomes zero. This is true for $\boldsymbol{m}_{\mathrm{A,B}} \parallel \boldsymbol{\sigma}_{\mathrm{A,B}}$ which is equivalent to $\boldsymbol{L} \perp \boldsymbol{j}$. Hence, the current *switches* $\boldsymbol{L}$ from parallel to perpendicular with respect to the current density $\boldsymbol{j}$.

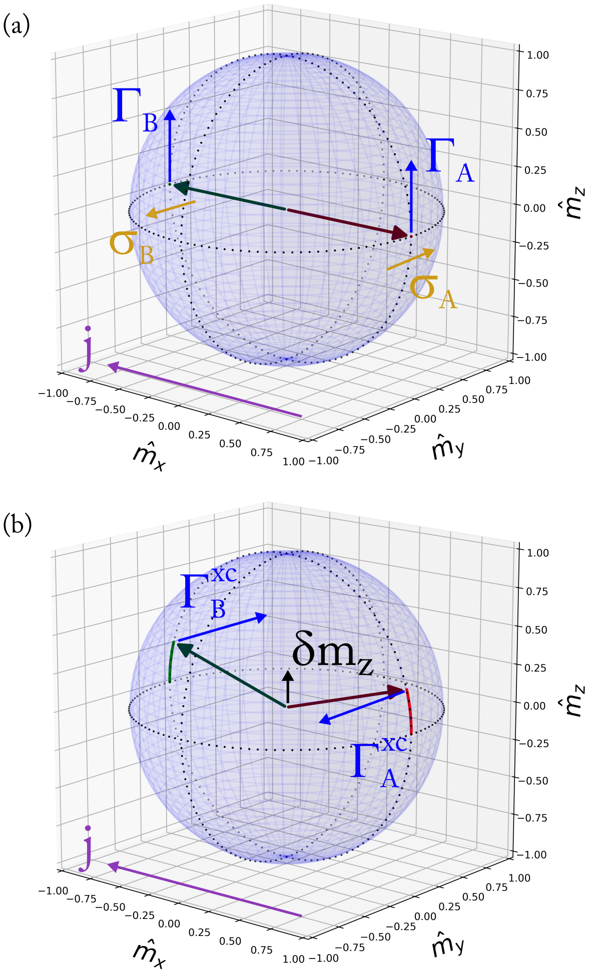

FIGURE 2.12: (a) Initial state with the Néel vector $\boldsymbol{L}$ being parallel to the x axis. The current density $\boldsymbol{j}$ points in $-x$ direction, i.e. $\boldsymbol{j} \parallel \boldsymbol{L}$. The spin polarization $\boldsymbol{\sigma}_{\mathrm{A,B}}$ is opposite for each sublattice, resulting in the parallel torques $\boldsymbol{\Gamma}_{\mathrm{A,B}}$ that disturb the antiparallel alignment. (b) The canting of the moments induces a small ferromagnetic component $\delta \boldsymbol{m}_z$. Disrupting the antiparallel order is costly in terms of energy for antiferromagnetically coupled moments. Hence, the exchange interaction gives rise to the exchange torque $\boldsymbol{\Gamma}^{\mathrm{xc}}_{\mathrm{A,B}}$ which leads to a rotation of the moments. The plots were created with a Python script.

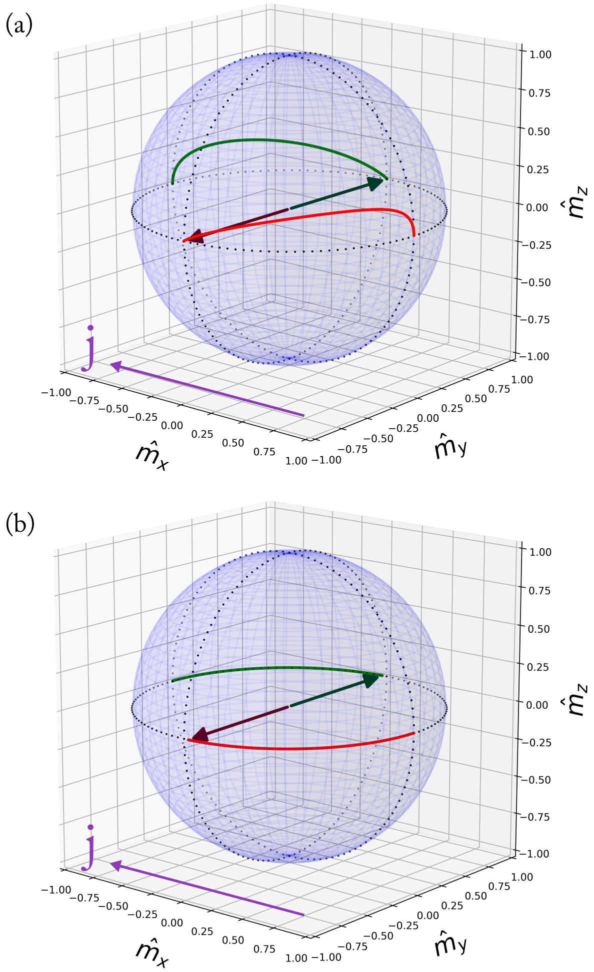

FIGURE 2.13: Trajectory of $\hat{\boldsymbol{m}}_{\mathrm{A,B}}$ with $\boldsymbol{\sigma} \propto \boldsymbol{j} \times \boldsymbol{z}$ and $\boldsymbol{j} \parallel -\boldsymbol{x}$ as exclusive driving force that is constant in time. (a) For $B_{\mathrm{xc}} = 1\,\mathrm{T}$ to overemphasize the canting of the moments as intermediate step for the rotation. (b) With a more realistic exchange field of $B_{\mathrm{xc}} = 100\,\mathrm{T}$. The canting remains but becomes too small to visualize. The graphs were generated with a Python script. The used parameters beside B_{xc} are $\alpha = 1$, $\left|\boldsymbol{m}_{\mathrm{A,B}}\right| = 500\,\mathrm{kA/m}$, and $\boldsymbol{\Gamma}_{\mathrm{A,B}} = 0.5\,\mathrm{J}$. Magnetic anistropy is neglected, i.e. $K_{\mathrm{ani}} = 0$. Introducing a magnetically hard z axis has no qualitative effect on the dynamics. For this parameter set the switching takes 80 ps.

The switching is a dynamic process in which the torques continuously change due to the canting and rotation of the moments. The time evolution is given by coupled LLGEs similar to Eqs. (2.37) and (2.38) extended by a field-like torque resulting from the NSOT and a normalization factor due to $|\boldsymbol{m}| \neq 1$. A visualization of the switching is shown in Fig. 2.13. The simulation is done with a Python script that solves the LLGE numerically using the Euler method in time steps of $\delta t = 5 \times 10^{-18}$ s. The solver has been programmed by Prof. Dr. Markus Meinert and was adapted for the given problem by the author of this thesis.

2.2.4 The effective Néel-order spin-orbit torque field

The drawn picture sketches the mechanism how the iSGE leads to a rotation of $\boldsymbol{L}$ that eventually reaches an equilibrium configuration in which $\boldsymbol{L} \perp \boldsymbol{j}$. For the transport experiments conducted in the course of this thesis, however, the dynamics of the current induced reorientation of $\boldsymbol{L}$ has no relevance since it is not resolvable anyway. Hence, the torques that eventually reorient, or switch, the Néel order are condensed into a staggered effective field

$$\boldsymbol{B}_{\text{eff}} = (\boldsymbol{j} \times \boldsymbol{z})\,\chi \tag{2.45}$$

with the spin-orbit-torque efficiency χ. $\boldsymbol{B}_{\text{eff}}$ gives rise to the Zeeman energy density

$$\varepsilon_{\text{Zeeman}} = -\frac{\boldsymbol{L} \cdot \boldsymbol{B}_{\text{eff}}}{V_{\text{cell}}} \tag{2.46}$$

per unit cell volume V_{cell} which is minimized for $\boldsymbol{L} \perp \boldsymbol{j}$.

To apply this effective field approach to an actual sample on has to consider additional sample specific properties. First, the film is not single crystalline but consists of many grains of grain volume V_{g}. Second, CuMnAs is assumed to have a strain induced biaxial anisotropy which is characterized by the anisotropy constant $K_{4\|}$ [53]. The easy axes correspond to the a and b axes, i.e. (100) and (010) directions, of the tetragonal CuMnAs [54] [cf. Fig. 2.11 (a)]. Furthermore, the Néel vector of a single grain is regarded as collinear. The magnetic energy of a CuMnAs grain under the influence of an electrical current density $\boldsymbol{j}$ can be written as

$$E(\varphi) = \left[K_{4\|} \sin^2 2\varphi - \frac{\boldsymbol{L} \cdot \boldsymbol{B}_{\text{eff}}}{V_{\text{cell}}}\right] V_{\text{g}} \tag{2.47}$$

with φ being the angle between $\boldsymbol{L}$ and the a axis of the film [cf. Sec. 2.1.2.2]. Following this description, $\boldsymbol{L}$ can be switched between different states that coincide with magnetic easy axes if the NSOT, given by Eq. (2.46) multiplied by V_g, overcomes the anisotropy energy barrier

$$E_\text{ani} = K_{4\|} V_\text{g} \tag{2.48}$$

and the pulse lines coincide with the magnetic easy axes a and b. Note that the lithography is done to ensure that a and b are parallel to x and y, respectively [cf. Fig. 2.11 (a) and Fig. 3.4]. Up to now, this process is regarded as deterministic and the set state is stable in time. Hence, a current burst of sufficient magnitude would switch $\boldsymbol{L}$ and the resulting orientation could be evaluated by a PHE measurement using the 45° rotated probe lines [for more details regarding the pulse-probe setup cf. Sec. 3.4]. The expected result is a switching between two discrete $R_\perp$ values that are related to the AMR amplitude. Furthermore, the switching should be temperature independent as the NSOT mechanism is predicted to be independent of the electron-scattering time [21].

However, the preliminary experiments on Mn_2Au [2] suggest that the switching is probabilistic, e.g. a thermally activated or at least assisted process. This hypothesis is consistent with the results of this dissertation.

2.3 Relevance of thermal activation

The potential-energy surface (PES), often simply called energy landscape, described by Eq. (2.47) is plotted in Fig. 2.14 (a) using parameters that have been found to be reasonable in the course of this work [cf. Sec. 4.2]. The local minima given by the biaxial anisotropy of the CuMnAs are shifted slightly due to the NSOT energy, but the energy barrier separating neighboring minima remains $E_\text{B} > 0$. Thus, no deterministic switching can be observed in this system using moderate current densities. The current density at which deterministic switching occurs, i.e. $E_\text{B} < 0$ due to the NSOT energy, is [2]

$$j_\text{det} = \frac{8\sqrt{6}}{9} \frac{K_{4\|} V_\text{cell}}{L\chi}. \tag{2.49}$$

For the CuMnAs system this calculates to $j_\text{det} \approx 22 \times 10^{10}\,\text{A/m}^2$.

The system, however, is at a finite temperature T with the thermal energy $k_B T|_{T=300\,\text{K}} \approx 26\,\text{meV}$. $k_B = 1.380649 \times 10^{-23}\,\text{J/K}$ is the Boltzmann constant. $k_B T$ is comparable to E_B and, therefore, the system can change its state by a thermally activated hopping process. This infers that a system of multiple grains, which have $\boldsymbol{L}$ aligned in a certain direction, will randomize over time since it is thermally unstable. The hopping becomes preferential

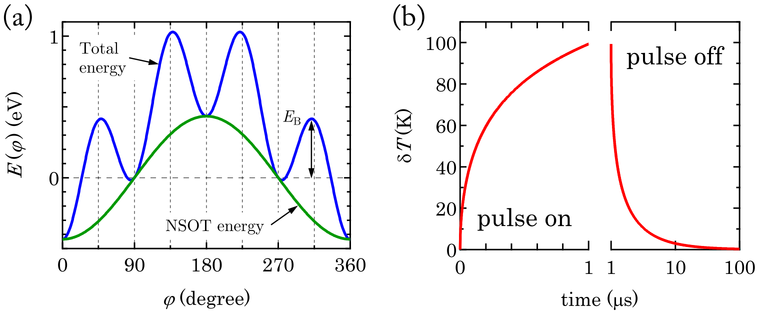

FIGURE 2.14: (a) Calculated PES using Eq. (2.47) with the parameters $|\boldsymbol{j}| = 6.0 \times 10^{10}\,\mathrm{A/m^2}$, $\chi = 3\,\mathrm{mT}/(10^{11}\,\mathrm{A/m^2})$ [22], $|\boldsymbol{L}| = 7\mu_\mathrm{B}$ [54], $K_{4\|} = 1.2\,\mu\mathrm{eV/(unitcell)} \approx 2.1\,\mathrm{kJ/m^3}$, $V_\mathrm{cell} = 6.318\,\text{Å} \cdot \left(3.820\,\text{Å}\right)^2$, and $V_\mathrm{g} = (38\,\mathrm{nm})^3$, obtained from literature or experimental results presented in Sec. 4.2. Here, $E_\mathrm{B} \approx 0.4\,\mathrm{eV}$ is the energy barrier for a switching from $\varphi = 270°$ to $\varphi = 360°$. (b) Time dependent temperature rise δT for a current pulse with $|\boldsymbol{j}| = 6.0 \times 10^{10}\,\mathrm{A/m^2}$ and $\Delta t = 1\,\mu\mathrm{s}$ calculated using Eq. (2.50). The x-axis is split into a linear and a logarithmic segment.

due to the NSOT which allows for a thermally assisted switching that occurs at $j < j_\mathrm{det}$. Furthermore, the current generating the NSOT also heats up the device due to the Joule heating power $\mathrm{d}P = \rho j^2\,\mathrm{d}V$. The experiment therefore facilitates the switching by multiple means, i.e., reducing the energy barrier with the NSOT and enhancing hopping processes by increasing the temperature. A model derived by You *et al.* can be used to estimate the temperature rise [55]

$$\delta T(t) = \frac{whj^2}{\pi \kappa_\mathrm{s} \sigma} \left[\operatorname{arcsinh}\left(\frac{2\sqrt{\mu_\mathrm{s} t}}{\alpha w}\right) - \theta\left(t - \Delta t\right) \operatorname{arcsinh}\left(\frac{2\sqrt{\mu_\mathrm{s}\left(t - \Delta t\right)}}{\alpha w}\right) \right] \tag{2.50}$$

of a thin film device during a current pulse. The model considers a two-dimensional heat dissipation into the substrate with parameters κ_S and μ_S, namely the heat conductivity and the thermal diffusivity. h is the film thickness, w is the pulse line width and σ is the electrical conductivity of the film. α is an adjustable parameter which is set to $\alpha = 0.5$ as suggested by You *et al.*. The evaluation of Eq. (2.50) using the substrate parameters $\kappa_\mathrm{GaAs} = 55\,\mathrm{W/(m\,K)}$ and $\mu_\mathrm{GaAs} = 31\,\mathrm{mm^2/s}$ of GaAs and device parameters $h = 68\,\mathrm{nm}$, $w = 8\,\mu\mathrm{m}$, and $\sigma = (430\,\mu\Omega\,\mathrm{cm})^{-1}$ is shown in Fig. 2.14 (b). The temperature rise of the device will reduce σ and, thus, j will fall during the pulse since a constant voltage source is used to generate the current bursts. Therefore, the calculation yields an upper estimate for δT.

The energetic conditions, at least in this particular experiment with sputter-deposited films of high granularity, demand to regard the switching as a thermally activated mechanism that promotes a preferential orientation of $\boldsymbol{L}$ due to a weak contribution that originates from the NSOT. An independently acting grain in such a film with thermally driven dynamics will attempt to change its state at a rate ν that is given by the Néel-Arrhenius equation

$$\nu = \frac{1}{\tau} = f_0 \exp\left(-\frac{E_\mathrm{B}}{k_B T}\right). \tag{2.51}$$

The attempt rate $f_0 = 10^{12}\,\mathrm{Hz}$ accounts for the THz dynamics in antiferromagnets, i.e., the ultrafast precession of the sublattice magnetic moments about the exchange field [56].

2.3.1 Thermal relaxation

After each attempt, $\boldsymbol{L}$ can end in one of p different states where p denotes the number of minima in the PES [cf. Fig. 2.14 (a)] which is equivalent to a p-fold rotational symmetry. Such a system can be described as

$$\boldsymbol{N} = \begin{pmatrix} N_1 \\ N_2 \\ \vdots \\ N_p \end{pmatrix} \tag{2.52}$$

with N_i being the relative occupation number of each state and $\sum_i N_i = 1$. Without electrical current, all states are energetically degenerate and, thus, the change of N_i depends on its occupation only. Therefore, one can write

$$\frac{\mathrm{d}N_i}{\mathrm{d}t} = \sum_{j=1}^{p} \left[\left(\frac{1}{p} - \delta_{ij}\right) \nu N_j\right] \tag{2.53}$$

as the time derivative of N_i. δ_{ij} is the Kronecker delta and ν is given by Eq. (2.51). For the CuMnAs films a biaxial anisotropy ($p = 4$) is assumed and, hence, Eq. (2.53) can be written in matrix form as

$$\frac{\mathrm{d}\boldsymbol{N}}{\mathrm{d}t} = \frac{\nu}{4} \begin{pmatrix} -3 & 1 & 1 & 1 \\ 1 & -3 & 1 & 1 \\ 1 & 1 & -3 & 1 \\ 1 & 1 & 1 & -3 \end{pmatrix} \begin{pmatrix} N_1 \\ N_2 \\ N_3 \\ N_4 \end{pmatrix} \tag{2.54}$$

which has the general solution

$$\begin{aligned} \boldsymbol{N}(t) = \exp(-\nu t) &\left[C_1 \begin{pmatrix} -1 \\ 0 \\ 0 \\ 1 \end{pmatrix} + C_2 \begin{pmatrix} -1 \\ 0 \\ 1 \\ 0 \end{pmatrix} + C_3 \begin{pmatrix} -1 \\ 1 \\ 0 \\ 0 \end{pmatrix} \right] \\ &+ \frac{1}{4} \begin{pmatrix} 1 \\ 1 \\ 1 \\ 1 \end{pmatrix} . \end{aligned} \tag{2.55}$$

$N_{1,3}$ and $N_{2,4}$ account for $\boldsymbol{L}$ being (anti)parallel to the x- or y-axes of the experiment, respectively. For all grains being oriented, e.g. $N_1 = 1$, one obtains the coefficients $C_1 = C_2 = C_3 = -1/4$. In a PHE measurement this results in the time dependent transverse resistance

$$R_\perp(t) = A_{\mathrm{AMR}} \left[N_1(t) + N_3(t) - N_2(t) - N_4(t) \right] \tag{2.56}$$

$$= A_{\mathrm{AMR}} \exp(-\nu t) , \tag{2.57}$$

where A_{AMR} is the AMR amplitude [cf. Sec. 2.1.4]. If not all grains are collinear at $t = 0$ the amplitude is reduced, i.e. $R_\perp(t = 0) < A_{\mathrm{AMR}}$. $R_\perp$ decays with the Néel-Arrhenius rate ν. Using the more common decay constant $\tau = 1/\nu$ this concludes to

$$R_\perp = R_\perp(t = 0) \exp\left(-\frac{t}{\tau} \right) . \tag{2.58}$$

2.3.2 Derivation of an analytic expression for the switching

For $j \neq 0$ a grain will preferably switch into a low energy state, but the mechanism remains probabilistic with small switching probability and high attempt rate. Such a system is described by a Poisson distribution and the probability that an electrical pulse of length Δt switches the grain therefore reads [2]

$$P_{\mathrm{sw}}(\Delta t) = 1 - \exp\left(-\frac{\Delta t}{\tau} \right) \tag{2.59}$$

with τ being given by Eq. (2.51). This is a purely kinetic description and only valid for pulses $\Delta t \gg 1/f_0$, which is satisfied for $\Delta t \geq 1$ µs. For small switching probability $P_{\text{sw}} \approx 0$ one can apply a linear response approximation by expanding the exponential in Eq. (2.59) to

$$P_{\text{sw}}(\Delta t) \approx \Delta t f_0 \exp\left(-\frac{E_\text{B}}{k_B T}\right) \tag{2.60}$$

with τ being inserted accordingly. For an initially uniform occupation of all states and identical grains the transverse resistance, generated by the PHE, becomes $R_\perp \propto P_{\text{sw}}$. Hence, the $R_\perp$ change per current pulse in linear response regime is given by

$$\left|\Delta R_\perp^{\text{lin}}\right| \approx A \Delta t f_0 \, \exp\left(\frac{x L \chi V_\text{g} j}{k_B T V_\text{c}} - \frac{E_\text{B}}{k_B T}\right) \tag{2.61}$$

with A being the effect amplitude which equals the AMR amplitude in the case of coherent switching of all grains.

$$x = \left\{\pm\frac{1}{\sqrt{2}}, \pm\left(1 - \frac{1}{\sqrt{2}}\right), -\left(1 + \frac{1}{\sqrt{2}}\right)\right\} \tag{2.62}$$

reflects that the energy barrier E_B entering Eq. (2.51) depends on the combination of initial and final state [cf. Fig. 2.14 (a)]. Further considering the experimental condition of a constant charge per burst Q, a detail that will be discussed in Sec. 3.4, one obtains a linear response approximation per burst of

$$\left|\Delta R_\perp^{\text{burst}}\right| \approx \frac{Q A f_0}{j w h} \exp\left(\frac{x L \chi V_\text{g} j}{k_B T V_\text{c}} - \frac{E_\text{B}}{k_B T}\right) \tag{2.63}$$

by multiplying Eq. (2.61) with Eq. (3.18). This equation yields multiple predictions regarding the dependence of the switching characteristics on various experimental parameters. The switching amplitude is found to depend exponentially on the current density j and also exponentially on the measurement temperature T. Here, the switching amplitude is independent of the pulse width Δt. However, the temperature rise δT during the pulse is not captured by this description [cf. Eq. (2.50)]. Thus, longer Δt are expected to increase the switching amplitude as well since they facilitate higher sample temperatures.

Experimental techniques 3

The scope of this thesis is an experimental investigation of the NSOT introduced theoretically in Sec. 2.2. The process steps to fabricate a suitable device for transport measurements are illustrated in Sec. 3.1. In this work, the transport experiment profoundly relies on the Lock-In technique which is outlined in Sec. 3.2. Sec. 3.3 gives an introduction to simulation routines that are used to corroborate the interpretation of the results.

This chapter will be concluded by Sec. 3.4 where the experimental sequence of the transport experiment is presented. Although the applied methods are allover common, the exact progression of current flows is new and was designed in the course of this work to rule out artifacts, e.g. by measuring a polarity dependence.

3.1 Sample preparation

In this section the sample preparation procedure will be outlined with the assumption, that the fundamentals about standard techniques as sputter deposition [57, 58], lithography [59, 60] and basic thin film characterization methods [61–64] are already known.

3.1.1 Thin film growth

All samples that are discussed in this thesis were grown by magnetron sputtering in machines that allow to vary the substrate temperature during deposition. If not specified otherwise, the plasma was sustained with a dc power supply. For epitaxial samples, (1×1) cm^2 large pieces of single-crystalline GaAs (001) or MgO (001) were used as substrates. MgO is electrically insulating while GaAs is a semiconductor. However, the used GaAs was undoped with a resistivity $\rho_{\mathrm{GaAs}} > 10^8$ Ωcm at room temperature and, thus, acts like an insulator in regard of transport experiments. To evaluate the stoichiometry of a deposited alloy via x-ray fluorescence (XRF), completely amorphous SiO$_2$, also called fused silica (FS), substrates were used. Growth rates were determined by measuring x-ray reflectivity (XRR) at films grown on either FS or fragments of Si-wafers with 50 nm thermally oxidized surface. All samples were capped with materials, i.e. Ti or Si, that passivate under ambient conditions to prevent a degradation of the film. Materials that are stable in air were capped as well to keep the sample stacks as similar as possible. Si was always sputtered using an rf generator.

Usually, MgO substrates are suitable to grow epitaxial samples without any preparation steps. A GaAs substrate, however, must undergo a cleaning procedure before executing the deposition since its surface oxidizes under ambient conditions and the oxide has not the crystallographic properties for which GaAs was chosen in the first place. Hence, the oxide layer has to be removed, e.g. by a chemical treatment with technical hydrochloric acid 37% (HCl). HCl dissolves the oxide layer and does not damage the GaAs itself. In addition, the substrates surface becomes protonated by the acid which acts as a short-time protection from further oxidization. The GaAs preparation procedure follows:

1. HCl etching for 2 minutes
2. flushing with purified water
3. drying with pressurized N_2 gas
4. insertion into the sputtering chamber

Once the substrate is placed into the sputtering chamber and, thus, in a vacuum with base pressure $p_0 < 1 \times 10^{-7}$ mbar, the surface does not need protection from oxidization anymore. However, the surface is still protonated and has to be cleared, e.g. by increasing the substrates temperature above the desorption temperature T_D of the protective layer. This work asserts that $T_\mathrm{D} \approx 400°\mathrm{C}$ [cf. Sec. 4.1].

3.1.2 Structural characterization

XRR and x-ray diffraction (XRD) experiments are performed to investigate the structural properties of the deposited films. XRR curves can be fitted using the GenX reflectivity-fitting package to obtain parameters as thickness, mass density and interface/surface roughnesses [65]. For the fit to succeed it is necessary that the root-mean-square roughness R_RMS of the films surface and interfaces are sufficiently small. The threshold up to which R_RMS the evaluation is possible differs quite a bit and depends on the optical properties of the material and the machinery, e.g., which wavelength and optics are used. For CuMnAs measured with the locally available diffractometer this threshold is around $R_\mathrm{RMS} \approx 5\,\mathrm{nm}$. XRD is used to investigate the crystallography of the grown film, i.e., the crystal structure, the oop lattice constant

c and the oop crystallite size L_c. The ip lattice constants are referred to as a and b. The crystal structure determines which diffraction peaks, characterized by the Miller indices $(\,h\,k\,l\,)$, exist. From peaks with indexing $(\,0\,0\,l\,)$ one can calculate

$$c = \frac{\lambda l}{2\sin\theta}. \tag{3.1}$$

$\lambda = 1.540598\,\text{Å}$ is the used x-ray wavelength. θ describes the angle between the x-ray beam and the samples surface with $\theta = 90°$ representing a perpendicular incidence. Scherrer's formula allows to estimate

$$L_c \approx \frac{\lambda}{\beta_\mathrm{w}\cos\theta} \tag{3.2}$$

from the integral width β_w of a diffraction peak in radians.

The surface roughness obtained by XRR represents the samples topography with a single number σ_s, which is only equal to R_RMS if the height profile follows a Gaussian distribution. The real value of R_RMS for any height profile, and many other topographic features, can be examined by scanning force microscopy (SFM) (also known as atomic force microscopy). In principle, SFM can be used to evaluate the lateral-grain-size distribution or the lateral-coherence length. However, in this thesis, the purpose of SFM was solely to obtain reliable values for R_RMS.

Another method to investigate the samples surface is scanning electron microscopy (SEM). This technique creates images with morphologic and material dependent contrast. SEM lacks the possibility to quantify the height of details in the image and the lateral resolution is inferior to SFM. However, taking a SEM image takes seconds while the recording of a SFM measurement takes tens of minutes. Additionally, SFM is more limited than SEM regarding the design of the sample. In particular, only small planar thin film samples can be investigated by SFM due to the mechanical components that are necessary to handle the cantilever. SEM was not used as regular characterization method but becomes important in Chap. 5, especially due to its utility regarding the morphological investigation of bonded samples.

The inner structure of a thin film can be imaged by transmission electron microscopy (TEM). This technique has a great spatial resolution and allows to visualize the ordering of atoms in the film as a real-space picture. Thus, one can evaluate grain sizes in those pictures as well. It is also possible to create element-specific images to track diffusive processes or to identify oxidized layers. Unfortunately, to create a TEM image a thin lamella has to be cut out of the thin film sample which destroys the sample partially and poses considerable effort. Thus, only one TEM image, recorded by Daniela Ramermann, was made to complement the findings of this thesis.

3.1.3 Electrical characterization

A fast but yet powerful electrical characterization can be made via the four-point method. Here, four equidistant tips are placed on the sample in a line. The voltage drop $V_{4\mathrm{p}}$ between the inner tips can be used to calculate the resistance $R_{4\mathrm{p}} = V_{4\mathrm{p}}/I_{4\mathrm{p}}$ with the current $I_{4\mathrm{p}}$ flowing in the film, injected through the outer tips. The resistivity of a thin film sample then computes to

$$\rho = h \frac{\pi}{\ln 2} R_{4\mathrm{p}} \tag{3.3}$$

with the film thickness h.

3.1.4 Lithography and electrical contacting

The samples are grown as planar films and the standard characterization methods, specifically XRR, XRD, SFM and four-point resistivity measurement, can be done noninvasive without further preparation. On the other hand, plenty experiments require to pattern the film into a distinct structure. A structured film that serves a certain purpose is generally called device. For this thesis, the patterning was done with ultra-violet lithography (UVL) and electron-beam lithography (EBL) to define devices with dimensions in the micrometer scale. The etching was done with Ar-ion milling. Initial experiments were carried out with devices structured by EBL, which is a time consuming but very accurate way to do the patterning. Later it became evident that this high precision is not necessary for the experiment and, therefore, UVL was used as fast alternative. For transport experiments, it is necessary to reliably contact the devices electrically. Thus, a device is typically connected to contact pads with dimensions of $(100 \times 100)\ \mu\mathrm{m}^2$. The pads are either part of the initial lithography step and, thus, consist of the sample's material, or they are added in a second lithography step and are made of, e.g., a Ta/Au double layer with low resistance. In this thesis no Au contact pads were used, primarily because the films investigated in Chap. 4 repeatably became damaged during the second lithography step. Anyhow, it was tested several times to perform two-step lithography since a low resistance of the whole device is usually desirable.

If only a small number of contacts, e.g. two, have to be connected to the electrical equipment to do an experiment, the contacting is often realized via gold needles. This method is handy because there is no need for further sample preparation following the lithography. The experiments done in this work, however, need eight connections. Thus, the samples were placed into ceramic dual inline packages (C-DIPs) with a lead count of 24. The cavity, in which the sample was glued with silver paint, had dimensions of (9.65×9.65) mm^2. Hence, after performing the lithography, the sample had to be cleaved to fit in the cavity. The sample was coated with uv-resist during the breaking process to keep the surface dust free. The connections between contact pads and C-DIP leads were established by Al-wedge bonding.

3.2 The Lock-In technique

The class of experiment that is fundamental to this thesis is the electrical transport experiment, i.e., measuring a voltage V that arises as consequence to a charge current I. This voltage measurement is often considered simple since high quality dc and ac voltage measurement equipment is commercially available. However, resolving small voltage changes on top of a base voltage or measuring small voltages with magnitudes comparable to, e.g., thermal noise or crosstalk from other electromagnetic emitters, is a nontrivial task. The conventional approach to increase the sensitivity of a voltmeter is to apply a moving-average filter which is not very efficient especially if the perturbations originate from crosstalk. A more advanced method is the so-called Lock-In technique which is the subject of this section. It is applicable in a great variety of experiments as long as an ac driving force is related to an ac response. Here the focus lies on its implementation regarding ac transport experiments and, hence, this passage conditions that a Lock-In amplifier is used. The presented information is extracted from a Stanford Research Systems Lock-In amplifier manual [66].

A Lock-In measurement requires a reference frequency ω_r at which the Lock-In amplifier generates a time dependent output voltage

$$V_\mathrm{ref}(t) = V_0^\mathrm{ref} \sin\left(\omega_\mathrm{r} t + \theta_\mathrm{r}\right) \tag{3.4}$$

with amplitude V_0^ref and phase θ_r. If the output of the Lock-In amplifier is connected to a perfect ohmic resistor with resistance R an in-phase current

$$I_\mathrm{out}(t) = \frac{V_0^\mathrm{ref}}{R} \sin\left(\omega_\mathrm{r} t + \theta_\mathrm{r}\right) \tag{3.5}$$

is driven through this resistor. The voltage drop over that resistor, which is the measurement signal of interest in this example, is $V_\mathrm{sig} = \gamma V_\mathrm{ref}$. $0 < \gamma < 1$ accounts for the lead resistance. However, due to perturbations the actual measured voltage

$$V_\mathrm{in}(t) = V_\mathrm{sig}(t) + V_\mathrm{white}(t) + V_\mathrm{cross}(t) + \ldots \tag{3.6}$$

can contain additional terms like white thermal noise $V_{\text{white}} \propto \sqrt{RT}$ and disturbances from crosstalk $V_{\text{cross}}(t) = \sum_i V_i \sin(\omega_i t + \theta_i)$ consisting of a finite number of perturbations at distinct frequencies and phases. A typical root cause for crosstalk is another experiment that operates at a distinct frequency and emits radiation. However, in this example $V_{\text{cross}}(t)$ summarizes all perturbations with fixed frequency and phase, e.g., constant fluctuations in the power supply. I_{out} would be affected by those perturbations as well, which is neglected at this point. Just note that a time dependent resistance $R(t)$, for example due to electric heating of the resistor, induces higher harmonic responses. A visual representation of Eq. (3.6) with low signal-to-noise ratio is shown in Fig. 3.1. In (a), the different terms $V_{\text{white}}(t)$,

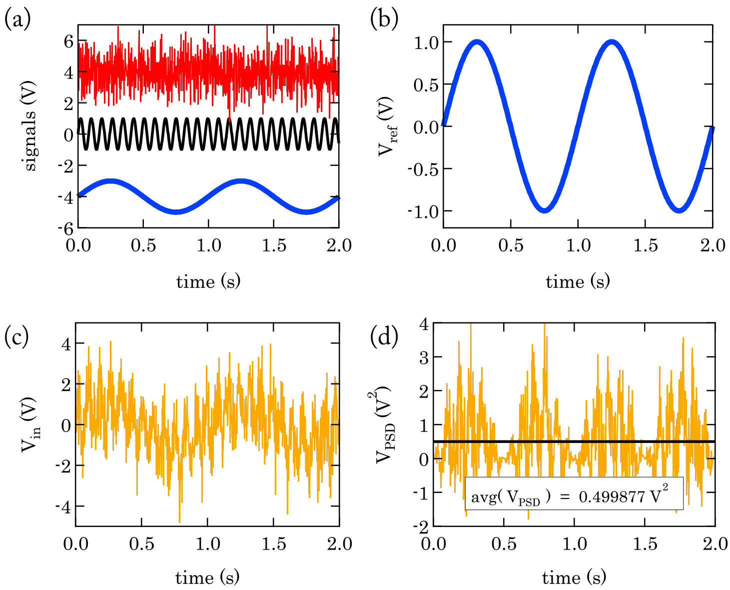

Figure 3.1: A visualization of the Lock-In technique. (a) Possible contributions to the measured signal shown individually. The red, black and blue curves show V_{white}, V_{cross} and V_{sig}, respectively. They are shifted by $[+4, 0, -4]$ V for clarity. (b) A plot of $V_{\text{ref}} = V_{\text{sig}}/\gamma$ with $\gamma = 1$ for ideal leads. (c) The time dependent signal that is recorded by the Lock-In, i.e. $V_{\text{in}} = V_{\text{sig}} + V_{\text{cross}} + V_{\text{white}}$. (d) A plot of $V_{\text{PSD}} = V_{\text{ref}} \cdot V_{\text{in}}$. The black line represents the average value of V_{PSD}. The data used for this figure is generated with the NumPy package in Python.

$V_{\text{cross}}(t) = 1\,\text{V}\,\sin(12.3\omega_{\text{r}})$ and $V_{\text{sig}} = 1\,\text{V}\,\sin(\omega_{\text{r}})$ with $\omega_{\text{r}} = 2\pi\,\text{s}^{-1}$ are drawn in red, black and blue, respectively. V_{white} follows a normal distribution with a width of 1.0, centered at zero and multiplied by $1\,\text{V}$. The frequency $12.3\omega_{\text{r}}$ at which V_{cross} oscillates is chosen at random. (b) is a plot of $V_{\text{ref}} = V_{\text{sig}}/\gamma$ and (c) shows the summation of all terms in (a), i.e. V_{in}. To separate the desired signal from noise and perturbations, the measured voltage is then multiplied with V_{ref}:

$$V_{\text{PSD}}(t) = V_{\text{in}}(t) \cdot V_{\text{ref}}(t) \tag{3.7}$$

The outcome is called Phase Sensitive Detection (PSD). The result is shown in Fig. 3.1 (d). The time average of this curve is $\text{avg}\left(V_{\text{PSD}}\right) = 0.499877\,\text{V}^2$. In fact, this average converges to

$$\text{avg}\left(V_{\text{PSD}}\right) = \frac{V_0^{\text{sig}} V_0^{\text{ref}}}{2} = \frac{\gamma}{2}\left(V_0^{\text{ref}}\right)^2 \tag{3.8}$$

for an infinite measurement interval and therefore allows to calculate the amplitude of the unperturbed voltage drop over the resistor $V_0^{\text{sig}} = \gamma V_0^{\text{ref}}$. Here, $V_0^{\text{sig}} = 2\,\text{avg}\left(V_{\text{PSD}}\right)/V_0^{\text{ref}} = 0.9998\,\text{V}$ is remarkably close to the true value of $1\,\text{V}$. To mathematically proof Eq. (3.8) one has to execute the multiplication in Eq. (3.7) using a generalized representation of V_{in}. An arbitrary ac input signal can be written as the integral

$$V_{\text{in}}(t) = \int_0^{\infty} \text{d}\omega V_0(\omega) \sin\left(\omega t + \theta(\omega)\right) \tag{3.9}$$

over all frequencies ω with individual amplitudes $V_0(\omega)$ and phases $\theta(\omega)$. Using this generalized form Eq. (3.7) turns into

$$\begin{aligned} V_{\text{PSD}}(t) &= \int_0^{\infty} \text{d}\omega V_0(\omega) \sin\left(\omega t + \theta(\omega)\right) \cdot V_0^{\text{ref}} \sin\left(\omega_{\text{r}} t + \theta_{\text{r}}\right) && (3.10)\\ &= \int_0^{\infty} \text{d}\omega V_0(\omega) V_0^{\text{ref}} \sin\left(\omega t + \theta(\omega)\right) \sin\left(\omega_{\text{r}} t + \theta_{\text{r}}\right) && (3.11) \end{aligned}$$

and with the trigonometric identity

$$\begin{aligned} 2\,\sin(\omega_a t + \theta_a)\sin(\omega_b t + \theta_b) = &\cos\left(\left[\omega_a - \omega_b\right] t + \theta_a - \theta_b\right)\\ &- \cos\left(\left[\omega_a + \omega_b\right] t + \theta_a + \theta_b\right) \end{aligned} \tag{3.12}$$

one finds that V_{PSD} is a voltage containing frequencies components of ω_{r} mixed with any ω present in the measured signal. Most frequency mixes result in an ac voltage. The only dc component of V_{PSD} arises from $\omega = \omega_{\text{r}}$

which is, if ω_r is chosen wisely, solely due to the measurement signal $V_\mathrm{sig} = \gamma V_\mathrm{ref}$ [cf. Eq. (3.12): $(\omega_a - \omega_b) = 0$].

Eq. (3.8) allows to calculate V_0^sig by taking the time average of V_PSD which is a possible solution for that problem since the ac components will eventually cancel out if the measurement time is large enough. However, the technical solution used in Lock-In amplifiers utilizes low-pass filter to separate the dc component of V_PSD. This can be done with analog electronics or by a Digital Signal Processing (DSP) chip after digitalization of V_PSD. In electronics, a low-pass filter can be realized by the combination of a capacitor and a resistor with capacitance C and resistance R, respectively. In Fig. 3.2 an example for an RC filter of fourth order is shown. In general, an RC filter is characterized by its order n, i.e. how many identical RC filter are placed in series, and the time constant

$$\textsc{tc} = R \cdot C. \tag{3.13}$$

TC is a measure how long the capacitor needs to be charged if a voltage is applied to the input side of the RC filter. A large capacitor with high capacitance takes longer to charge. The charging time also increases if the charging current is limited by a high resistance. Hence, an oscillating voltage will change its polarity before a significant voltage could build up at the output of the RC filter if TC is large. This damping effect of high frequencies, more precisely of frequencies larger than the cut-off frequency $\omega_\mathrm{c} = \textsc{tc}^{-1}$, is enhanced with each increase of n [cf. Fig. 3.3 (a)]. ω_c is independent of n.

A dc voltage will always pass a low-pass RC filter independent of TC. However, if a dc voltage is switched on or off it is not constant in time

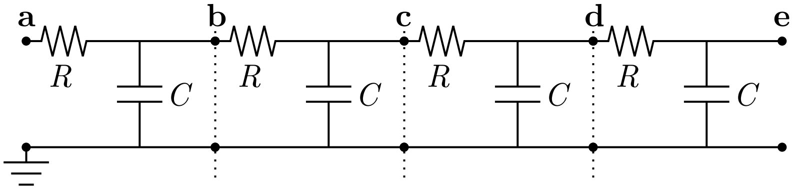

Figure 3.2: A fourth-order RC low-pass filter is constructed by a series connection of four RC low-pass filter with identical time constant $\textsc{tc} = R \cdot C$. The individual filters are visually separated by the dotted vertical lines. The bottom power line is grounded. A time dependent voltage applied to point **a** results in a voltage at point **b** with high frequencies $\omega > \omega_\mathrm{c} = \textsc{tc}^{-1}$ being damped. This process is recursive for point **c**, **d** and **e**, successively enhancing the dampening of high frequencies.

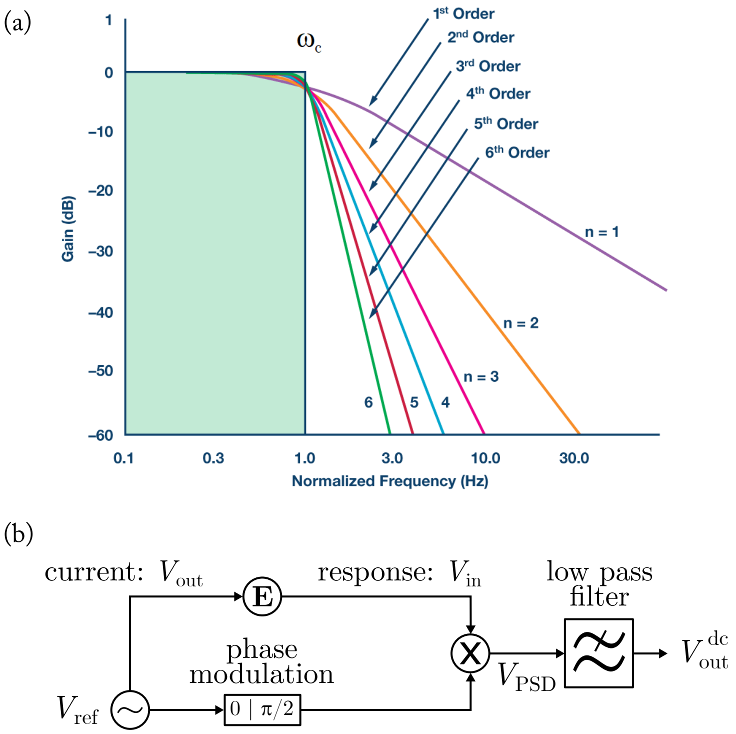

FIGURE 3.3: (a) Frequency dependent dampening of voltages at an RC filter. The filter order n increases the slope of the curve. The cut-off frequency depends on the filter characteristics $\omega_c = \textsc{tc}^{-1} = (RC)^{-1}$. (b) Graphical depiction of the Lock-In technique. An ac reference $V_{\text{ref}}(t)$ excites a driving current $V_{\text{out}}(t)$ to feed a transport experiment **E**. From that experiment, the ac voltage $V_{\text{in}}(t)$ is recorded. $V_{\text{PSD}}(t) = V_{\text{in}}(t) \cdot V_{\text{ref}}(t)$ is calculated with $V_{\text{ref}}(t)$ being optionally phase shifted by $\pi/2$. A low pass filter separates the dc component $V_{\text{out}}^{\text{dc}}$ of $V_{\text{PSD}}(t)$ which is proportional to the experiments in- or out-of-phase response at reference frequency. Subfigure (a) is adapted from Ref. [67].

anymore and the RC filter will therefore react time dependent. The output voltage of an ideal low-pass filter converges with time to the dc input voltage. Practically, a fourth order RC filter needs about $10 \cdot \textsc{tc}$ to level at the equilibrium output voltage. Depending on the filter characteristics the output voltage consists of the dc and low frequency components of V_{PSD}. Hence, in each situation a reasonable TC must be chosen to balance measurement accuracy and time expenditure. This becomes especially important if the observed transport effect is itself time dependent.

A closer look at Eq. (3.12) bares another important detail. The cosine becomes time independent if $\omega_a = \omega_b$ but its value deviates from unity if $\theta_a \neq \theta_b$. Hence, the phase between reference and measured signal is important. The presented algorithm evaluates the in-phase component of the signal with respect to the reference. To obtain the out-of-phase component, the reference signal is phase shifted by $\pi/2$ before executing the multiplication in Eq. (3.7). Although it is not important for this thesis note that Lock-In amplifiers are capable to evaluate the experiments response with respect to the reference frequency ω_r or at integer multiple frequencies, i.e., higher harmonics.

To summarize this section a compact visualization of the Lock-In technique is depicted in Fig. 3.3 (b).

3.3 Computational techniques

Beside the tools available through standard evaluation software, more complex computational methods had to be mastered to accomplish the aim of this thesis. This section conveys a brief introduction to those techniques.

3.3.1 Kinetic Monte Carlo Simulation

Monte Carlo (MC) in general refers to algorithms that treat problems by the use of random numbers [68]. It allows to solve computationally expensive problems with fewer operations compared to a conventional approach. The consequential speed increase is in balance with a loss in accuracy and can be tuned to match the requirements of the problem. A use case for the MC method is solving a complicated integral. The inherent randomness of every MC method becomes handy when dealing with physics that contains randomness itself, such as thermodynamics. Probabilistic events can be described by analytic expressions, e.g., as solutions of rate equations, only for simple systems and large ensembles. Thus, in many cases, a numerical approach is inevitable.

If one is interested in the time evolution of a probabilistic system it is straightforward to utilize a MC method, i.e., kinetic Monte Carlo (kMC) [69]. Note that dynamic Monte Carlo is often used synonymously to kMC. In general, kMC is applicable to systems that can be described entirely by a potential-energy surface (PES). Then, the possible states of the system are given by the local minima of the particular PES. The time evolution is regarded as hops from one state into another. Hopping itself is a stochastic process where the hopping probability captures the physics of the system and is usually linked to the PES. In each iteration of a hopping process, representing a discrete time step, the hopping probability is compared to a random number which decides whether the hop takes place, or not. The code that was used for this thesis has been developed by Prof. Dr. Markus Meinert with additions by the author of this thesis. It is written in Python and was executed parallelized on a remote workstation with 32 cores.

3.3.2 Finite-Element-Method

The Finite-Element-Method (FEM) is used to find approximative solutions for sets of partial differential equations (PDEs) [70]. PDEs are essential to describe a large variety of physical phenomena including electrostatics, which classifies the problems that had to be solved within this thesis. In particular, equilibrium current density distributions in arbitrarily shaped two dimensional devices were studied using the FEM. For this kind of problem, the algorithm has to approximate the solution of the Poisson equation

$$-\hat{\epsilon}\,\nabla^2\phi = \rho_\mathrm{c}. \tag{3.14}$$

ϕ is the electrostatic potential that is linked to the voltage $V = \Delta\phi = \phi_i - \phi_j$ and $\hat{\epsilon}$ is the permittivity tensor. Note that the permittivity tensor includes the conductivity and, thus, Ohm's law. ρ_c is the charge density which, through the continuity equation

$$-\nabla \boldsymbol{j} = \dot{\rho}_\mathrm{c}, \tag{3.15}$$

is related to the current density $\boldsymbol{j}$. As the first step of the FEM a given device shape with specified boundary conditions and material parameters is partitioned into a finite number of elements. This procedure is called meshing. These finite elements can have any form but are typically triangular. Secondly, a polynomial function as approximation for the fundamental PDE, here for Eq. (3.14), is derived and solved for each triangle with matching boundary conditions of neighboring triangles. From that solution one can derive the current density at each point via Eq. (3.15). The FEM is by its construction only an approximation but its precision can be adjusted by varying the size of each triangle, which is in balance with the computation time.

The FEM analysis in this thesis was done with COMSOL Multiphysics and FEMM. Both softwares need as input the device geometry, boundary conditions and material parameters. Hence, they are easy-to-use and do not require a detailed understanding of the underlying algorithms. COMSOL is a highly sophisticated FEM software package that allows to do three dimensional FEM simulations with the possibility to couple various physical problems, e.g., a current generates heat and, thus, changes the resistivity which eventually results in a nontrivial current density distribution at equilibrium. This software, however, is available only with a subscription of considerable price. A license was available through the Bielefeld University of Applied Science only while Christian Mehlhaff and Lukas Neumann worked on their Master's theses [71, 72]. FEMM, on the other hand, is a free software with limited functionality in comparison to COMSOL [73, 74]. However, it can calculate current density profiles in two dimensional structures which is the required functionality for this thesis. Therefore, most FEM simulations were executed using FEMM (version 4.2).

3.4 Setup of the NSOT transport experiment

To perform a transport experiment, it is necessary to guide a current, in this case an electrical current, in a specific direction and measure a voltage between points with well-known location in relation to that current. Hence, plane thin-film samples are typically patterned into devices by the use of lithography [cf. Sec. 3.1.4]. In Fig. 3.4 images of the two variants of the used device are shown. Due to the similarity to the national flag of the United Kingdom this device type will be referred to as *Union Jack* device.

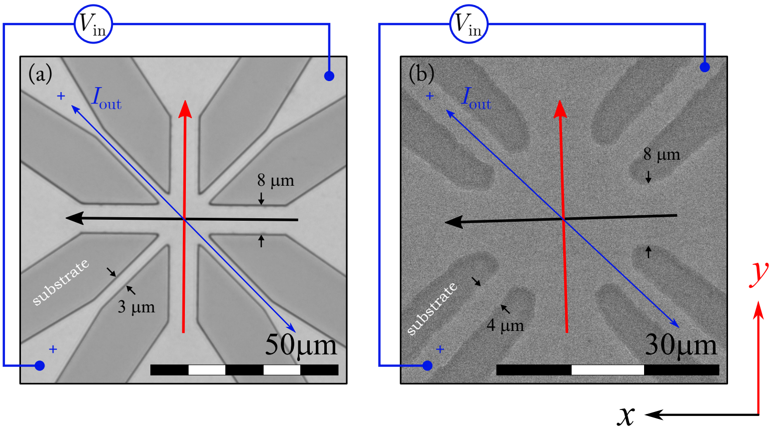

Figure 3.4: Images of the *Union Jack* devices with an overlay depicting the measurement geometry. The nomenclature of the pulse lines is defined by the coordinate system. (a) A greyscale optical micrograph of a device patterned using EBL. The current channels are 8 and 3 µm wide. (b) UVL patterned device with current channels of 8 and 4 µm width. The image is recorded with a SEM.

The *Union Jack* devices are designed to guide current pulses either in x or y direction trough the 8 µm wide channels which will be called pulse lines in the following. The pulses are characterized by their pulse width Δt and current density $j = |\boldsymbol{j}|$. If multiple pulses are bunched to a burst, the number of pulses per burst and the duty cycle separating subsequent pulses are additional parameters. The black and red arrows in Fig. 3.4 represent the technical current direction for $j > 0$, e.g., in the image the electrons are moving from left to right for a positive current density being applied to the x pulse line. The narrow channels are the probe lines. They are used to investigate the response of the film to the pulses using a PHE measurement geometry, i.e., the voltage is measured perpendicular with respect to the probe current. The transport measurement is done with a Lock-In amplifier (Zurich Instruments MFLI) and the polarity marked in the figure correspond to the colors of the outputs and inputs of the Lock-In. The evaluated quantity is the perpendicular resistance [cf. Fig. 3.3 (b)]

$$R_\perp = \frac{V_{\mathrm{out}}^{\mathrm{dc}}}{I_{\mathrm{out}}}. \tag{3.16}$$

I_{out} is measured as voltage drop over a series resistor with known resistance. There are various physical effects that are responsible for the response to a current pulse of considerable intensity. Hence, the investigated phenomenon will be introduced in the respective chapter individually. The experimental setup for the transport measurement, however, is very similar throughout this thesis and independent of the involved physics.

The electrical setup that facilitates a successive burst generation and $R_\perp$ measurement is shown as a circuit diagram in Fig. 3.5. The bursts are generated by an arbitrary waveform generator (Agilent 33522A) in combination with a differential broadband amplifier (Tabor Electronics 9260) that has a fixed amplification factor of x10 and provides a differential output voltage of $\leq$ 34 V. The pulse form is monitored with a digital storage oscilloscope (UNI-T UTD2052CEX) which is connected directly to the output of the Tabor amplifier. A switchbox containing reed relais directs the bursts either to the x or y pulse line while keeping the Lock-In disconnected during the burst to avoid an overload of the Lock-In amplifiers input. Additionally, the $R_\perp$ measurement would become corrupted if the broadband amplifier with is finite lead resistance is connected to the device during the measurement. Hence, the switchbox facilitates open circuit conditions for the pulse lines during probing as well. Optionally, the sample is placed in a closed-circuit He cryostat allowing to vary the sample temperature $T_{\mathrm{s}} \leq 290\,\mathrm{K}$. Before each sequence, the pulse line resistances $R_{x,y}(T_{\mathrm{s}})$ are checked with two-point resistance measurements using a Keithley 2000 multimeter. The

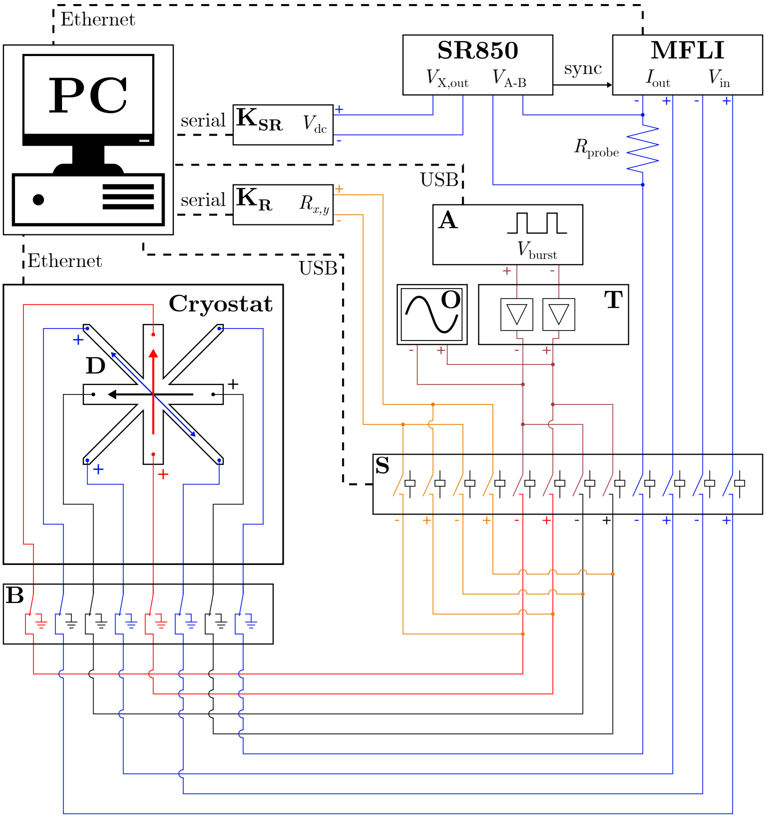

Figure 3.5: Circuit diagram of the transport experiment. The usage of the cryostat and the SR850 Lock-In is optional. Dashed lines represent data connections while solid lines are BNC cables with an impedance of $50\,\Omega$ used to measure voltages or to push currents. **B** is the breakout box, **S** is the switchbox, **T** is the Tabor amplifier, **O** is the oscilloscope and **A** is the Agilent waveform generator. $\mathrm{K_R}$ and $\mathrm{K_{SR}}$ are Keithley 2000 multimeters. Note that the Tabor amplifier inverts the polarity. All dynamic components are regulated by the **PC** which allows for a completely automated measurement. The color code is adapted from Fig. 3.4, complemented by orange and burgundy. Orange accounts for the connections to measure $R_{x,y}$ and burgundy, which is a mix of red and black, highlights the lines carrying the pulse voltage which are not yet assigned to either the x or y pulse line.

pulse voltage

$$V_{x,y}(T_\mathrm{s}) = j\,wh\,R_{x,y}(T_\mathrm{s}) \tag{3.17}$$

is adjusted accordingly to obtain the set current density. w and h are the current line width and film thickness, respectively. In each pulse, the voltage is ramped linear to $V_{x,y}$ during a well defined ramp-up and ramp-down time $t_{\text{ramp}-\text{up}} = t_{\text{ramp}-\text{down}} = t_\text{ramp} = \min(0.25\,\Delta t, 1\,\mu\text{s})$. The charge that is transferred in a pulse is unaffected by this procedure. A breakout box that can ground the sample using mechanical switches is installed between the device and the switchbox. It is primarily used during sample changes. A second Lock-In amplifier (Stanford Research Systems SR850) is used to determine the magnitude of the probe current I_out. Both Lock-In amplifiers use identical settings and are phase locked. If no second Lock-In was available, the voltage drop over the series resistor was measured with a Keithley multimeter directly.

A schematic illustration of the sequence that is considered as one experiment is shown in Fig. 3.6. Before the first and after each burst, $R_\perp$ is evaluated at the reference frequency $f_\text{ref} = 81.3\,\text{Hz}$ using a fourth-order low-pass filter with TC $= 100\,\text{ms}$. Hence, a delay of 2 s between burst and the recording of $R_\perp$ is set to ensure an equilibration of V_out^dc [cf. Eq. (3.16)]. The bursts are designed to transport a constant charge per burst Q trough

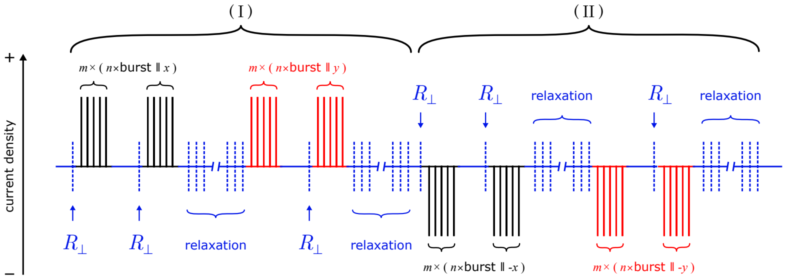

Figure 3.6: Schematic illustration of the measurement sequence for a transport experiment. The color code is matched to the arrows in Fig. 3.4. Prior to each burst, $R_\perp$ is measured with an ac probe current. The probe current density is at least two orders of magnitude smaller compared to the burst currents. The time evolution of $R_\perp$ is monitored for the duration T_relax after n bursts have been applied to one pulse line. Bursts are applied with varying polarity in subsequent parts labeled with (I) and (II).

the structure by adjusting the number of pulses per burst

$$N(\Delta t, j) = Q \ (\Delta t \, j \, wh)^{-1} \tag{3.18}$$

in dependence of other experimental parameters. After n bursts along x, the time evolution of $R_\perp$ is observed over the so-called relaxation time T_{relax} with measurements every second. The same scheme is executed for bursts parallel to the y-direction, forming part (I) of the sequence. Part (II) is a repetition of (I) with inverted polarity of the current pulses. A complete experiment for a given set of parameters consists of m full repeats of each part, i.e. m times part (I) followed by m times part (II).

The *Union Jack* devices do not promote a homogeneous current flow in the center region of the device. This affects the pulse and the probe current alike. Thus, a FEM simulation is set up to determine the actual current density distribution [cf. Sec. 3.3.2]. The results for the switching pulse and the probe current, calculated with COMSOL, are shown in Fig. 3.7. The current flow is inhomogeneous with hot spots at the corners, which is a similar result obtained for 4-arm Hall crosses [2]. For pulsing, the current density in the center of the device reads 55% of the current density in the leads, which is the nominal applied current density j, while it is increased up to 185% of the lead current density in the hot spots. Hence, *whatever* effect is driven by that current will vary locally in magnitude. Note that compared to the 4-arm crosses the area of nearly homogeneous current density is quite large.

The same is true for the probe current density $\boldsymbol{j}_{\text{probe}}$ which results in a locally varying sensitivity of the experiment [cf. Fig. 3.7 (b)]. The eventually measured voltage $V_\perp$ originates primarily from electrical fields $\boldsymbol{E}$ that are in between the pick-up leads, which can be estimated by the line integral

$$V_\perp = \int_{\boldsymbol{r}} \boldsymbol{E}(\boldsymbol{j}_{\text{probe}}) \cdot \mathrm{d}\boldsymbol{r} \tag{3.19}$$

along the curve $\boldsymbol{r}$. Following this simplistic view one can conclude that a large portion of $V_\perp$ originates from the central region of the *Union Jack* device. Hence, the measurement is mostly sensitive on the effect size in this region and therefore center region current density

$$j_{\text{CR}} = 0.6\, j \tag{3.20}$$

is introduced which is especially important for quantitative analyses.

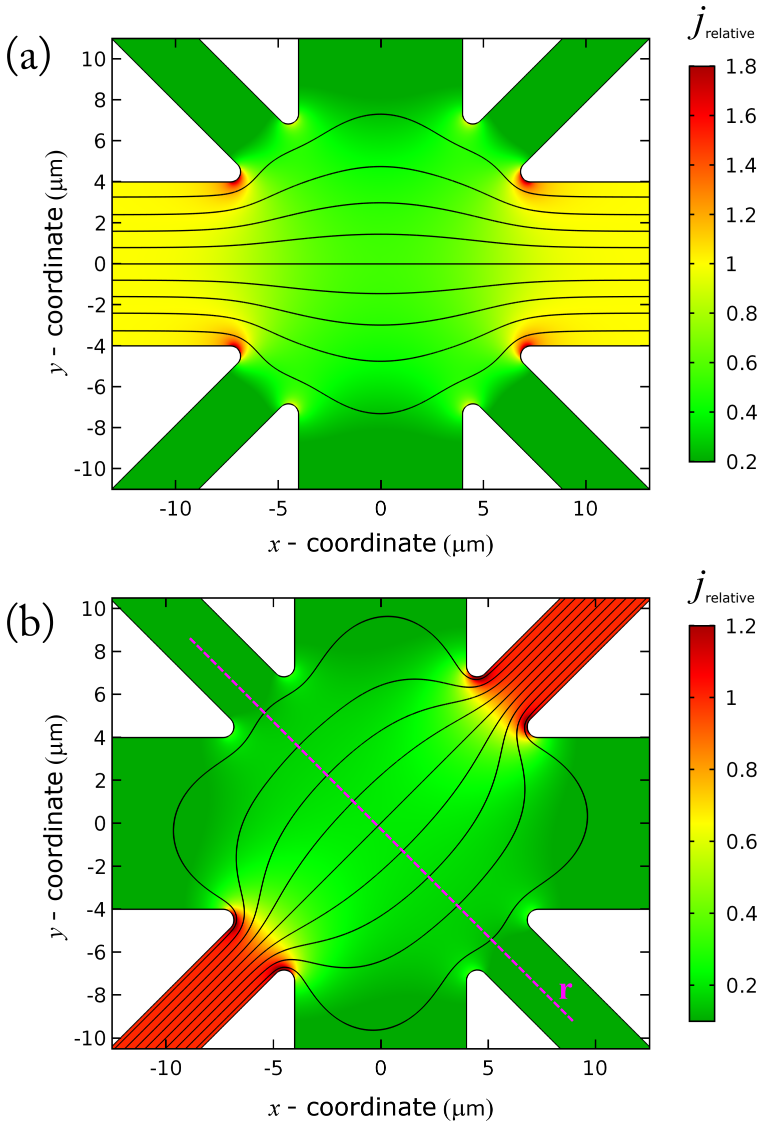

FIGURE 3.7: FEM simulation of the relative current flow distribution in a *Union Jack* device with pulse line width of 8 µm and probe line width of 3 µm. (a) For a constant voltage being applied at the pulse line in x-direction. (b) For a constant voltage being applied at the probe line in (x, y)-direction. The purple line points in $(-x, -y)$-direction.

Néel-order spin-orbit torque switching in sputtered CuMnAs

4

This chapter comprises the key results of this thesis, which have been obtained from switching experiments on tetragonal CuMnAs thin films that were deposited by dc-magnetron sputtering. From first switching experiments on Mn_2Au, which were conducted in the course of the Master's thesis of Dominik Graulich, it became obvious that the NSOT theory alone cannot describe the obtained results [75]. Thus, the first output in conjunction to this work is an extension to the NSOT theory that regards the switching as a thermally activated mechanism [2]. The experience gained from these preliminary experiments lead to an extensive series of experiments on tetragonal CuMnAs [4]. In particular, the switching characteristics were investigated in dependence of the sample temperature T_s, the pulse current density j, and the pulse width Δt. All found dependencies are in striking agreement with the extension to the NSOT theory [cf. Sec. 2.3]. The results are shown in Sec. 4.2. As final consistency check a kMC simulation is applied to resemble the switching, again, with good agreement [cf. Sec. 4.4].

4.1 CuMnAs sample preparation and characterization

The NSOT is only present in materials that obey symmetry requirements described in Sec. 2.2. In this thesis, tetragonal CuMnAs is used as this material. To perform a transport experiment in which the current is guided parallel to either the crystallographic a or b axis the thin film needs its tetragonal symmetry axis, the c axis, pointing in oop direction. In the following, this process which eventually results in a working device for NSOT switching will be outlined. A series of CuMnAs films are deposited by dc-magnetron sputtering from a composite target with $Cu_{0.3}Mn_{0.3}As_{0.4}$ stoichiometry on HCl-etched GaAs (001) substrates [cf. Sec. 3.1.1]. Prior to the deposition, the substrate is heated to 400 °C or 410 °C and kept at the respective temperature for 10 minutes to clean the GaAs surface. Afterwards, the sample is cooled down to the deposition temperature T_d. All CuMnAs samples are capped with Ti which is deposited after cooling down to room temperature.

XRD measurements done at samples deposited at different T_d are shown in Fig. 4.1. At high temperatures, the CuMnAs crystallizes highly oriented in the desired phase with an oop lattice parameter $c = 6.286\,\text{Å}$. The c axis of these samples is 0.5 % shorter if compared to samples prepared by MBE [76]. With decreasing T_d the $(00\,l\,)$ peaks decrease in intensity and a (110) peak arises close to the GaAs (002) substrate peak. From Fig. 4.1 alone one can tell that a high $T_\mathrm{d} \geq 400°\mathrm{C}$ is necessary to grow CuMnAs films of good crystalline quality. Repeatability tests for various T_d show that a bad crystal growth is obtained randomly if the surface cleaning is done at 400 °C. This issue is solved by increasing the cleaning temperature to 410 °C. Hence, samples used for further experiments are cleaned at 410 °C for 10 minutes and, out of convenience, the deposition temperature is chosen

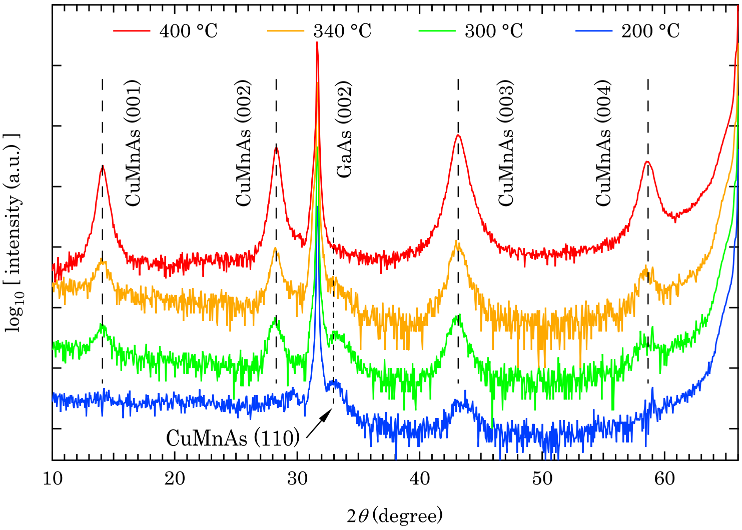

Figure 4.1: XRD measurements of Ti capped CuMnAs films with nominal film thicknesses $h_\mathrm{CuMnAs} = 100\,\mathrm{nm}$ grown at various deposition temperatures T_d. The curves are shifted vertically for clarity. The steep intensity increase for $2\theta > 64°$ is due to the (004) peak of the GaAs substrate. For $T_\mathrm{d} < 400°\mathrm{C}$ a CuMnAs (110) peak is visible around $2\theta = 33.25°$. For $T_\mathrm{d} = 400°\mathrm{C}$ this peak vanishes which indicates a highly oriented growth of the CuMnAs crystallites. Furthermore, the peaks become narrower for higher T_d. This is related to larger CuMnAs crystallites in oop direction [cf. Eq. (3.2)].

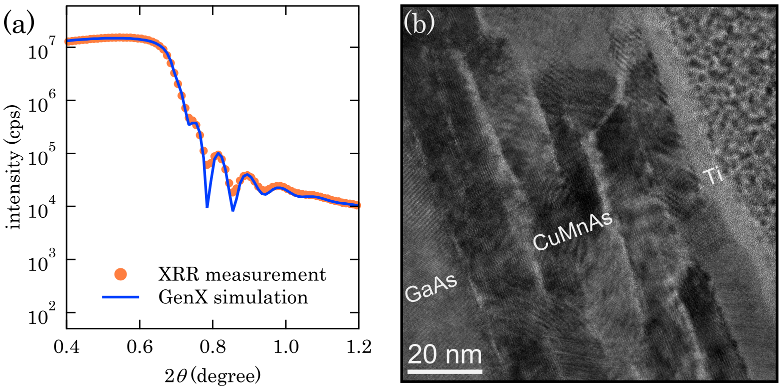

FIGURE 4.2: (a) XRR and (b) TEM measurement of a CuMnAs sample grown at 410°C. The nominal thickness is $h_{\mathrm{nom}} = 80\,\mathrm{nm}$ while the actual thickness, obtained consistently from the TEM image and the XRR fit, reads $h = 68\,\mathrm{nm}$. The film roughness of $4.6 \ldots 5.0\,\mathrm{nm}$ obtained by the XRR fit is consistent with the SFM result of $R_{\mathrm{RMS}} = 4.8\,\mathrm{nm}$.

as $T_{\mathrm{d}} = 410\,^{\circ}\mathrm{C}$ as well. The film is sputtered from an off-stoichiometric target but has a $1:1:1$ stoichiometry within the accuracy of the available XRF experiment. Films grown at $T_{\mathrm{d}} = 410\,^{\circ}\mathrm{C}$ have a high surface roughnesses of $R_{\mathrm{RMS}} = 4.8\,\mathrm{nm}$ which is quantified by SFM measurements. Hence, fitting XRR curves becomes tricky since oscillations are only visible up to $2\theta \approx 1^{\circ}$, as seen in Fig. 4.2 (a). The shown fit, however, appears to be reasonable since its results are consistent with the TEM and SFM results. Fig. 4.2 (b) shows a TEM image of a lamella cut parallel to the (110) direction of the GaAs substrate. A detail view of the GaAs–CuMnAs interface can be seen in Fig. 4.3 (a) with the visible tetragonallity of the CuMnAs unit cell. Since the $(a\,\mathrm{or}\,b) - c$ plane is visible in the picture the basal plane of the CuMnAs has to grow rotated by 45° with respect to the GaAs surface unit cell. This is expected since $a_{\mathrm{CuMnAs}} = b_{\mathrm{CuMnAs}} = 3.82\,\text{Å}$ [76] fits to $a_{\mathrm{GaAs}} = b_{\mathrm{GaAs}} = c_{\mathrm{GaAs}} = 5.65\,\text{Å}$ [77] only for a rotated growth, i.e. $\sqrt{2} \cdot 3.82\,\text{Å} = 5.40\,\text{Å}$ ($\sim 4.5\%$ mismatch). Note that the GaAs has an fcc structure. Energy-dispersive x-ray spectroscopy (EDX) done in the TEM shows the presence of oxygen throughout the Ti film and in the bright areas of the CuMnAs layer [cf. Fig. 4.3 (b) - (d)]. Since CuMnAs likely oxidizes under ambient conditions this oxygen accumulation is most likely related to the TEM preparation process which includes contact to air. Nevertheless, the oxidation is limited to certain areas of the film, indicating that the crystal is more vulnerable to oxygen in these regions. These weak spots can be interpreted as grain boundaries. This reasoning is consistent with Scherrer's formula, Eq. (3.2), which calculates an oop crystallite size of $L_c \approx 10\,\mathrm{nm}$ from the XRD peak widths. Note that the EDX result also assures that

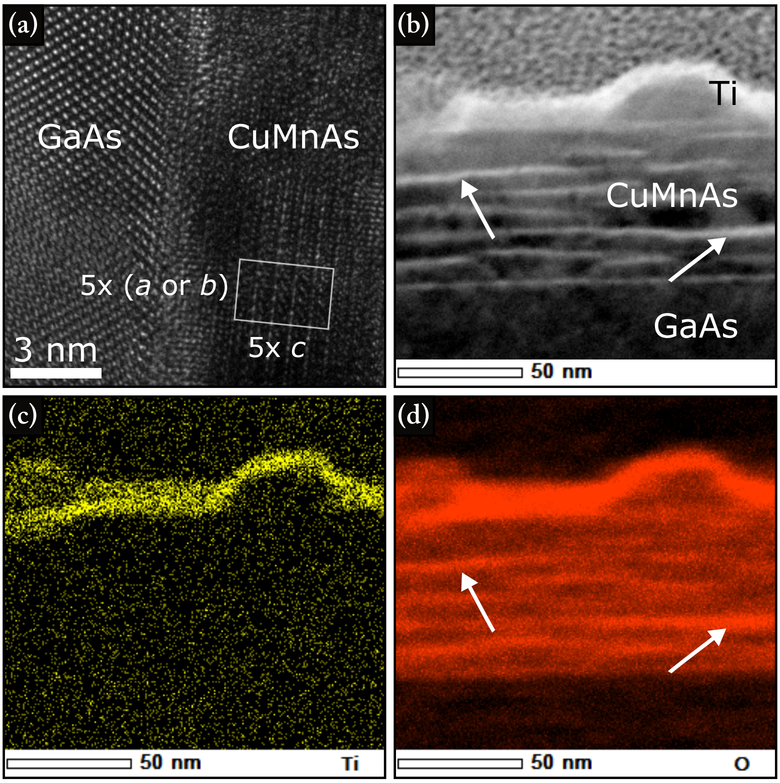

Figure 4.3: (a) Detail view of the GaAs / CuMnAs interface. The white rectangle spans over five CuMnAs unit cells and highlights the tetragonal distortion. The observed dimensions fit to the asserted rotated growth. (b) TEM image used for an EDX analysis. The two arrows point on large white areas within the CuMnAs layer which turn out to be oxygen rich [cf. (d)]. (c) EDX result for Ti concentration. (d) EDX result for O concentration. The capping layer is completely oxidized but no significant oxidation penetrates the CuMnAs. Areas that are bright in (b) show a high oxygen concentration.

the Ti film works well as non-conducting capping layer that protects the CuMnAs from bulk oxidation.

The sample on which the transport experiments are conducted has the stack design GaAs / CuMnAs 68 nm / Ti 5nm. The electrical resistivity $\rho \approx 430\,\mu\Omega\,\mathrm{cm}$ of the CuMnAs is estimated using four-point measurements assuming negligible conduction in the Ti capping [cf. Sec. 3.1.3]. After the growth and basic characterization multiple *Union Jack* devices are patterned onto the sample by EBL [cf. Fig. 3.4 (a)]. The structured sample is then glued into an C-DIP and randomly selected devices are contacted by Al-wire bonds. Here, two neighboring devices on the same sample are used. The j and Δt variations are performed on the same device, whereas the T_s variation is done on the second one. The final sample package is then placed in a closed-cycle He cryostat with electrical feedthroughs.

4.2 Experimental findings on CuMnAs

Pulsing experiments as described in Sec. 3.4 are performed with ranges of sample temperatures T_s, current densities j, and pulse widths Δt. The pulses are expected to rotate the Néel vector $\boldsymbol{L}$ via the NSOT mechanism, explained in Sec. 2.2. The state of $\boldsymbol{L}$ is evaluated by a Lock-In measurement of the transverse resistance using the narrow probe lines. Since the transverse resistance is expected to originate from the orientation of the magnetic system, i.e. via the PHE, the recorded quantity is labeled as planar Hall resistance R_PHE. Note that the distinction whether the transverse resistance has a magnetic origin becomes important in Chap. 5. Exemplary data is shown in Fig. 4.4 (a) where R_PHE is drawn as a function of the elapsed time. Alternating the direction of pulsing switches the system between high and low values of R_PHE where the change is independent of the current-polarity as expected for the NSOT mechanism. A weak polarity dependence remains, i.e. R_PHE drifts to higher values during part (I) and to lower values in part (II). This polarity dependent contribution may originate from torques that arise in the domain walls of the AFM [53]. Nevertheless, the contribution is very small and will be removed throughout the thesis by taking the polarity average, as plotted in Fig. 4.4 (b). The curve is color coded to match the pulsing sequence introduced with Fig. 3.6 and an offset arising from imperfect lithography is removed, i.e. the curve is centered around zero. The set magnetic state is thermally unstable as seen from the decay of ΔR_PHE during the relaxation of length $T_\mathrm{relax} = 600\,\mathrm{s}$. However, the experiment demonstrates perfectly reproducible switching of R_PHE with a slight asymmetry with respect to the pulsing direction.

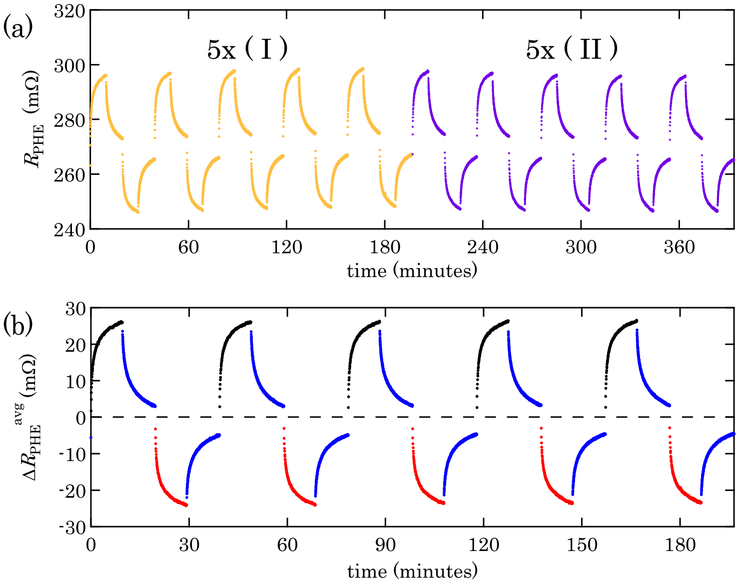

FIGURE 4.4: (a) R_{PHE} versus time trace at $T_s = 260$ K, $j = 5.9 \times 10^{10}$ A/m^2 and $\Delta t = 5$ µs. Different polarity of the current pulses in part (I) and (II) is highlighted by different colors. (b) Average over (I) and (II) plotted in colors matched to the pulsing scheme in Fig. 3.6. A constant offset of ΔR_{PHE} is removed.

The first switching cycle of a T_s variation is shown in Fig. 4.5. The x axis is split with burst number as the parameter for the pulsing phase and time as the parameter for the relaxation phase. The temperature not only affects the amplitude of the switching, but also changes the overall shape, e.g. the steepness. However, the curve shape is similar for different T_s, which holds true for different j and Δt as well. To comprehensively visualize the features of the switching curves in dependence on the varied parameters one has to compress these features into quantitatively comparable characteristic parameters. A procedure to achieve this is described in the following section.

4.2.1 Quantification of switching characteristics

The magnetically set state is thermally unstable which is a proof that the switching energy barrier is in the order of the thermal energy. Hence, the thermal-activation model introduced in Sec. 2.3 can be used to extract mi-

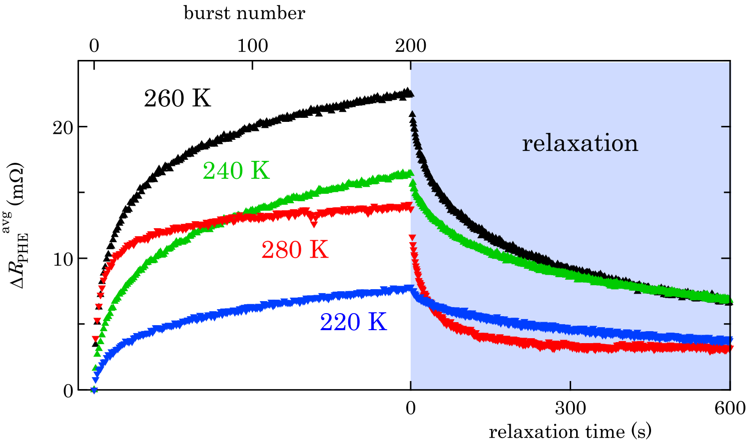

FIGURE 4.5: First switching cycle for pulses $\parallel x$ using $j = 6.47 \times 10^{10}$ A/m^2 and $\Delta t = 1$ µs and different T_{s}. The curves are shifted to start at $\Delta R_{\mathrm{PHE}}^{\mathrm{avg}} = 0$ individually. Pulsing and relaxation are plotted on separate x-axis at the top and bottom of the graph, respectively.

croscopic parameters of the system from the collected data. The decay of the magnetic system with no current applied, described by Eq. (2.58) in Sec. 2.3.1, allows to evaluate the microscopic energy barrier $E_{\mathrm{B}} = K_{4\parallel} V_{\mathrm{g}}$ via the Néel-Arrhenius equation (2.51). E_{B} depends on the volume of the ensemble of grains that have been switched and, thus, a film of grains that follow a grain size distribution will manifest in a superposition of different relaxation times τ_i. Hence, the general fitting function for the relaxation reads

$$\Delta R_{\mathrm{PHE}}(t) = \sum_{i=0}^{n} d_i \exp\left(-\frac{t}{\tau_i}\right) . \tag{4.1}$$

n gives the number of exponential functions used and d_i are the weights. Alternatively, one may use stretched exponentials to describe the ensemble when the relaxation times are dense [3, 78]. However, the simple sum of exponentials provides a more transparent picture. n should be as small as possible to limit the number of free parameters and, therefore, avoid overfitting. On the other hand, n must be large enough to find good agreement between the model function and the data. As seen in Fig. 4.6 three terms of the form

$$\Delta R_{\mathrm{PHE}}(t) = d_0 + d_1 \, \exp\left(-\frac{t}{\tau_1}\right) + d_2 \, \exp\left(-\frac{t}{\tau_2}\right) \tag{4.2}$$

during relaxation are sufficient to describe the observed switching curve reasonably well and additional exponentials do not further improve the result. $d_0 \approx d_0 \exp\left(-t/\tau_0\right)$ corresponds to an exponential function with $\tau_0 \gg T_{\mathrm{relax}}$.

An analytic expression that describes the switching amplitude per burst $\left|\Delta R_{\perp}^{\mathrm{burst}}\right|$, cf. Eq. (2.63), has been derived in Sec. 2.3.2. The requirement of a uniform orientation of $\boldsymbol{L}$ is approximatively given after T_{relax} and, hence, the steepness of the switching curve at burst number $b = 0$ is a good estimation for $\left|\Delta R_{\perp}^{\mathrm{burst}}\right|$. Taking the numerical derivative on the measured data turns out to be relatively unstable. Therefore, a purely phenomenological fit is applied to the data to take the derivative analytically. Interestingly, Eq. (4.1) is also well suited to model the pulsing phase. However, different variables need to be used, i.e., time is replaced by burst number and the decay parameter is replaced by a dimensionless quantity μ_i with no direct physical

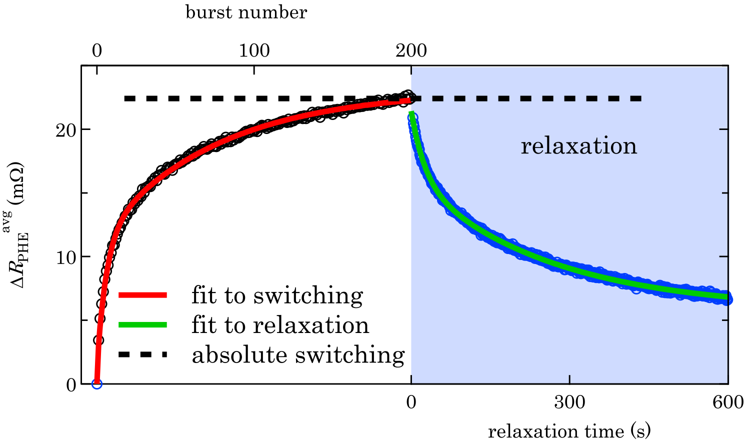

Figure 4.6: Plot of the data taken at $T_{\mathrm{s}} = 260\,\mathrm{K}$ already shown in Fig. 4.5 using the color code introduced with Fig. 3.6. The solid lines in red and green are piecewise fits using Eq. (4.3) and (4.2), respectively. Pulsing and relaxation are plotted on separate x-axis.

meaning. Thus, the pulsing phase is fitted with

$$\Delta R_{\mathrm{PHE}}(b) = c_0 + c_1 \exp\left(-\frac{b}{\mu_1}\right) + c_2 \exp\left(-\frac{b}{\mu_2}\right). \tag{4.3}$$

b represents the burst number, $\mu_{1,2}$ and $c_{0,1,2}$ are fit parameters. The steepness of the switching curve, called switching efficiency R_e in the following, is then calculated as

$$R_\mathrm{e} = \left|\frac{\mathrm{d}(\Delta R_{\mathrm{PHE}}(b))}{\mathrm{d}b}\right|_{b=0} = \left|-\frac{c_1}{\mu_1} - \frac{c_2}{\mu_2}\right| \approx \left|\Delta R_{\perp}^{\mathrm{burst}}\right| \tag{4.4}$$

by taking the derivative of Eq. (4.3) at $b = 0$. The good agreement between the model function and the data for $n = 3$ suggests that the real grain size distribution can be characterized by three distinct grain sizes V_g^i that relate to the energy barriers $E_\mathrm{B}^i = K_{4\|} V_\mathrm{g}^i$. The relative occurrence of each grain size does not change between pulsing and relaxation and, hence, one would expect $c_1/c_2 = d_1/d_2$. Implementing this constraint into the fitting routine greatly improves the stability of the fit which is the first evidence that the thermal-activation model is self-consistent.

To obtain R_e and $\tau_{1,2}$ the averaged data is fitted piecewise using Eq. (4.2) and (4.3). Those characteristics can be calculated for each switching cycle where the signal-to-noise ratio is sufficiently large to apply the fit. Additionally, the difference of R_{PHE} before and after applying n bursts along one axis is defined as the absolute switching amplitude $|\Delta R_\mathrm{a}|$ [cf. Fig. 4.6].

4.2.2 Dependence of the switching characteristics on sample temperature, current density, and pulse width

R_e, $|\Delta R_\mathrm{a}|$, τ_1, and τ_2 for different parameter sets $\{T_\mathrm{s}, j, \Delta t\}$ are shown in Fig. 4.7, 4.8, and 4.9, respectively. In each experiment 10 switching cycles are recorded which are analyzed independently. The shown data represents the mean values. The results differ slightly between pulsing along x or y. Hence, standard deviations are calculated separate for each pulsing direction and the greater value is taken as error to reflect the reproducibility.

By taking the logarithm of Eq. (2.63) one obtains

$$\ln\left[R_\mathrm{e}\right] \approx \ln\left[\left|\Delta R_{\perp}^{\mathrm{burst}}\right|\right] \propto \frac{xL\chi V_\mathrm{g} j}{k_B T V_\mathrm{c}} - \frac{E_\mathrm{B}}{k_B T} \tag{4.5}$$

as prediction of the thermal-activation model. The dependency of $\ln\left[R_\mathrm{e}(T_\mathrm{s})\right]$ on T_s and j is explicitly captured:

$$\ln\left[R_\mathrm{e}(T_\mathrm{s})\right] \propto -\frac{1}{T_\mathrm{s}} \qquad \text{and} \qquad \ln\left[R_\mathrm{e}(j)\right] \propto j \tag{4.6}$$

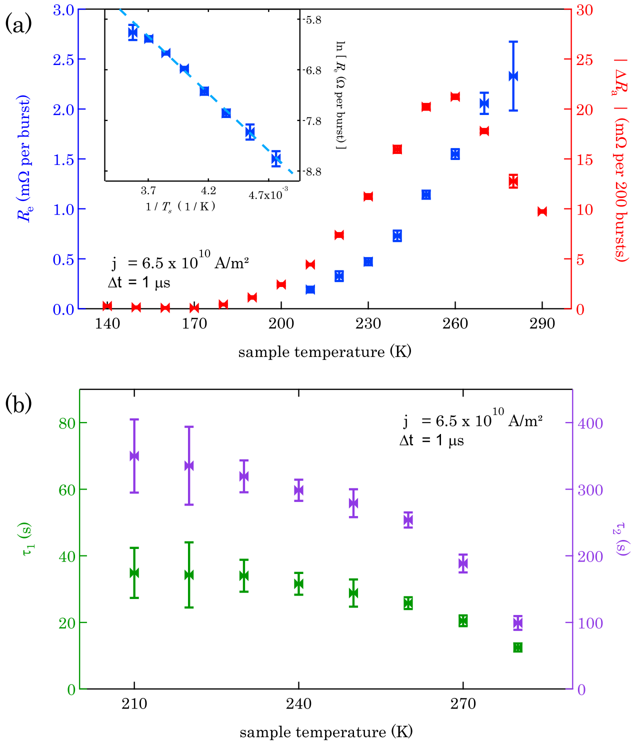

Figure 4.7: Plot of (a) R_e and $|\Delta R_\mathrm{a}|$ and (b) $\tau_{1,2}$ in dependence of the sample temperature T_s with fixed $j = 6.5 \times 10^{10}\,\mathrm{A/m^2}$ and $\Delta t = 1\,\mu\mathrm{s}$. The inset in (a) shows Arrhenius plot of R_e including a line fit disregarding the data point at $1/280\,\mathrm{K}^{-1}$. $\tau_{1,2}$ depends on T_s as expected for a thermally unstable system.

From Eq. (4.5) no Δt dependency is predicted. However, the temperature rise during a pulse, given by You's formula (2.50), is not implemented in the analytic derivation. Due to the higher device temperatures obtained from longer pulses an increase of R_e and $|\Delta R_\mathrm{a}|$ in dependence of Δt is expected. Weather this dependency will be linear, quadratic or indiscriminately, cannot be told from the thermal-activation model.

In Fig. 4.7 (a) one sees that $|\Delta R_\mathrm{a}|$ has a local maximum at $T_\mathrm{s} = 260\,\mathrm{K}$ and it decreases to zero for low T_s. From the maximum absolute switching amplitude one can calculate the maximum resistivity change due to the magnetic switching to $\Delta\rho = |\Delta R_\mathrm{a}| \cdot 68\,\mathrm{nm} = 0.68\,\mu\Omega\,\mathrm{cm}$. Hence, the lower

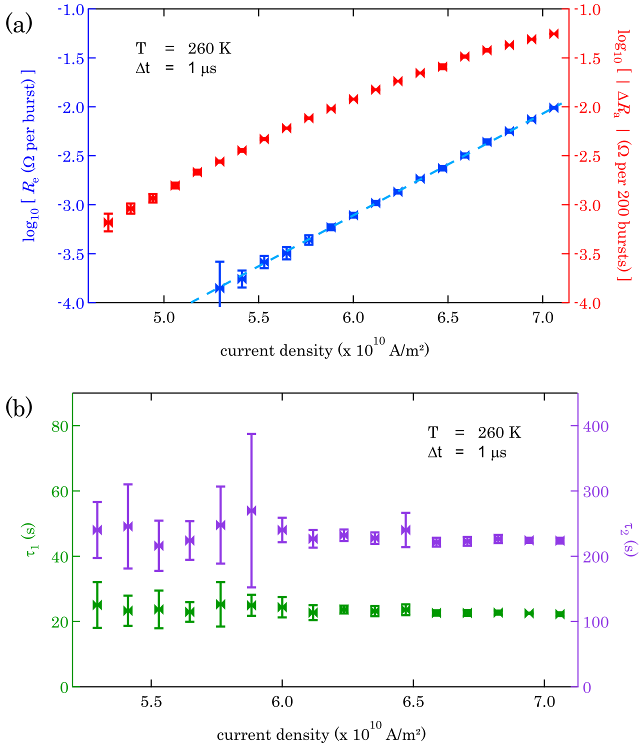

Figure 4.8: Plot of (a) $\log_{10}[R_e]$ and $\log_{10}[|\Delta R_a|]$ and (b) $\tau_{1,2}$ in dependence of the current density j with fixed $T_s = 260\,\text{K}$ and $\Delta t = 1\,\mu\text{s}$. The line in (a) is a linear regression to $\log_{10}[R_e]$, validating an exponential dependence $R_e(j)$. $\tau_{1,2}$ is independent of j.

limit of the AMR ratio reads $\Delta\rho/\rho = 0.14\%$. R_e monotonically increases with increasing T_s. The inset shows an Arrhenius plot of R_e, i.e. $\ln[R_e]$ is plotted against $1/T_s$. The resulting linear dependency with negative slope is in line with the prediction of the thermal-activation model [cf. Eq. (4.6)]. The deviations for high T_s are a consequence of the particular grain size distribution of the film, which will be discussed in depth in Sec. 4.3. The relaxation time constants τ_1 and τ_2 decrease with increasing T_s and tend to zero for $T_s > 280\,\text{K}$ as shown in Fig. 4.7 (b). Note that the thermal-activation model states that the decay rate solely depends on the sample temperature T_s [cf. Sec. 2.3.1].

A logarithmic plot of R_e and $|\Delta R_a|$ as function of the current density

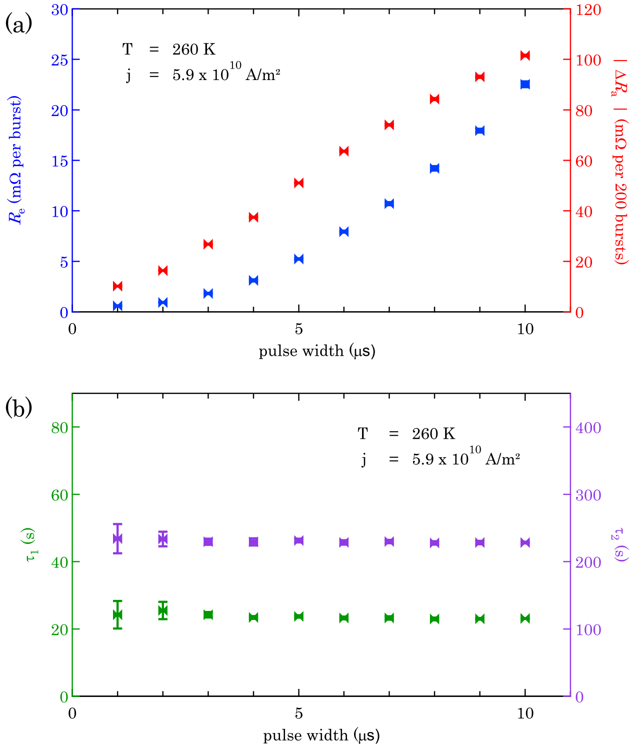

Figure 4.9: Plot of (a) R_e and $|\Delta R_\mathrm{a}|$ and (b) $\tau_{1,2}$ in dependence of the pulse width Δt with fixed $T_\mathrm{s} = 260\,\mathrm{K}$ and $j = 5.9 \times 10^{10}\,\mathrm{A/m^2}$. The dependence of R_e and $|\Delta R_\mathrm{a}|$ on Δt is implicitly captured by the thermal-activation model since Joule heating is enhanced for longer pulses. Thus, the shown trend matches the expectation. $\tau_{1,2}$ is independent of Δt.

is shown in Fig. 4.8 (a) with a linear fit applied to $\log_{10}[R_\mathrm{e}]$. Again, the prediction made with Eq. (4.6), i.e. $R_\mathrm{e} \propto \exp(j)$, is verified. $|\Delta R_\mathrm{a}|$ grows sub-exponentially due to a saturation of the switching. The decay times τ_1 and τ_2 are independent of j [cf. Fig. 4.8 (b)].

In Fig. 4.9 (a) the dependence of R_e and $|\Delta R_\mathrm{a}|$ on Δt is shown. As argued above, this increase is expected due to the increased Joule heating facilitated by longer pulses. τ_1 and τ_2 are independent of Δt as well [cf. Fig. 4.9 (b)]. The decay constants obtained for $T_\mathrm{s} = 260\,\mathrm{K}$ are

$$\tau_1 \approx 24\,\mathrm{s} \qquad \text{and} \qquad \tau_2 \approx 234\,\mathrm{s}. \tag{4.7}$$

4.3 Discussion of the thermally assisted switching in CuMnAs

All predictions that conclude from the thermal-activation model are verified by the experimental results presented in Sec. 4.2.2. From the fits applied to switching efficiency dependencies, however, no microscopic parameters of the CuMnAs film like the anisotropy energy density $K_{4\|}$ can be extracted. Actually, the only quantity which can be evaluated without numerically expensive simulations, which will be discussed in Sec. 4.4, is the switching energy barrier E_B. This can be done by rearranging Eq. (2.51) to

$$E_\mathrm{B}^i = \ln\left(f_0 \tau_i\right)\, k_B T_\mathrm{s} \tag{4.8}$$

considering that the system can be characterized by three grain sizes $V_\mathrm{g}^{0,1,2}$. $E_\mathrm{B} = K_{4\|}\, V_\mathrm{g}$ depends on the grain size distribution of the system, which is identical for all shown experiments. The measured decay constants (4.7) at $T_\mathrm{s} = 260\,\mathrm{K}$ then relate to

$$E_\mathrm{B}^1 \approx 691\,\mathrm{meV} \qquad \text{and} \qquad E_\mathrm{B}^2 \approx 743\,\mathrm{meV}. \tag{4.9}$$

The index $i = 0$ accounts for the nonrelaxing grains with $E_\mathrm{B}^0 > E_\mathrm{B}^2$. For the T_s variation one finds temperature dependent $\tau_{1,2}$ and temperature dependent $E_\mathrm{B}^{1,2}$ which are shown in Fig. 4.10 (a). Here, a linear fit $E_\mathrm{B} = \Delta_T k_B T_\mathrm{s}$ allowing no offset yields the so-called thermal stability factor

$$\Delta_T = \frac{E_\mathrm{B}}{k_B T_\mathrm{s}} \tag{4.10}$$

which characterizes the switched grain ensemble. This calculates to

$$\Delta_T^1 \approx 31.1 \qquad \text{and} \qquad \Delta_T^2 \approx 33.4. \tag{4.11}$$

Using the thermal stability factor the grain ensembles are categorized into three segments, namely *unblocked* for $\Delta_T \lesssim 27$ ($\tau \lesssim 0.5\,\mathrm{s}$), *switchable* for $27 \lesssim \Delta_T \lesssim 44$, and *blocked* if $\Delta_T \gtrsim 44$ ($\tau \gtrsim 10^7\,\mathrm{s} \approx 0.3\,\mathrm{yr}$). This classification follows the rationale of metallic polycrystalline exchange bias systems [79]. In a film with grains that follow a grain size distribution, e.g. a Gaussian one, these categories represent different segments of grain sizes, as depicted in Fig. 4.10 (b). In unblocked grains $\boldsymbol{L}$ changes its state fast compared to our measurement timing and, thus, their contribution to the signal averages to zero. The switchable grains can be manipulated by the current pulses but are not stable at given T_s. Hence, the signal generated by these grains decays within tens of minutes. Blocked grains do not change their

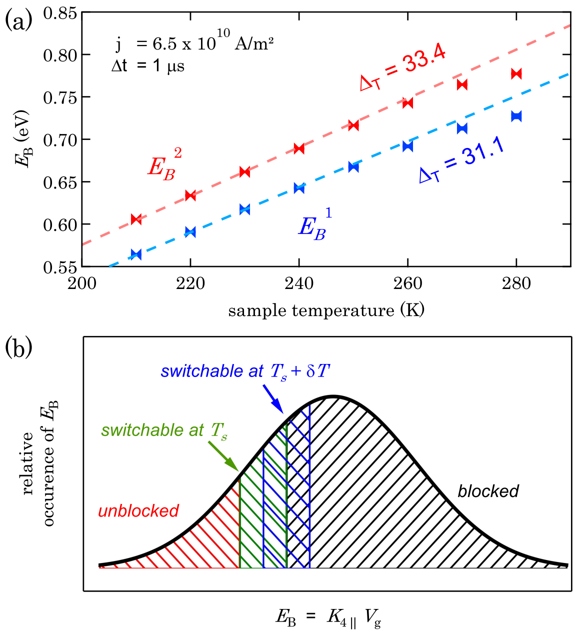

Figure 4.10: (a) $E_\mathrm{B}^{1,2}$ calculated from $\tau_{1,2}$ using Eq. (4.8). The dashed lines are linear fits with no offset considering $T_\mathrm{s} \leq 240\,\mathrm{K}$. (b) Gaussian $E_\mathrm{B} = K_{4\|}V_\mathrm{g}$ distribution. The hatched areas indicate parts of the ensemble that are *unblocked* (red), *switchable* (green/blue), or *blocked* (black).

state during the given time scales and are considered stable, even with current applied if Joule heating is neglected. In reality, however, Joule heating results in a temperature increase δT during a pulse allowing for the switching of a set of initially blocked grains, represented by the blue hatched area in Fig. 4.10 (b). After the pulse, the temperature returns back to T_s whereupon the relaxation rate is enhanced during the first couple of µs of the cool-down [cf. Fig. 2.14 (b)]. The measurement of R_PHE is delayed by 2 s after the burst. Thus, grains which have been switched and did not relax back to equilibrium during this delay are measured. This is effectively the case for $\tau \gtrsim 0.5\,\mathrm{s}$ during the pulse. The increased temperature $T_\mathrm{s} + \delta T$ during the pulse shifts the subset of switchable grains to larger grain sizes. Thereby, larger grains become switchable, while small grains become unblocked during a pulse and occupy the four Néel-vector orientations uniformly. When the switchable subset during the pulse shifts through a maximum of the grain size distribution as a function of temperature a maximum in $|\Delta R_\mathrm{a}|$ is observed, while the efficiency R_e further increases [cf. Fig. 4.7 (a)]. This reasoning for the local maximum of $|\Delta R_\mathrm{a}|$ in a T_s sweep applies to any distribution that has a well-defined maximum occurrence of $E_\mathrm{B}^\text{max-o} = K_{4\|}\, V_\mathrm{g}^\text{max-o}$.

The estimated thermal stability factors of the fast and slow relaxation component (4.11) are independent of T_s. At lower temperature, the switchable subset of grains shifts to smaller grain volumes, such that $E_\mathrm{B} = k_\mathrm{B} T \Delta_T$ is in agreement with the categorization of switchable grains. Consequently, it is expected that at lower temperature only grains with smaller energy barrier are switchable. The temperature increase during a pulse and the accompanied relaxation enhancement acts on a shorter time scale than the measurement can resolve. Formerly blocked grains that became switchable during the pulse and did not relax within the 2 s delay are blocked again and, therefore, do not affect the relaxation time constants $\tau_{1,2}$. Hence, the observable resistance decay is determined by T_s only. This is in line with the theoretical result that the NSOT should be temperature independent [21].

Up to now, the Arrhenius plot in the inset of Fig. 4.7 (a) has only been used to validate the proportionality $R_\mathrm{e} \propto -T_\mathrm{s}^{-1}$. However, e.g. in chemistry such a plot is routinely used to find the activation energy E_A of a chemical reaction. It is calculated from the slope $|m|$ via

$$E_\mathrm{A} = k_\mathrm{B}|m| = (195 \pm 8)\ \mathrm{meV} \tag{4.12}$$

with $|m|$ being obtained from the Arrhenius plot. The error is the standard deviation of the fit times k_B. Following Eq. (4.5) one can identify

$$E_\mathrm{A} = E_\mathrm{B} - \frac{x L \chi V_\mathrm{g} j_\mathrm{CR}}{V_\mathrm{c}}. \tag{4.13}$$

Note that the center-current density $j_\mathrm{CR} = 0.6\, j$ is used for this quantitative analysis [cf. Chap. 3]. The Arrhenius plot evaluates E_A with respect to T_s although the switching happens with a time dependent temperature $T_\mathrm{s} < T < T_\mathrm{s} + \delta T$ and, hence, E_A is underestimated.

With known j_CR, $x = 1/\sqrt{2}$ for orthogonal switching, literature values $\chi = 3\,\mathrm{mT}/(10^{11}\,\mathrm{A/m^2})$ [22] and $|\boldsymbol{L}| = 7\mu_\mathrm{B}$ [54], structural information $V_\mathrm{cell} = 6.318\,\text{Å} \cdot \left(3.820\,\text{Å}\right)^2$ and E_B obtained from relaxation measurements, one finds that V_g is the only unknown parameter. This conclusion holds true if only grains with one distinct grain size are excited by the NSOT. But, as it was argued above, within a temperature sweep one always excites grains with matching thermal stability factor Δ_T and, thus, different parts of the grain ensemble.

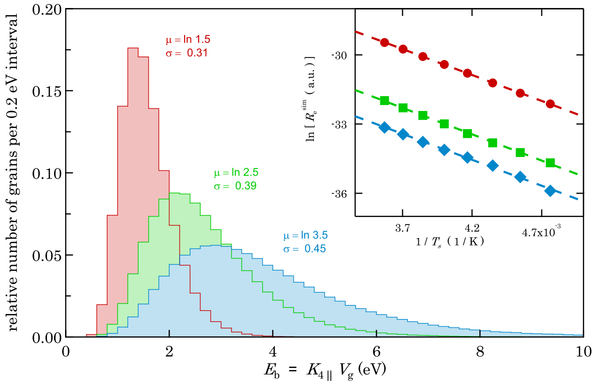

FIGURE 4.11: Histograms for ensembles of 10^6 grains each where $E_\mathrm{B} = K_{4\|}V_\mathrm{g}$ is lognormal distributed. The inset shows the Arrhenius plot for each distribution in the respective color.

In the following the consequences of this statement are illustrated in an example. Fig. 4.11 shows histograms of three ensembles with 10^6 grains each, where the distribution of $E_\mathrm{B} = K_{4\|}V_\mathrm{g}$ is lognormal, i.e. $\mathcal{LN}(\mu, \sigma)$. μ is the mean value and σ the standard deviation of the distribution. From a known distribution one can calculate the switching efficiency

$$R_\mathrm{e}^\mathrm{sim} \propto \sum_{i=1}^{10^6} \Bigg(l_\mathrm{g}^i \exp\left[\left(\xi\, V_\mathrm{g}^i - \frac{K_{4\|}}{k_\mathrm{B}}\, V_\mathrm{g}^i\right)\frac{1}{T_\mathrm{s}}\right] \cdot \\ \exp\left[-2\,\mathrm{s}\cdot f_0 \exp\left(-\frac{K_{4\|}\, V_\mathrm{g}^i}{k_\mathrm{B} T_\mathrm{s}}\right)\right]\Bigg) \qquad (4.14)$$

with $\xi = xL\chi j_\mathrm{CR}/(k_\mathrm{B}V_\mathrm{c})$ following Eq. (2.63). $K_{4\|}V_\mathrm{cell} = 1.2\,\mu\mathrm{eV}$ ($K_{4\|} \approx 2.1\,\mathrm{kJ/m^3}$) is taken from the kMC simulation results that will be discussed in Sec. 4.4. The second exponential function accounts for the relaxation during the delay of 2 s in the experiment [cf. Eq. (2.51)]. Each summand contributes to the measured transverse voltage in proportion to the edge length $l_\mathrm{g} \approx \sqrt[3]{V_\mathrm{g}}$ of the respective grain. The Arrhenius plot of $R_\mathrm{e}^\mathrm{sim}$ is shown in the inset of Fig. 4.11 for three different grain size distributions. It turns out, that $\mathcal{LN}_1(\ln 0.8, 0.16)$, $\mathcal{LN}_2(\ln 1.0, 0.23)$, and $\mathcal{LN}_3(\ln 1.2, 0.27)$ are represented by similar $E_\mathrm{A} = \{198 \pm 8,\ 189 \pm 4,\ 192 \pm 2\}$ meV, although their shapes are diverse. Hence, E_A does not allow to draw conclusions about the underlying grain size distribution and, thus, the Arrhenius plot evaluation only yields an effective quantity. As consequence one has to conclude, that the grain size of the nonrelaxing grains V_0 is not accessible by the shown experiment.

4.4 Kinetic Monte-Carlo model

The experimental findings provide substantial evidence that the thermal-activation model for the NSOT switching is valid for this sputter-deposited CuMnAs film. However, the shown analysis only yields the product of anisotropy energy density $K_{4\|}$ and grain size (distribution) V_g as result regarding microscopic parameters. Thus, a full kMC simulation is set up to simulate the switching and relaxation alike to extract $K_{4\|}$ and V_g individually [2, 4]. The simulation applies the NSOT theory to calculate a PES for the system with and without current [cf. Fig. 2.14 (a)]. Then, the thermal-activation model is used to calculate the respective switching probability P_sw with Eq. (2.59). This is done for a large number, e.g. 200 000, of individual grains and for each of them P_sw is compared to a random number $0 < r < 1$. If $P_\mathrm{sw} > r$, the grain switches its state.

The simulations result is shown as a comparison to the respective experimental data in Fig. 4.12. The relevant inputs used in the simulations are listed in Tab. 4.1.

Most parameters entering the simulation are accessible either from theo-

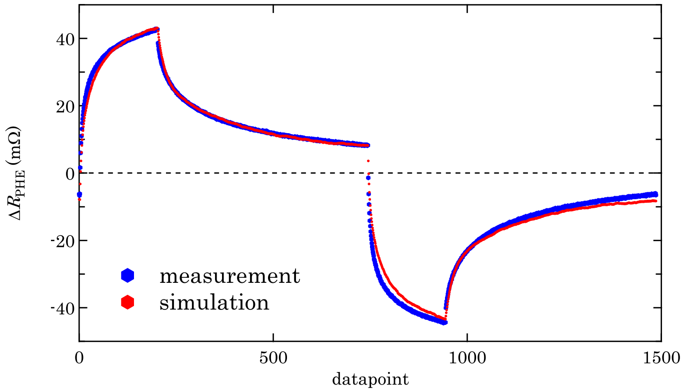

Figure 4.12: Comparison of a kMC simulation using the parameters listed in Tab. 4.1 and the first switching cycle of the measurement shown in Fig. 4.4 (b).

retical calculations or the presented analysis scheme for the switching curves. The remaining free parameters are the anisotropy energy density $K_{4\|}$, the effect amplitude A which in the case of one grain size would be equal to the AMR amplitude A_{AMR}, and the underlying grain size distribution. As demonstrated by Fig. 4.11 it is not possible to determine the grain size distribution from the experiments. However, it is possible to model the decay of a set state by the sum of three terms, cf. Eq. (4.2), each representing an energy barrier E_{B}. This leads to three energy barriers $E_{\mathrm{B}}^{0,1,2}$ that can be used to characterize the grain size distribution. E_{B}^{0} accounts for the nonre-

Parameter	Value	Source
aniso. energy density	$K_{4\|} = 1.2\,\mu\mathrm{eV}/V_{\mathrm{cell}}$	free
effect amplitude	$A = 71.5\,\mathrm{m}\Omega$	free
grain size population	$V_{\mathrm{g}}^{0,1,2} = \{0.42, 0.35, 0.23\}$	free
energy barriers	$E_{\mathrm{B}}^{1,2} = \{691, 743\}$ meV	measurement
energy barrier	$E_{\mathrm{B}}^{0} = 2E_{\mathrm{B}}^{2} - E_{\mathrm{B}}^{1} = 795\,\mathrm{meV}$	estimation
electrical resistivity	$\rho = 430\,\mu\Omega\,\mathrm{cm}$	measurement
CuMnAs thickness	$h = 68\,\mathrm{nm}$	measurement
CR current density	$j_{\mathrm{CR}} = 3.54 \times 10^{10}\,\mathrm{A/m^2}$	FEM simul.
sample temperature	$T_{\mathrm{s}} = 260\,\mathrm{K}$	exp. parameter
pulse width	$\Delta t = 5\,\mu\mathrm{s}$	exp. parameter
relaxation time	$T_{\mathrm{relax}} = 600\,\mathrm{s}$	exp. parameter
unit cell volume	$V_{\mathrm{cell}} = 92.2\,\mathrm{Å}^3$	Ref. [76]
spin-torque efficiency	$\chi = 3\,\mathrm{mT}/(10^{11}\,\mathrm{A/m^2})$	Ref. [22]
Néel-vector magn.	$\|\boldsymbol{L}\| = 7\mu_B$	Ref. [54]

Table 4.1: Summary of parameters used for the kMC simulation shown in Fig. 4.12. Free parameters are adjusted iteratively to reach good agreement with the experiment. Experimental parameters are set conditions at which the experiment is conducted. Literature values are taken from the respective references. The other parameters are extracted from the switching experiment, estimated or originate from a simulation. CR stands for center-region.

laxing grains and, thus, cannot be determined by relaxation measurements. To limit the number of free parameters $E_\mathrm{B}^0 = 2E_\mathrm{B}^2 - E_\mathrm{B}^1 = 795\,\mathrm{meV}$ is chosen as fixed parameter in the simulation. The rational behind this decision is to have a set of energetically equidistant grains [$\Delta E = 52\,\mathrm{meV}$]. With a biaxial anisotropy energy density of $K_{4\|} = 1.2\,\mu\mathrm{eV/(unit\ cell)} \approx 2.1\,\mathrm{kJ/m^3}$ a good match between simulation and experiment is achieved. The corresponding grain volumes are of the order $V_\mathrm{g} \approx (37\ldots39\,\mathrm{nm})^3$. From XRD and TEM investigations we know that the sample has an oop grain size of $L_c \approx 10\,\mathrm{nm}$ [cf. Sec. 4.1]. This, in turn, leads to a lateral grain diameter of $\approx 2.3\,\mathrm{nm}$ assuming cylindrical grains. These numbers are an approximation and might not represent the true granularity of the system. However, the scale of this outcome fits in the overall picture.

4.5 Summary on CuMnAs switching

In the first part of this thesis the NSOT switching mechanism was investigated in CuMnAs thin film samples that were grown by dc-magnetron sputtering. The deposition process was studied and a procedure that allows to reliably grow CuMnAs thin films that crystallize in the tetragonal phase has been found. The deposition at high temperatures of $T_\mathrm{d} = 410°\mathrm{C}$ compels a rough surface with $R_\mathrm{RMS} = 4.8\,\mathrm{nm}$ if the sputtering is done with a dc power supply. A Bachelor's thesis that was done in collaboration to this dissertation found that an rf plasma greatly decrees the surface roughness while keeping the crystalline quality [80]. However, up to now no switching experiments have been conducted at those smooth rf films.

The NSOT switching was observed in the sputtered films and the experimental parameters sample temperature T_s, pulse current density j, and pulse width Δt have been varied. To analyze the switching characteristics in dependence of those parameters an evaluation scheme has been developed and applied to the data. The findings were discussed using a macroscopic thermal-activation model which acts as an extension to the NSOT theory. The good agreement between experiments on CuMnAs and predictions that follow the thermal-activation model provides strong evidence that the developed description marks a valuable advancement in understanding the physics of NSOT switching.

The switching and relaxation can be reproduced by a kMC simulation with striking agreement to experimental data. With the shown evaluation scheme and theoretical calculations from other sources the proposed model achieves quantitative agreement with only three free parameters left. The biaxial anisotropy energy density $K_{4\|}$ is one of those free parameters. By optimizing the agreement between simulation and experiment the value

$K_{4\parallel} = 1.2\,\mu\mathrm{eV}/V_{\mathrm{cell}}$ ($K_{4\parallel} \approx 2.1\,\mathrm{kJ/m^3}$) has been found.

One can summarize that the NSOT is a relatively small torque that cannot facilitate a deterministic switching of the Néel order using moderate current densities. The observed switching is a thermally assisted process and, as consequence, the set state is to a large degree thermally unstable. Despite the thermally activated nature of the switching it is observable at multiple temperatures. This is reasoned by the granularity of the film which results in various switching energy barriers. At each temperature, a different subset of grains participates in the switching process. The active grains are characterized by a thermal stability factor $27 \lesssim \Delta_T \lesssim 44$.

Resistive-nonmagnetic contribution in switching experiments

5

In Chap. 4 the current densities used to reorient the Néel vector in a CuMnAs thin film are $5.3 \times 10^{10}\,\mathrm{A/m^2} < j < 7.1 \times 10^{10}\,\mathrm{A/m^2}$. As comparison, a commercially available NYM-J cable with three braids used in private households has a braid cross section of $A_{\mathrm{hh}} = 1.5\,\mathrm{mm}^2$. According to DIN VDE 0298-4 each braid has a legal current resilience of $I_{\mathrm{hh}} = 15\,\mathrm{A}$ if installed into a ductwork [81]. This concludes to a legal current density for households of

$$j_{\mathrm{hh}} = \frac{I_{\mathrm{hh}}}{A_{\mathrm{hh}}} = 10^7\,\mathrm{A/m^2} \tag{5.1}$$

which is more than three orders of magnitude smaller than the current density used in the CuMnAs switching experiment. Regarding the relatively high current densities necessary to observe NSOT switching it is mandatory to consider changes of the film due to the electrical stress.

Hence, this chapter covers the influence of high current densities on nonmagnetic thin film *Union Jack* devices to reveal possible artifacts in NSOT switching experiments. For this investigation different materials have been tested as model systems, namely Mo, Nb, Ta, Ti, and V. It was desired to find a metal that can be grown in different degrees of crystalline quality by adjusting the deposition temperature. Although all candidates yielded similar results that lead to the same conclusion, Nb was outstanding regarding durability and reproducibility. Investigations that go beyond a proof of concept transport experiment are, therefore, only conducted in Nb films and those results are shown in the following.

First, Nb thin films of different crystalline quality are prepared. The deposition procedure and basic characterization results are covered in Sec. 5.1. Then, different mechanisms that may alter the thin film properties are introduced in Sec. 5.2 followed by experiments used to test for the proposed mechanisms in Sec. 5.3. Finally, FEM simulations are conducted to construct a consistent model that can explain how changes of the thin films properties result in a nonmagnetic contribution that resembles the PHE. They are presented in Sec. 5.4.

5.1 Nb sample preparation and characterization

Stacks of Nb thin films of the type MgO (001) / Nb 25 nm / Si 2 nm are grown by dc-magnetron sputtering [cf. Sec. 3.1.1]. The Nb film is deposited at different temperatures T_d to obtain samples with varying properties. One sample is grown at RT while the HT sample is grown at $T_\mathrm{d} = 400\,°\mathrm{C}$. XRD measurements, presented in Fig. 5.1, show that the crystallographic properties of the films depend on T_d. The RT sample shows no preferred growth direction, whereas the HT sample grows in (110) direction. Using Scherrer's formula (3.2) one finds that the oop crystallite size L_c is in the order of the film thickness for both samples. This difference in XRD intensity indicates that the grains in the RT sample grow broadly oriented and, thus, only a fraction of grains can contribute to the diffraction peaks. In the HT sample, on the other hand, most crystals align themselves according to the substrates crystallography which leads to a high XRD intensity. The resistivities are $\rho_\mathrm{RT} = 27.4\,\mu\Omega\,\mathrm{cm}$ and $\rho_\mathrm{HT} = 23.5\,\mu\Omega\,\mathrm{cm}$, determined by four-point measurements. $\rho_\mathrm{HT} < \rho_\mathrm{RT}$ is due to reduced electron scat-

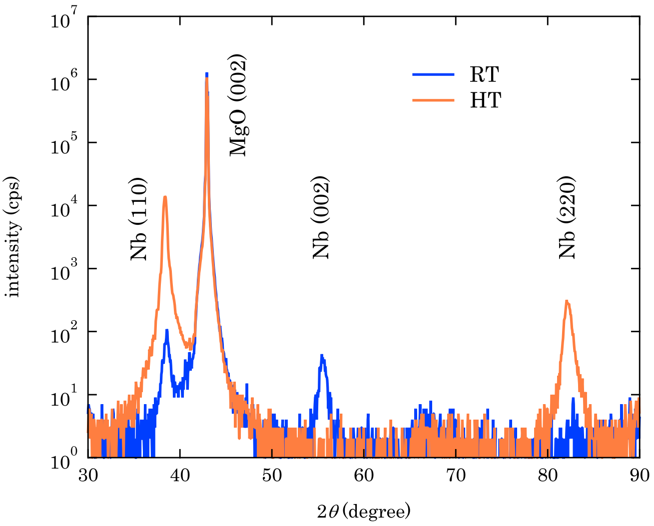

Figure 5.1: XRD measurements of Si capped Nb films with film thicknesses $h_\mathrm{Nb} = 25\,\mathrm{nm}$ grown at various deposition temperatures T_d, i.e. room temperature (RT) and high temperature (HT). The integral width of the (110) peak reads $\beta_\mathrm{HT} = 0.47°$ and $\beta_\mathrm{RT} = 0.55°$ which translates to $L_c^\mathrm{HT,RT} = \{24.6, 20.5\}\,\mathrm{nm}$.

tering at grain boundaries, directly linking the resistivity to the crystallite size. From the deposition characteristics one can conclude that the growth of Nb crystals in (110) direction on MgO (001) substrates is favored in a high-temperature deposition process.

To repeat the experiments done at CuMnAs the films are patterned into *Union Jack* devices using UVL [cf. Fig. 3.4 (b)] and wire-bonded into C-DIPs. On each sample, half of the devices have their pulse lines aligned parallel to the substrates edge, the other half of the devices are rotated by $45°$.

5.2 Consequences of high current densities

In the following two mechanisms will be discussed regarding the expected effects of high currents passing through the the *Union Jack* devices pulse lines.

5.2.1 Annealing

You's formula (2.50) has already been introduced in Sec. 2.3. It describes the temperature rise δT facilitated by a current density that flows through a

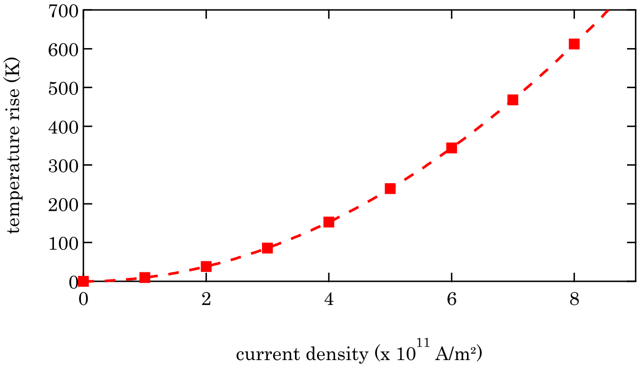

FIGURE 5.2: Maximum temperature rise of the Nb film during a $\Delta t = 10\,\mu s$ pulse of different current density j evaluated with You's formula (2.50). The used parameters are $\kappa_{\mathrm{MgO}} = 40\,\mathrm{W/(m\,K)}$, $\mu_{\mathrm{MgO}} = 12\,\mathrm{mm^2/s}$, $\alpha = 0.5$, $w = 8\,\mu\mathrm{m}$, $h = 25\,\mathrm{nm}$, and $\sigma = (25\,\mu\Omega\,\mathrm{cm})^{-1}$. The dashed line visualizes $\delta T \propto j^2$ by a quadratic fit.

thin current channel. Hence, the maximum film temperature

$$T_{\max} = T_{\mathrm{s}} + \delta T(j, \Delta t) \tag{5.2}$$

can be calculated in dependence of current density j and pulse width Δt. In this chapter the sample temperature T_{s} is always room temperature. As seen in Fig. 5.2, one has to apply high j to obtain a δT that is comparable to CuMnAs which is primarily due to the lower resistivity and film thickness of the Nb samples [cf. Fig. 2.14 (b)]. Anyway, for $\Delta t = 10\,\mu\mathrm{s}$ and $j = 6 \times 10^{11}\,\mathrm{A/m^2}$ one obtains a temperature rise of $344\,\mathrm{K} \approx \delta T_{\mathrm{CuMnAs}}$. From knowledge gained from the deposition process one could expect that the RT sample would experience significant thermal annealing if exposed to such a current density for a longer period of time. The annealing would then reduce the resistivity in areas of high current density, i.e. in the constrictions of the *Union Jack* device.

An elevated temperature may also induce a structural transformation of the material into an unstable phase of different resistivity. However, a metastable phase transition in Nb should only appear above 2800 K [82]. Hence, the annealing process is regarded as irreversible with no effect being expected during the observation of the relaxation. Note that this might be different in other systems.

5.2.2 Electromigration

The effect of high current densities in thin film devices has been investigated extensively decades ago in the course of microelectronics [83–86]. It has been found that the predominant reason for the failure of microstructures under electrical stress is electromigration. In the presented experiment electromigration would manifest in a transport of material away from areas of high current density, i.e. the constrictions, thereby creating voids in the material and increasing the local resistivity.

Electromigration as well as annealing are thermally activated and depend on individual energy barriers Q and the temperature T via a Boltzmann factor [87]. In particular, according to Black's equation [88]

$$\mathrm{MTF} = \frac{A}{j^2} \exp\left(\frac{Q}{k_{\mathrm{B}}T}\right) \tag{5.3}$$

the mean-time-to-failure (MTF) is a strong function of current density and temperature, where the film temperature itself depends strongly on the current density. Here, k_{B} is the Boltzmann constant and A is a scaling factor. As shown above, the film temperature may rise by several hundred Kelvin within a pulse [cf. Figs. 2.14 (b) & 5.2]. In Fig. 5.3, Black's equation

(5.3) is evaluated within two models: one calculated at fixed temperature $T = 300\,\mathrm{K}$, and one calculated at an elevated temperature $T + \mathrm{avg}\,(\delta T)$ with $\mathrm{avg}\,(\delta T)$ being the pulse-averaged temperature for a pulse width of $\Delta t = 10\,\mu\mathrm{s}$. The parameters for Black's equation are chosen as $Q = 0.6\,\mathrm{eV}$ and $A = 2 \times 10^{17}\,\mathrm{sA^2/m^4}$. While Q is a typical value for grain-boundary self-diffusion [88], A is chosen to roughly match the experimental destruction threshold of the device determined in Sec. 5.3. Considering $j > 10^{11}\,\mathrm{A/m^2}$ one clearly sees that the Joule heating is largely responsible for a short MTF. In the high-current density regime, Black's equation (5.3) is often rewritten as

$$\mathrm{MTF} = \frac{A}{j^m} \exp\left(\frac{Q}{k_\mathrm{B} T}\right) \tag{5.4}$$

with $m > 2$ to effectively take the Joule heating into account. The numerical estimate done via You's formula (2.50) suggest that $m \approx 13$ in this specific example, i.e. the MTF shows a very rapid decay with increasing j.

Electromigration is a long-range movement of atoms and fundamentally different to, e.g. the dislocation of atoms within a unit cell. During the relaxation, a negligible current is flowing through the structure and, thus,

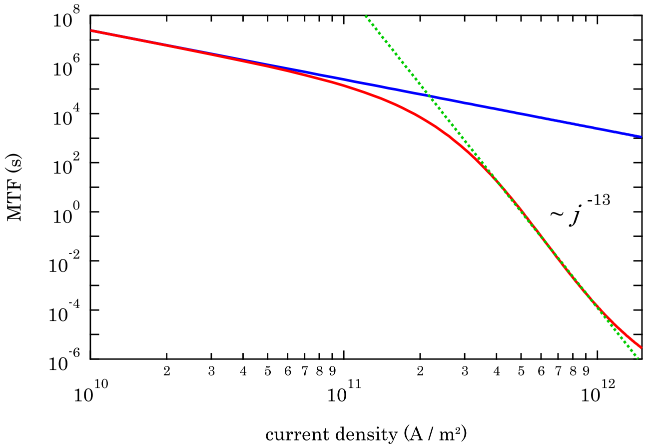

FIGURE 5.3: MTF as a function of the current density. Two models are considered: The blue curve considers a fixed temperature of 300 K, and the red curve includes Joule heating δT as pulse-averaged temperature $\mathrm{avg}\,(\delta T)$. The dotted line represents a power-law fit to the high-current density regime.

there is no driving force for electromigration. It is therefore expected that no electromigration related effect is observable during the relaxation of the system.

5.3 Experimental investigation

The experimental procedure regarding the transport experiment is similar to the CuMnAs switching experiment and described comprehensively in Chap. 3. Here, however, the sample is not placed in a cryostat and the probe-current readout is not done with a second Lock-In amplifier but with a Keithley multimeter directly [cf. Fig. 3.5]. Transport experiments are performed either with simultaneous microdiffraction (µXRD) measurements or SEM imaging.

5.3.1 Pulsing experiments with Nb thin films

A pulsing experiment performed with Nb thin films is presented in Fig. 5.4. Panel (a) shows the change of $R_\perp$ for the RT sample with a current density of $j = 7.5 \times 10^{11}\,\mathrm{A/m^2}$ applied alternating to the x and y pulse line. The respective relaxation is observed for $T_\mathrm{relax} = 60\,\mathrm{s}$. A significant change of $R_\perp$ during pulsing is observed, whereas $R_\perp$ remains stable during the relaxation. Initially, pulsing along x increases $R_\perp$ while pulsing along y decreases $R_\perp$. The amplitude of the switching decreases with each repeat and vanishes around the fifth repeat. The following repeats show an inverted sign of the response with virtually constant amplitude. An overall trend towards higher values of $R_\perp$ is present which is most likely related to asymmetries of the pulse lines due to imperfect lithography. It is not shown explicitly but note that the polarity of the pulse current has no impact on the signal. Fig. 5.4 (b) shows an equivalent measurement for the HT sample. However, a higher current density of $j = 11.0 \times 10^{11}\,\mathrm{A/m^2}$ had to be applied to observe a transverse electrical response of similar magnitude. The HT sample only shows one sign of transverse resistance change $\Delta R_\perp$ that is independent of the applied current density. The degradation of the $\Delta R_\perp$ amplitude slows down for successive repeats. There is no qualitative difference in behavior between devices with aligned with the edge of the substrate or rotated.

This experiment shows that one can observe a transverse response to electrical pulses in a nonmagnetic film. The striking difference to the NSOT switching in CuMnAs, discussed in Chap. 4, is that the current induced response of the Nb is stable in time. The processes introduced in Sec. 5.2 share this property. The following passages focus on the experimental validation of either process without verification that a lateral variation in resistivity can induce a transverse response in a PHE measurement geometry. The exact mechanism how any of these processes can introduce a perpendicular resistance change will be clarified later in Sec. 5.4.

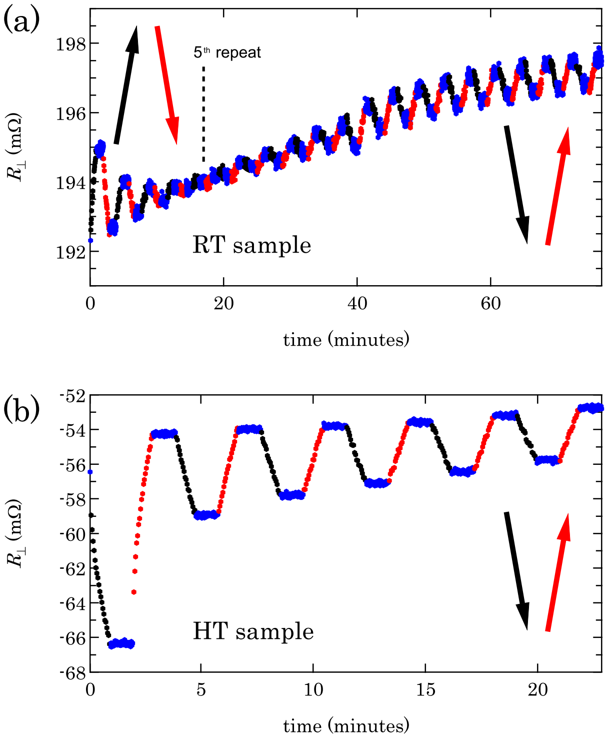

FIGURE 5.4: (a) Pulses with $j = 7.5 \times 10^{11}\,\mathrm{A/m^2}$ and $\Delta t = 10\,\mu\mathrm{s}$ are applied to a device on the RT sample with $x \parallel$ MgO[100]. The colors of the data points match the arrows in Fig. 3.4 to identify the pulsing and the relaxation phase. The arrows here accentuate the sign of $dR_\perp/dt$ that correlates with a certain pulsing direction. In (a), this sign inverts after the fifth repeat. (b) A similar measurement performed at the HT sample with $j = 11.0 \times 10^{11}\,\mathrm{A/m^2}$ and $\Delta t = 2\,\mu\mathrm{s}$. The offset to $R_\perp$ in (a) and (b) arises from imperfect lithography, i.e. the transverse voltage pick-up lines are not perfectly in line.

5.3.2 Pulsing experiments at Nb with simultaneous microdiffraction measurements

The annealing mechanism proposed in Sec. 5.2.1 suggests that Joule heating induced by the applied current density leads to a crystallization in the constrictions of the *Union Jack* device. This should be observable in the RT sample but not in the HT sample since it is of good crystallinity already. The structural properties of a crystalline sample are typically investigated by XRD. Here, the pulsing experiment is combined with µXRD measure-

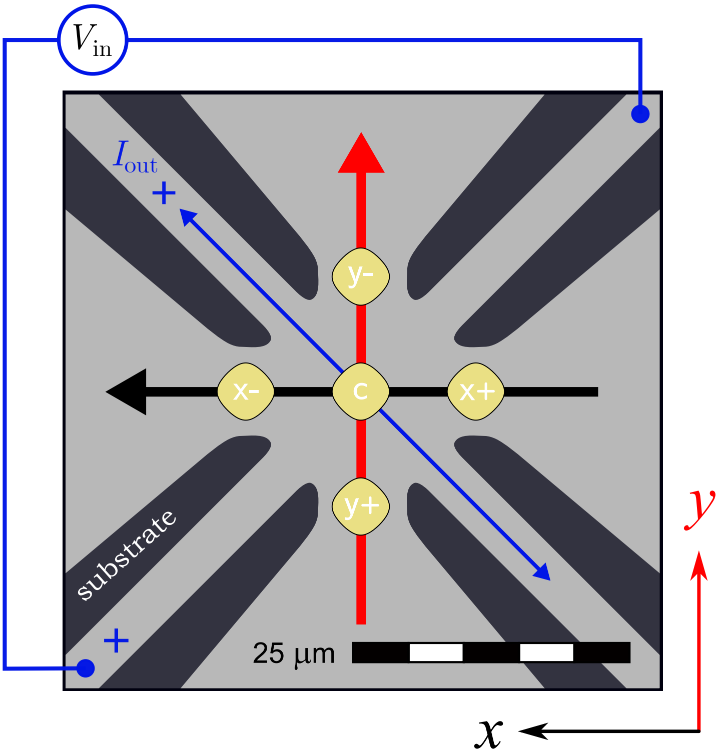

Figure 5.5: Schematic of the UVL *Union Jack* device. The arrows describe the electrical contacting and are analog to Fig. 3.4. Pulse and probe line have a width of 8 µm and 4 µm, respectively. Yellow areas show the positions of the x-ray spot for µXRD measurements and the nomenclature for the positions. The contour corresponds to 50% beam intensity.

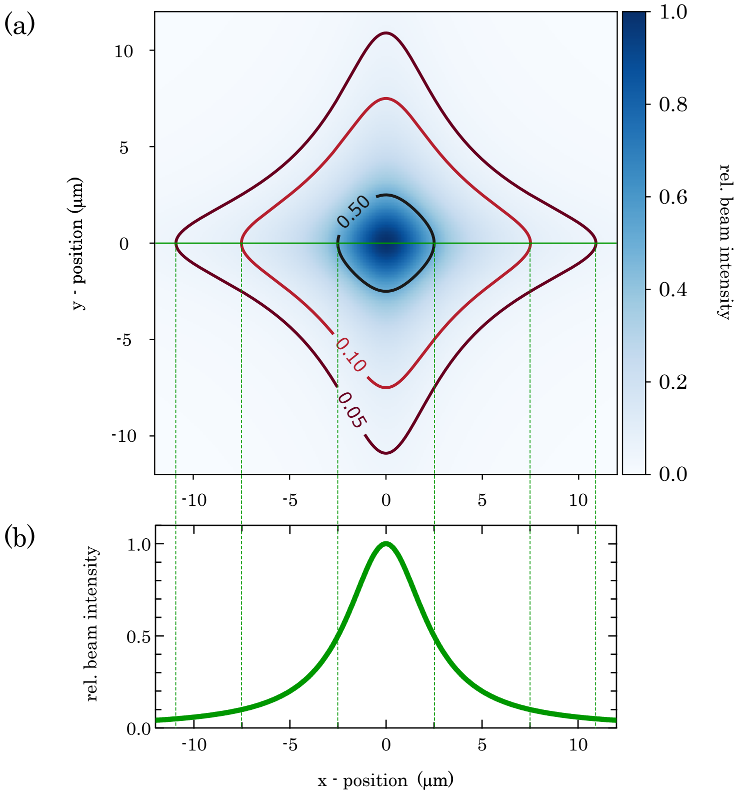

Figure 5.6: Lorentzian intensity profile of the x-ray spot used for the µXRD measurements. (a) 2D colorplot of the spot with contours for various relative intensities. The beam expands in x and y direction due to the apertures used to reduce the spot size. (b) Intersection of the 2D intensity profile along the x-axis highlighting the long tails associated with a Lorentzian.

ments to investigate the crystallinity of the film in the constrictions and find a correlation to the electrical pulsing, i.e. a current induced annealing.

The µXRD investigation is conducted at the Advanced Light Source (ALS), beamline 12.3.2, Berkeley, California, USA [89]. µXRD uses a synchrotron as radiation source where white x-rays are generated by the deflection of an electron beam with superconducting bending magnets. This white beam has a high brightness and the spot can be downsized to a couple of µm, which allows to investigate laterally varying crystallographic properties. Optionally, the white beam can be guided through a monochromator allowing to select a specific photon energy $h\nu$. The x-ray spot has a fixed position, and the sample can be moved by a $xyz - \theta - \phi$ stage with submicron positioning accuracy. To calibrate the position of the x-ray spot, the sample is moved while measuring the x-ray fluorescence which allows to map the presence of Nb and, thus, find the device. Diffraction patterns are detected by a PILATUS 1M detector, consisting of ten two-dimensional x-ray sensitive charge-coupled device (CCD) arrays, using an integration time of $10 - 30\,\mathrm{s}$.

An experiment that combines electrical current pulses and µXRD operates as follows. A pulse-relaxation sequence of $n = 100$ bursts of pulses with pulse width $\Delta t = 10\,\mu\mathrm{s}$ is sent through either the x or the y pulse line of the device with $R_\perp$ measurements after each burst. During the following relaxation time $T_{\mathrm{relax}} = 60\,\mathrm{s}$ diffraction patterns are measured subsequently for the beam being positioned in each of the constrictions $\{x\pm, y\pm\}$ and the center C of the device, as indicated in Fig. 5.5. The positions at which the µXRD measurements are taken always follow the same order, i.e. $\{\mathrm{C}, x-, y-, x+, y+\}$. This procedure is then repeated for the other pulse line. The current density j is gradually increased to maintain a $R_\perp$ change of significant amplitude after each pulse-µXRD succession. The yellow spots sketched in Fig. 5.5 mark the contour at which the beam intensity drops to 50% which corresponds to a full-width-at-half-maximum (FWHM) of 5 µm. However, the beam profile follows a Lorentzian intensity distribution as illustrated in Fig. 5.6. Due to the long tails associated with a Lorentzian intensity profile, a fraction of the beam will hit the constrictions of the device even if positioned in the center.

Exemplary 2D diffractograms for the RT and HT sample are shown in Fig. 5.7. The photon energy $h\nu$ is chosen individually to suit the diffraction conditions of selected diffraction peaks. To determine the crystallinity of a sample, the integrated intensity $I_{n,\mathrm{raw}} = \sum^{\mathrm{pixel}} i_{\mathrm{pixel}}$ is calculated in a region of interest (ROI) around the respective peak position. i_{pixel} is the total x-ray count of each pixel and n is the experiment index. The x-ray intensity of the beamline varies slightly over time, so $I_{n,\mathrm{raw}}$ is normalized to the background signal I_{bg} which is calculated from a ROI that contains only diffuse scattering and fluorescence signals. The positions of the off-specular diffraction spots, e.g. (013) and (123), depend on the oop and ip lattice constants of the Nb. A deformation of the crystal, analog to the piezoelectric effect, would therefore be visible as movement of the peaks. A deformation of the unit cell induces an anisotropic resistivity comparable to the AMR and, hence, would resemble the NSOT switching in a nonmagnetic material as well. A movement of peaks is not observed in any experiment which negates this alternative explanation of the transverse resistance variation seen in Fig. 5.4.

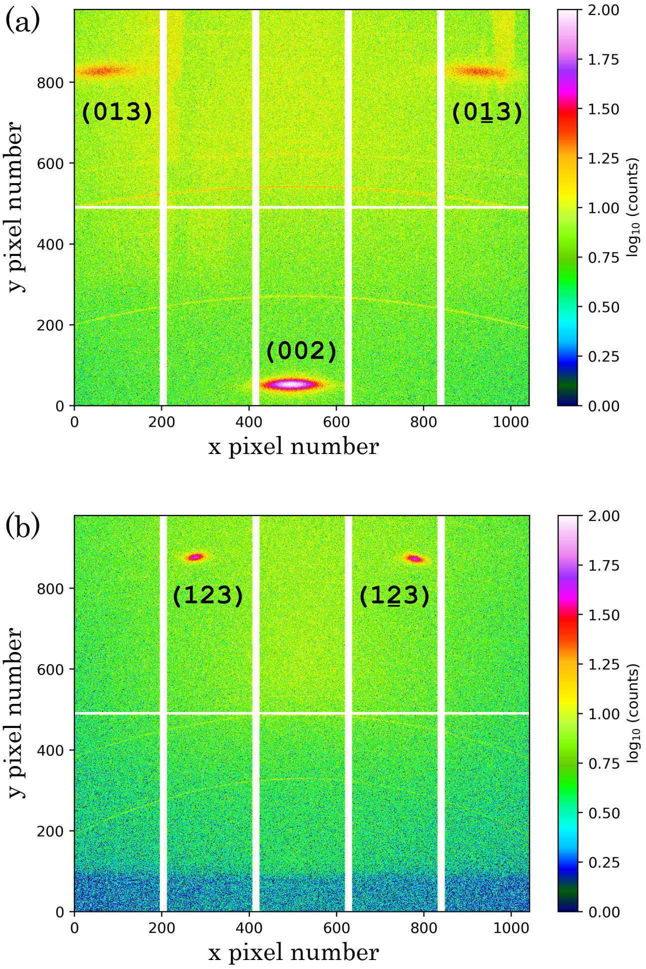

FIGURE 5.7: Exemplary 2D diffractograms measured with monochromatic x-rays of energy $h\nu$. The reflexes result from the Nb film and are labeled with Miller indices. The rings are due to the polycrystalline Al bonding wires. (a) RT sample measured with $h\nu = 11.2\,\mathrm{keV}$. (b) HT sample measured with $h\nu = 12.6\,\mathrm{keV}$. The low-intensity area at the bottom is caused by shadowing from the C-DIP frame.

The expectation regarding the presented evaluation scheme is, that each time the bursts are applied in $x(y)$ direction an enhancement $I_{n,\mathrm{raw}}/I_{\mathrm{bg}}$ is obtained in diffractograms measured at the $x\pm$ $(y\pm)$ position with a slight enhancement for the C position due to the expanded intensity profile of the x-ray spot [cf. Fig. 5.6]. The µXRD peak intensities measured at the constrictions that are not used for pulsing should not change significantly. In Fig. 5.8 the evaluation of the normalized peak intensity $I_n = I_{n,\mathrm{raw}}/I_{\mathrm{bg}}$ divided by I_0 under continuous electrical stress is shown. Panel (a) shows the RT and the (b) HT sample, respectively. Because of the noisy signal, the measured value $I_{n=0}$ is not suitable for normalization of the measurements. Instead, the normalization factor I_0 is determined by applying a linear fit individually to each data set (n, I_n). The experiment index on the x-axis is a number raised with each pulsing-relaxation sequence containing no information about j or the pulsing direction. The pulse lines are altered with each raise of the experiment index. However, note that a more sophisticated plot containing the omitted information yields no more insight due to the huge scattering of the data. The error bars are calculated as $\Delta I_n = \sqrt{I_n}$ following Poisson statistics which implies the assumption of a perfect detector. This methodology underestimates the error but allows to compare data sets of varying peak intensities. Note that the data sets shown in Fig. 5.8 (a) have varying errors which change systematically with measurement position and observed peak. This apparent inconsistency can be regarded as an artifact due to the movement of the sample stage in combination with a measurement performed at imperfect diffraction condition. For the RT sample $h\nu$ is chosen to capture simultaneously specular and off-specular peaks which comes with the cutback that neither peak is measured at optimized diffraction condition. As consequence, the measured intensity is highly sensitive to changes of the sample's angles with respect to the beam. The peaks with comparably small error correlate with the movement direction of the stage along the x direction. Hence, this effect is most likely caused by a tiny mechanical instability of the setup, i.e. each time the sample stage moves it tilts slightly with respect to the beam. Due to this technical issue, which is most prominent for movements along x direction, the brightness data scatters significantly more than expected from photon counting statistics. This mechanism has no effect on the measurement performed on the HT sample because $h\nu$ is optimized solely for the off-specular peaks and, thus, the measured peak intensity is stable with respect to small variations of the samples orientation.

Pulsing-µXRD experiments are conducted either until the sign of the response inverts or the device breaks. j is gradually increased to maintain a $\Delta R_\perp$ of similar magnitude. For the RT sample the current density is varied in the range $j_{\mathrm{RT}} = (7.0 \ldots 7.8) \times 10^{11}\,\mathrm{A/m^2}$ and $j_{\mathrm{HT}} = (7.4 \ldots 9.0) \times$

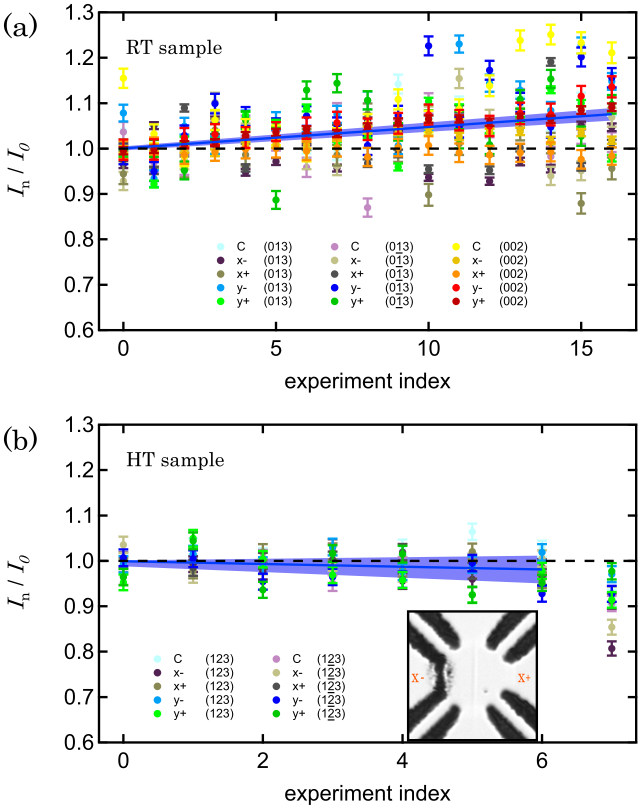

FIGURE 5.8: Plots of the normalized peak intensities I_n divided by their value prior to the pulsing experiment for (a) the RT and (b) the HT sample. Error bars are calculated as $\Delta\left(I_n/I_0\right) = \sqrt{I_n}/I_0$. The experiment index increases with every pulsing-relaxation sequence. 2D diffractograms are taken and evaluated for each peak and every position on the sample. The dashed black lines represent $I_n/I_0 \equiv 1$. Linear fits of the data are shown as blue lines with blue areas representing a 3σ surrounding obtained from the fit. The fit in (b) is applied for experimental index $n = 0\dots6$. The inset shows a micrograph of the broken device after $n = 7$.

10^{11} A/m^2 for the HT sample, respectively. The radiation itself does not affect the electrical readout during T_{relax}, therefore it is assumed that the sample is not altered by the µXRD measurement.

To overcome the unsatisfying signal-to-noise ratio a more general examination of the data is applied. Instead of looking at the individual positions, all datasets are collected and a linear regression $y = y_0 + m \cdot n$ is applied to extract the trend of peak intensity under repeated electrical pulsing. Each data point is weighted according to its individual error ΔI_n from photon counting statistics. In Fig. 5.8, these regressions are visualized by the blue lines. The blue areas indicate a 3σ error band. Note that the fit result is dominated by the data points with comparably low error and, hence, the calculated uncertainty is small as well. Tab. 5.1 contains the summarized results of this investigation. The HT device was destroyed during the experiment with index 7 where pulses were applied in x direction. It can be seen in Fig. 5.8 (b) that the peak intensity measured at the $x-$ position after destruction drops about 20%, which is significantly less compared to the other positions. An optical micrograph verifies that indeed the $x-$ constriction is the one which broke during the experiment. Thus, the linear regression is restricted to $n = 0 \dots 6$. This observation additionally validates that the x-ray spot is significantly larger than the 5 µm FWHM suggest.

Concluding one can say that the RT sample shows an enhancement of µXRD peak intensity under repeated electrical pulsing while the HT is greatly unaffected by the pulses prior to destruction. Hence, the µXRD data can be regarded as indication for an enhanced crystallinity of the RT sample due to the electrical pulsing. The result for the HT sample aligns with this assumption since no enhancement of the µXRD peak intensity is observed, which is consistent with the already good crystallinity [cf. Fig. 5.1]. The negative slope obtained for the HT sample could even be interpreted as an indication for local destruction of the sample. However, judging from the 3σ error band this conclusion is rather vague. Dislocation of atoms due to electromigration occurs primarily in grain boundaries and, thus, the effect on the µXRD peak intensity should be small anyway.

Sample	slope $m \pm \sigma_m$	$y-$intercept $y_0 \pm \sigma_{y_0}$
RT [cf. Fig. 5.8 (a)]	$+4.7‰ \pm 0.2‰$	1.000 ± 0.002
HT [cf. Fig. 5.8 (b)]	$-3.1‰ \pm 1.1‰$	0.999 ± 0.004

Table 5.1: Results obtained from the microdiffraction evaluation illustrated in Fig. 5.8. For the HT sample only data points $n = 0 \dots 6$ are considered due to the destruction of the device at $n = 7$. The given uncertainties are the parameter error estimates σ obtained from the parameter covariance matrix of the linear fit. Note that $y_0 \simeq 1$ results from the normalization routine.

5.3.3 Pulsing experiments at Nb with simultaneous electron microscopy

The µXRD investigation presented in Sec. 5.3.2 provided evidence that high currents passing through a *Union Jack* device indeed promote an annealing of the film as proposed in Sec. 5.2.1. The HT sample, however, has to be investigated in more detail to uncover a gradual destruction of the film prior to an eventual meltdown. In this section, pulsing experiments are followed by SEM imaging to investigate lateral changes of the films morphology. The electrical contacting is identical to Sec. 5.3.2 but with a device that is rotated by 45° with respect to the MgO edge. The used pulses are similar, e.g. the pulse width is $\Delta t = 10\,\mu\text{s}$. A SEM image showing the device prior to any pulsing is shown in Fig. 5.9. The image appears slightly blurred due to the low acceleration voltage of $\text{EHT} = 5\,\text{kV}$ to increase the surface sensitivity of the imaging.

Out of convenience the following measurements are conducted on a fresh device on the RT sample since both signs of the nonmagnetic switching are present in that sample and can therefore be investigated successively [cf. Fig. 5.4 (a)]. After each pulsing-relaxation sequence a SEM image is taken with the device grounded while taking the image. The pulses are applied primarily along x direction with a single pulsing-relaxation sequence applied in y direction to demonstrate that the sign of $\Delta R_\perp$ depends on the

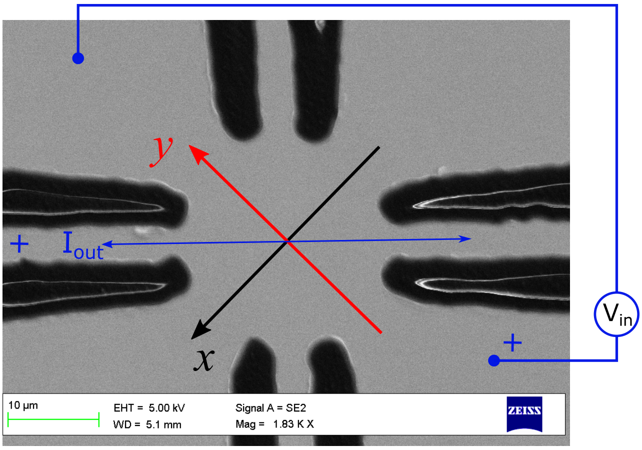

FIGURE 5.9: SEM image of a 45° device on the RT sample prior to any pulsing with arrows to indicate the electrical contacting analog to Fig. 3.4.

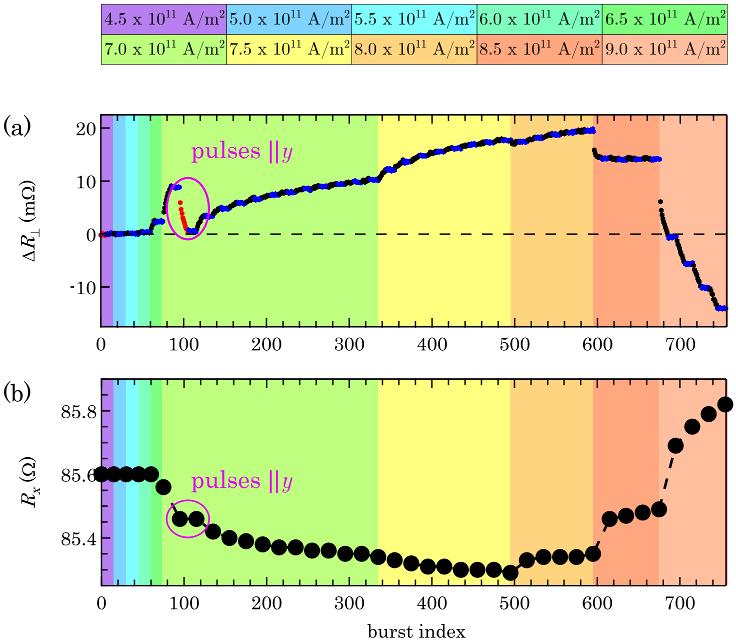

FIGURE 5.10: (a) $\Delta R_\perp$ response to bursts of different j. The colors of the data points match the arrows (red, black) in Fig. 5.9 to identify the pulsing direction and the relaxation phase (blue). The background coloring highlights the magnitude of j with respective numbers noted in the legend above. (b) The x-pulse line resistance R_x is measured prior to each pulsing-relaxation sequence. R_x does not change if the pulses are applied in y direction.

pulsing direction as in preliminary experiments. The $\Delta R_\perp$ response of the system and the values of R_x, taken intermittently as described in Chap. 3, are plotted in Fig. 5.10 (a) and (b), respectively. For $j \leq 6.0 \times 10^{11}$ A/m^2 neither a transverse response nor a change of R_x can be seen. Starting with $j = 6.5 \times 10^{11}$ A/m^2 a response with $\Delta R_\perp > 0$ and a decrease of R_x is observed. Further increasing j enhances the transverse response and the resistance change ΔR_x alike. Pulsing in y direction changes the sign of $\Delta R_\perp$ and has no impact on R_x. For successive bursts in the same direction, $\Delta R_\perp$ and ΔR_x seem to saturate until j is increased again. There is a crossover between reducing and increasing R_x at $j = 8.0 \times 10^{11}$ A/m^2 where the change of the transverse response also changes sign, superposed by a drift to higher values of $\Delta R_\perp$. This change in sign becomes more apparent for even higher j until a response associated to the HT sample, cf. Fig. 5.4 (b), is obtained for $j = 9.0 \times 10^{11}\ \mathrm{A/m^2}$.

All SEM images taken inbetween the pulsing-relaxation sequences for $j \leq 9.0 \times 10^{11}\ \mathrm{A/m^2}$ show no change of the samples features and are therefore not shown.

For larger current densities the effect size greatly enhances, as seen for $j = 9.5 \times 10^{11}\ \mathrm{A/m^2}$ in Fig. 5.11 (a) and (b). For this current density, the transverse response intermittently has a positive sign, while the overall trend is negative. R_x increases with each successive experiment until the device breaks. The lower left constriction of the structure displays morphological changes from sequence to sequence beginning with the first experiment at $j = 9.5 \times 10^{11}\ \mathrm{A/m^2}$ until destruction. Two SEM images taken after the second and fifth pulsing-relaxation repeat are shown in Fig. 5.11 (c) and (d), respectively. The destruction appears to be due to a meltdown of the film with droplets of material moving in electron flow direction. This visual-

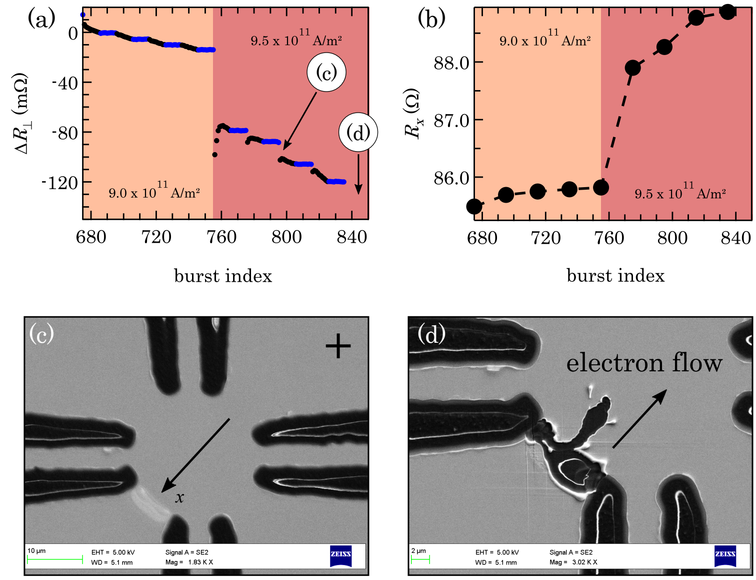

FIGURE 5.11: In (a) and (b) the continuation of Fig. 5.10 for $j = 9.5 \times 10^{11}\ \mathrm{A/m^2}$ is plotted with data overlap, i.e. the data for $j = 9.0 \times 10^{11}\ \mathrm{A/m^2}$ exits in both figures. (c) and (d) show SEM images of the device after the second (c) and fifth (d) repeat with $j = 9.5 \times 10^{11}\ \mathrm{A/m^2}$. The arrow in (d) indicate the electron flow direction that correlates with the formation of droplets after meltdown of the device in the constriction.

ization of momentum transfer between conduction electrons and Nb atoms supports the hypothesis of electromigration posed in Sec. 5.2.2.

The investigation presented in this section explicitly links the different signs of the nonmagnetic contribution to $\Delta R_\perp$ to a decrease and increase of $R_{x,y}$. As discussed in Sec. 5.3.2, the mechanism that decreases $R_{x,y}$ is a current induced annealing of the pulse lines. The increase of $R_{x,y}$ is proposed to be due to electromigration. The $R_{x,y}$ increase becomes significant way before any damage is observable in SEM imaging. The picture of the melted constriction provides only hints to electromigration. However, it has to be recognized that the literature [83–85, 87, 88] provides plenty examples where electromigration has been found to be the key mechanism for the destruction of micristructures. Hence, the assumption that electromigration causes the increase of $R_{x,y}$ will be regarded as affirmed in the following. Furthermore, the SEM images show that morphological changes of the sample are located in the constrictions of the device, i.e. in areas of high current density.

5.4 Discussion of resistive contributions in switching experiments using simulations based on the finite-element-method

The results presented in Sec. 5.3 provide strong evidence that the proposed mechanisms, namely current induced annealing and electromigration, are responsible for the observed change of pulse line resistances $R_{x,y}$. The changes are located in areas of the *Union Jack* device that experience the highest current densities. Hence, the local resistivity change $\Delta\rho$ is asymmetric with respect to the probe current I_out. As consequence, the probe current distribution will be asymmetric as well, inducing transverse voltages that resemble the PHE symmetry obtained in NSOT switching experiments [cf. Chap. 4].

In the following, the presented experimental evidence will be discussed by the help of FEM simulations. The calculations are performed with version 4.2 of the free FEMM software package [73, 74]. Fig. 5.12 shows the locally resolved current density for the *Union Jack* devices patterned by UVL during a current pulse. The current density is highest in the constrictions with a concave profile. A change of $R_{x,y}$ is due to a change of resistivity $\Delta\rho$ in the area of high current density only. Hence, the relative proportion of the constriction to the total resistance has to be calculated.

To shorten the following equations $R_0 \equiv R_{x,y}$ is used. The relative proportion to the total resistance that relate to a specific area of a given device can be calculated using the FEM. A suitable simulation setup is sketched

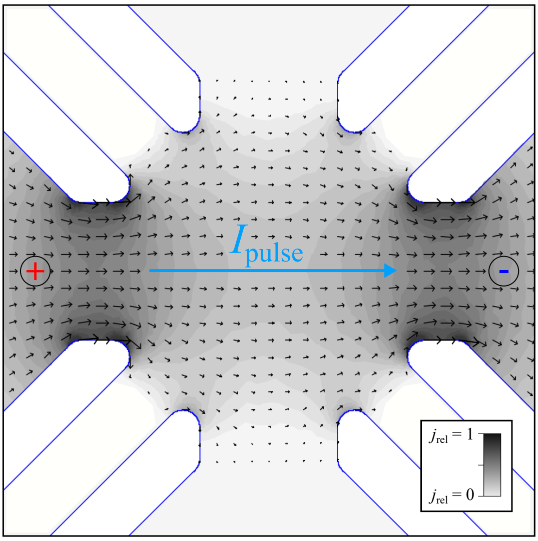

FIGURE 5.12: Greyscale plot of the locally resolved relative current density magnitude $j_{\text{rel}} = |\boldsymbol{j}/j_{\text{max}}|$ in a *Union Jack* device. The arrows show the local direction of $\boldsymbol{j}$. The boundary conditions resemble a pulse applied horizontally (x-direction). The area of highest current density follows a concave area in the constrictions of the device.

in Fig. 5.13. Here, the contact pads and most parts of the device have the resistivity ρ. The constrictions are modeled by rectangles that may have a different resistivity ρ^*. As pointed out above, in reality the area of resistivity change is concave. However, it turns out that the actual shape of this area has only a small impact on the simulated perpendicular resistance R_{FEM} obtained from the model. This has been tested for rectangular, concave, and convex areas. Hence, this description will consider rectangular areas for simplicity. The boundary conditions for the simulation are:

- Potential at the edge of the right contact pad is $V_{\text{R}} = 0\,\text{V}$ (grounded).
- A constant current $I_{\text{in}} = 1\,\text{A}$ is injected into the left contact pad.

The simulation evaluates which voltage V_{L} applied to the left contact pads edge solves the problem. For $R_{\text{c}} \ll R_0$ the relative proportion of the constrictions resistance R_{c} to the total resistance R_0 can be calculated by com-

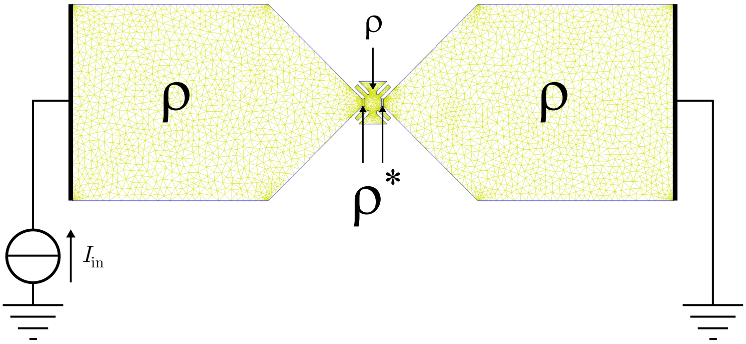

FIGURE 5.13: FEM mesh of the *Union Jack* device including the horizontal contact pads. A constant current I_{in} is injected into the left contact pad while the right one is grounded. The film has a resistivity ρ while rectangular areas in the horizontal constrictions of the *Union Jack* device have the resistivity ρ^*. The contact pads have realistic dimensions of $(100 \times 100)\ \mu\mathrm{m}^2$.

paring two conditions. First, $\rho^* = \rho$ is considered which results in

$$V_{\mathrm{L}}^{1\rho} = (R_{\mathrm{c}} + R_{\mathrm{R}})\, I_{\mathrm{in}} \tag{5.5}$$

that solves the problem. $R_{\mathrm{R}} = R_0 - R_{\mathrm{c}} \approx R_0$ is the resistance that is not due to the constrictions. The second simulation uses $\rho^* = 2\rho$ which results in the solution

$$V_{\mathrm{L}}^{2\rho} = (2R_{\mathrm{c}} + R_{\mathrm{R}})\, I_{\mathrm{in}}. \tag{5.6}$$

$V_{\mathrm{L}}^{1\rho}$, $V_{\mathrm{L}}^{2\rho}$ and I_{in} are known which allows to solve for R_{c} and R_{R} distinctively. This results in

$$\frac{R_{\mathrm{c}}}{R_0} \approx \frac{R_{\mathrm{c}}}{R_{\mathrm{R}}} = 6.36\% \approx 6\%. \tag{5.7}$$

Note that R_{c} is the sum of the resistance of opposing constrictions. Hence, each constriction accounts for ≈ 3% of the total pulse line resistance.

This consideration can be used to translate a change of the pulse line resistance ΔR_0 into a resistivity change in the constriction. Before and after a burst sequence two resistivities R_0 and R_0' are measured, respectively. Only the resistance of the constrictions changes due to the bursts. Hence, one obtains

$$R_0 = R_{\mathrm{c}} + R_{\mathrm{R}} \tag{5.8}$$

and

$$R'_0 = R'_\mathrm{c} + R_\mathrm{R} \tag{5.9}$$

with R_R being unaffected by the pulses. With Eq. (5.7) one can set

$$R_\mathrm{R} = 0.94\,R_0 \qquad \text{and} \qquad R_\mathrm{c} = 0.06\,R_0 \tag{5.10}$$

which allows to transform Eq. (5.9) to:

$$\frac{(R'_0/R_0) - 1}{0.06} = \frac{\Delta R_\mathrm{c}}{R_\mathrm{c}} \tag{5.11}$$

R_c and ΔR_c are connected to their respective resistivities by identical geometric parameters. Hence,

$$\frac{\Delta \rho_\mathrm{c}}{\rho_\mathrm{c}} = \frac{\Delta R_\mathrm{c}}{R_\mathrm{c}} \tag{5.12}$$

and, therefore,

$$\frac{\Delta \rho_\mathrm{c}}{\rho_\mathrm{c}} = \frac{(R'_0/R_0) - 1}{0.06} \tag{5.13}$$

links the relative change of the constrictions resistivity $\Delta\rho_\mathrm{c}/\rho_\mathrm{c}$ to the measured relative pulse line resistance change R'_0/R_0.

From the variation of R_x in Fig. 5.10 (b) one can calculate a $\Delta\rho_\mathrm{c}/\rho$ of about -6% around burst index 495. Here, the measured perpendicular resistance change is $\Delta R_\perp = +17.7\,\mathrm{m}\Omega$. That the constrictions relative proportion to the total resistance and $\Delta\rho_\mathrm{c}/\rho$ are similar is a coincidence and will vary for differently shaped devices. To check whether $\Delta\rho_c$ can account for $\Delta R_\perp$ FEM simulations are performed. The resistivity of the film is set to ρ_RT and the resistivity in the constrictions is $\rho_\mathrm{a} = \rho_\mathrm{RT} + \Delta\rho_c = 0.94\,\rho_\mathrm{RT}$ [cf. Fig. 5.14]. The simulation considers a dc sensing current I_s which resembles the in-phase response to an ac output current I_out driven by the Lock-In amplifier. As seen in Fig. 5.14, a transverse voltage arises due to the symmetry break about the sensing current direction with simulated transverse resistance is $R_\mathrm{FEM} = +8.7\,\mathrm{m}\Omega \approx 0.5\,\Delta R_\perp$.

In Fig. 5.12 one can see that the highest values of j are located at the device's edges close to the probe lines and also outside of the area that is considered for resistivity changes. The local modification of ρ will be concentrated where j is highest. The intersections between area of resistivity change and device contour cannot be moved easily in FEMM. Hence, these positions are fixed for every investigated shape of that area although the real

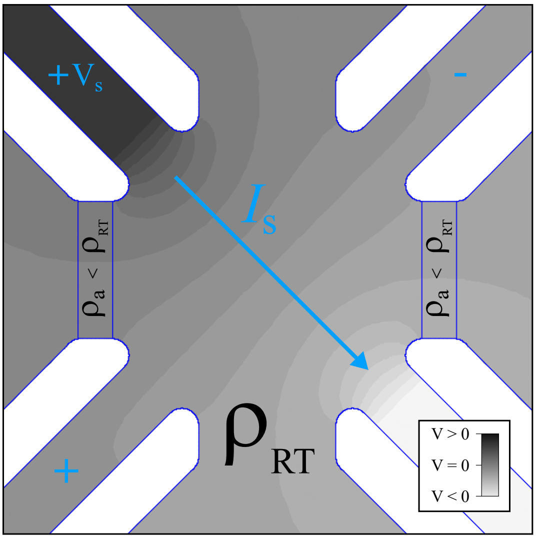

FIGURE 5.14: Greyscale plot of the potential landscape in a *Union Jack* device for an applied sensing current I_s. The boundary conditions resemble a measurement in PHE geometry [cf. Fig. 3.4]. Rectangular areas in the constrictions of the horizontal pulse line have reduced resistivity ρ_a. The simulation reveals the rise of a voltage perpendicular to I_s which resembles the PHE symmetry.

area of resistivity change ranges further towards the probe line as set for the simulation. This is troublesome because resistivity changes have more effect on the probe current if they are located closer to the probe lines. The discrepancy $\Delta R_\perp \approx 2 \times R_{\text{FEM}}$ is most likely due to the simplicity of the model, i.e. that the hot spot areas are not fully captured in the local resistivity change, which is due to limitations by the software. In Fig. 5.15 the experimental findings are compared to calculations made with the model using rectangular constrictions, where the local resistivity variation is calculated on the basis of the change in pulse line resistance. The qualitative agreement between experiment and simulation is remarkably good. Hence, the conclusion is that the transverse voltage that resembles the PHE in nonmagnetic *Union Jack* devices is largely due to a local change of the resistivity $\Delta\rho_c$ in the constriction.

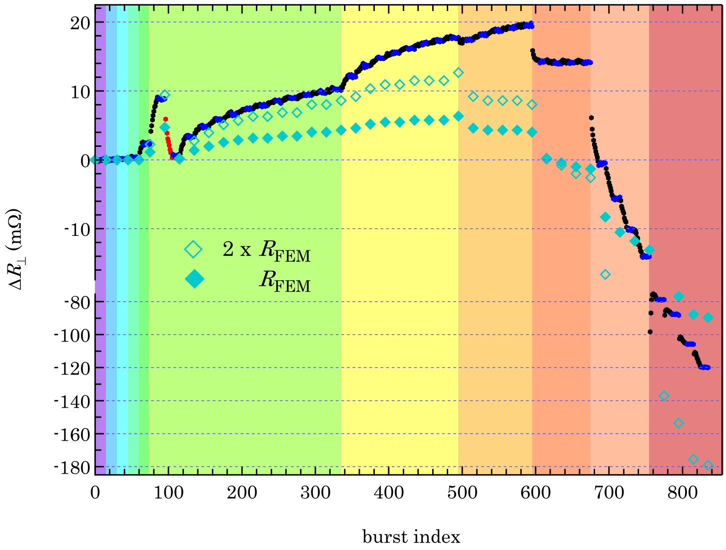

Figure 5.15: Comparison between R_{FEM}, calculated form the pulse line resistance in Fig. 5.10 (b), and $\Delta R_\perp$. The coloring of the data points for $\Delta R_\perp$ and the background is analog to Fig. 5.10. The quantitative agreement is astonishing for $j \leq 7.0 \times 10^{11}$ A/m^2 if the scaled values $2 \times R_{\text{FEM}}$ are used.

5.5 Discussion of competing explanation approaches

The first manuscript that identified a nonmagnetic contribution in current driven switching experiments was uploaded on arXiv.org in June 2019 and was written by Cheng *et al.* [90]. The peer-reviewed version was published in 2020 [91]. Here, Cheng *et al.* identified a "saw-tooth"-shaped contribution in $R_\perp$ measurements arising from the Pt layer in a $\alpha\text{−Fe}_2\text{O}_3$/Pt heterostructure that occurs if large current densities are applied to the device. The signal was present in devices made of a Pt single layer as well, which is analog to the epitaxial Nb films investigations. The manuscript of Cheng *et al.* does not propose an explanation, they only report the existence.

In November 2019, Chiang *et al.* obtained similar results and proposed a model to explain their finding [92]. They suggest that the high pulse currents lead to lateral temperature gradients and, thus, to Seebeck voltages which contribute to $R_\perp$ measurement. According to Cheng's interpretation, these voltages are of significant magnitude and persist over hours.

During this investigation there was no time dependent longitudinal or transversal resistance changes during the relaxation observable. Hence, the temperature of the *Union Jack* device is constant during the relaxation which is in line with You's calculation that predicts a decay of the device temperature within tens of microseconds after the pulse current is switched off [cf. Fig. 2.14 (b)]. This work therefore provides no evidence that supports the presence of lateral temperature gradients seconds after the pulse as suggested by Chiang *et al.*. In the supplementary material of Chiang's publication [92] one can see that they observe a significant change of the longitudinal resistance in their devices which they do not discuss with regard of its effect on $R_\perp$. The proposed model based on thermal gradients can also not explain the positive or negative signs of the transverse voltage that correlate with the pulse line resistance changes. Following the model developed in the course of this thesis, the longitudinal resistance change can explain their observation without the assumption of any temperature gradients. Thus, this competing explanation that is solely based on thermal gradients and associated thermovoltages is inconsistent with the data obtained in this work.

5.6 Summary on resistive contributions in switching experiments

The second part of this thesis dealt with effects of nonmagnetic origin that can occur if high currents are driven through *Union Jack* devices. As model system two Nb thin films have been prepared by dc-magnetron sputtering on MgO (001) substrates. By choosing different deposition temperatures the samples were designed to have different degrees of crystallization, i.e., one sample was polycrystalline, and one was epitaxial. The transport experiments, which are analog to those used to observe NSOT switching via the PHE [cf. Chap. 4], were conducted with *operando* µXRD and SEM measurements to reveal the underlying mechanisms that facilitate a nonmagnetic contribution in PHE measurement geometry.

In summary, the observation is reasoned by a gradual change of the sample's resistivity by electrical stress. This change is located in the areas of the *Union Jack* device that experience the highest current densities, i.e. the constrictions of the device. The local resistivity change leads to a transverse voltage in PHE measurement geometry due to the symmetry break of the device's properties about the axis defined by the sensing current [cf. Fig. 5.14]. Pulsing along the orthogonal channel restores the mirror symmetry by also reducing/increasing the resistivity in the other constriction. From the pulse line resistance changes $\Delta R_{x,y,} (\neq \Delta R_{xy})$ the magnitude of resistivity change $\Delta\rho_\mathrm{c}$ in the constrictions is estimated by the help of an FEM simulation. The obtained value for $\Delta\rho_\mathrm{c}$ is used to perform further FEM simulations allowing to calculate an expected tranverse resistance change $R_{\text{FEM}}(\Delta R_{x,y})$ which is then compared to the measurement result $R_{\perp}$. The findings are in semi-quantitative agreement.

The decrease and increase of the local resistivity is attributed to a crystallization and destruction of the sample, respectively. *Operando* SEM imaging and µXRD measurements support this interpretation. The crystallization or annealing effect, induced by joule heating, is not visible in SEM images, whereas the µXRD results corroborate the hypothesis of local crystallization in polycrystalline films. The sample destruction becomes significant in the transverse and pulse line resistance way before any morphological change could be seen in SEM images. The destructive mechanism is most likely electromigration which is supported by literature [83–86], although a solid proof for this particular experiment is yet missing. Throughout this study, it was found to be irreversible and relaxation was not observed. Thus, it is probable that as long as the electrically set state relaxes, the observed perpendicular resistance change is, at least partially, due to a switching of the magnetic order.

Conclusion and Outlook 6

Antiferromagnets have been important components in *spintronic* devices for decades and are highly relevant up to the present day. Their classical role is to passively modify the properties of ferromagnets via the exchange bias effect. Then the engineered ferromagnet acts as an active component of the *spintronic* device, e.g. to store information by the orientation of its magnetization. The fledging field of *antiferromagnetic spintronics* successfully demonstrated various concepts to utilize an antiferromagnet as an active component in these kind of devices. The most relevant advantages of antiferromagnets are their insensitivity to external magnetic fields and their ultrafast dynamics which, in principle, allow for information writing times in the picosecond time scale.

A promising mechanism to imprint information into an antiferromagnet is to send an electrical current through a thin film of a material in which the antiferromagnetic sublattices form inversion partners. In such a material the electrical current gives rise to the Néel-order spin-orbit torque (NSOT). This torque acts on the Néel order to eventually align the Néel vector $\boldsymbol{L}$ in the film plane, perpendicular to the driving current. A device in which the current can be directed into orthogonal directions can therefore be used as a digital memory cell. The information read-out can be realized by the planar Hall effect (PHE) through additional probe lines. This type of structure is called Union-Jack device [cf. Fig. 3.4]. The switching characteristics of these devices can be investigated with a pulse-probe transport experiment, portrayed in Chap. 3. This kind of experiment is typically referred to as a switching experiment.

Tetragonal CuMnAs possesses the symmetry required to generate the NSOT. The material can be grown with decent crystalline quality on GaAs substrates using dc-magnetron sputtering as described in Sec. 4.1. Observations made in switching experiments, illustrated in Sec. 4.2, reveal that the NSOT mechanism alone is insufficient to describe the observed dynamics. The extension of the NSOT theory to be a thermally activated or assisted process bears predictions to the dependency of the switching efficiency on the sample temperature, current pulse density, and current pulse width. The experimental findings are in line with the predictions made by the thermal activation model [cf. Sec. 2.3]. As seen in Fig. 4.7 (a) the temperature dependence of the switching efficiency is rather weak considering that it was found to be a thermally activated process. The reason for this peculiarity is the granularity of the dc-sputtered CuMnAs film. Each grain making up the film has a volume which defines its magnetic anisotropy energy barrier that must be overcome in a switching process. Since the film consists of grains with different volumes the switching can be observed at a range of different temperatures [cf. Fig. 4.7 (a)]. Hence, the referenced plot is a nontrivial transformation of the films grain size distribution [cf. Sec. 4.3]. One can summarize that the observable switching at a given temperature always originates from a subset of grains that fulfill a certain thermal stability criterion, i.e. $27 \lesssim \Delta_T \lesssim 44$. It also implies that the NSOT in the investigated film is relatively weak and the switching itself relies on thermal assistance, thereby always leading to a thermally unstable state which has limited relevance for information storage applications. This process facilitates memristive behavior which can be used for neuromorphic computing. The issue with the thermally unstable final state could be compensated by a variation of the pulse form. The cool down of the sample after the current is switched off takes a couple of microseconds [cf. Fig. 2.14 (b)]. In the presented experiment, however, the current ramp-down time is much faster, i.e. $t_{\text{ramp}} = \min(0.25\,\Delta t, 1\,\mu\text{s})$. Hence, after a switching pulse the sample remains at an elevated temperature while the NSOT field is zero which results in enhanced relaxation. To overcome this issue the current ramp-down could be matched to the cool down profile. Then, the sample would experience a gradually decreasing NSOT field during cool down which should stabilize the switched state. Another approach to improve the utility of NSOT switching could be the application of rf sputtering to deposit films with a narrower grain size distribution, while maintaining its compatibility with a large scale production. This could significantly increase the switching amplitude at an optimized temperature, since a larger portion of the total grain size ensemble would be active at a time.

The small magnitude of the NSOT demands for high current densities to observe the switching. Those high current densities promote significant Joule heating of the film which assists the switching process. The switched state is to a large extent thermally unstable and equilibrates over time. This picture fully describes the observations made in the investigated CuMnAs thin film. However, there are more effects that must be taken into account if high currents are passing through hot solids. The ones examined in Chap. 5 of this work are electromigration and annealing. Note that the thermal-activation physics are similar for NSOT switching, annealing and electromigration, which makes it nontrivial to disentangle those contributions by switching experiments alone.

To investigate the electrical response facilitated by electromigration and annealing in a PHE like read-out configuration, as applied for NSOT switching experiments, Nb films with different degree of crystallization were prepared [cf. Sec. 5.1]. Although nonmagnetic, these films generate an electrical response similar to the PHE in a switching experiment [cf. Sec. 5.3.1]. The response of a sample with low crystalline quality was examined with respect to current-induced annealing by *operando* microdiffraction (μXRD) measurements [cf. Sec. 5.3.2]. It turns out that the current pulses enhance the crystallinity of the film. This is verified by an increase of diffraction intensity and a decrease in electrical resistivity. The investigation aimed to resolve a local variation in crystallinity since the current density in a Union-Jack device also varies locally. However, the technique did not allow to create a map of crystallinity due to the limitation of the ability to focus the x-ray spot. Nevertheless, it is reasonable to assume that the annealing process follows the current density distribution because the temperature rise of the film depends on the current density squared.

For the investigation of the electromigration component to the nonmagnetic response the epitaxial Nb sample was used. This sample cannot experience annealing since it is of good crystalline quality already. Investigations have been repeated with μXRD measurements and revealed no change in diffraction intensity until a meltdown of the device is observed. Here, the PHE like response coincides with an increase in electrical resistivity, indicating a gradual destruction of the film that is not visible in μXRD measurements. This effect has been further investigated by *operando* scanning electron microscopy (SEM) imaging as described in Sec. 5.3.3. The shown data corresponds with a sample of low crystal quality to successively investigate the morphological change of the film during annealing and destruction. One can see that a change in electrical resistivity has a significant magnitude way before morphological changes become resolvable by SEM. The visible destruction of the film is uniquely located in the device's constrictions, which are the areas of highest current density [cf. Fig. 5.11 (c) & (d)]. The formation of droplets that moved in electron flow direction, strengthens the hypothesis that electromigration is the root cause for the increase of resistivity.

The experiments conducted within this thesis confirm that high currents passing through a *Union Jack* device can induce PHE like responses in the electrical read-out that may superpose with the magnetic signal of a switching experiment. The mechanisms are most likely annealing and electromigration which decrease/increase the local resistivity of the film in the constrictions of the device. The local change of resistivity breaks the mirror symmetry of the device about the sensing current direction, which results in an asymmetric current flow that leads to a transverse voltage. Pulsing along the orthogonal direction restores this mirror symmetry which eventually resembles the PHE. This model has been checked for quantitative consistency using the Finite-Element-Method (FEM) [cf. Sec. 5.4]. The simulated transverse voltage deviates from the experiment by roughly a factor of two. This discrepancy can be attributed to the simplicity of the applied model which only allows for two different resistivity values in the device and the area of changed resistivity is fixed. A simulation that takes the current density profile of the pulse current to calculate a continuous resistivity change, may rectify this inaccuracy. Despite small numerical deviations the model provides a solid framework to understand one mechanism of nonmagnetic contributions that resembles the PHE symmetry.

As electromigration is a directed transport along the direction of electron flow, one may use single-cycle ac current pulses instead of dc pulses. If the current pulses are short enough, this should substantially reduce the directed transport, thereby increasing the device's lifetime by orders of magnitude [93]. Consequently, the resistivity-enhancing component of the transverse electrical response should be substantially reduced. However, the contribution due to annealing would remain affected. The contribution due to annealing could be removed by ac pulsed-current annealing the device with a large current density prior to systematic investigations.

Annealing and electromigration are irreversible and, thus, do not generate a time dependent transverse voltage as observed in the CuMnAs switching experiments [cf. Fig. 4.4]. Therefore, it is most likely that the observations made in this work are truly related to the reorientation of the Néel vector in CuMnAs by the NSOT. In future experiments, however, one should make sure to regularly measure the pulse line resistances and to check the reproducibility of the switching not only at one parameter set but in, e.g., current density sweeps. This is particularly relevant for experiments performed close to the destruction threshold of a device since they are particularly prone to the electromigration-like component of the nonmagnetic electrical response. Using the FEM model, developed in this thesis, can also help to distinguish between magnetic and nonmagnetic signals since a change of the pulse line resistance can be used to estimate the magnitude of the parasitic nonmagnetic contribution.

As a concluding short summary one can say: The attempt to observe NSOT switching in sputtered CuMnAs thin films was successful. Parasitic contributions in current induced switching experiments have been identified and quantitatively analyzed using various techniques. A methodology to quantify switching characteristics for magnetic switching and to estimate the potential corruption by nonmagnetic contributions has been developed. All key results are published in peer-reviewed journals and potential research gaps are addressed.

Bibliography

[1] J. W. Goethe. *Italienische Reise*. Hofenberg, 2016. (Vollständige Neuausgabe).

[2] M. Meinert, D. Graulich, and T. Matalla-Wagner. Electrical Switching of Antiferromagnetic Mn_2Au and the Role of Thermal Activation. *Phys. Rev. Appl.*, 9(6):064040, 2018.

[3] M. Dunz, T. Matalla-Wagner, and M. Meinert. Spin-orbit torque induced electrical switching of antiferromagnetic MnN. *Phys. Rev. Research*, 2(1):013347, 2020.

[4] T. Matalla-Wagner, M.-F. Rath, D. Graulich, J.-M. Schmalhorst, G. Reiss, and M. Meinert. Electrical Néel-Order Switching in Magnetron-Sputtered CuMnAs Thin Films. *Phys. Rev. Appl.*, 12(6):064003, 2019.

[5] T. Matalla-Wagner, J.-M. Schmalhorst, G. Reiss, N. Tamura, and M. Meinert. Resistive contribution in electrical-switching experiments with antiferromagnets. *Phys. Rev. Research*, 2(3):033077, 2020.

[6] A. Niesen, N. Teichert, T. Matalla-Wagner, J. Balluf, N. Dohmeier, M. Glas, C. Klewe, E. Arenholz, J.-M. Schmalhorst, and G. Reiss. Structural, magnetic, and electrical properties of perpendicularly magnetized $Mn_{4-x}Fe_xGe$ thin films. *J. Appl. Phys.*, 123(11):113901, 2018.

[7] R. Silber, O. Stejskal, L. Beran, P. Cejpek, R. Antoš, T. Matalla-Wagner, J. Thien, O. Kuschel, J. Wollschläger, M. Veis, T. Kuschel, and J. Hamrle. Quadratic magneto-optic Kerr effect spectroscopy of Fe epitaxial films on MgO(001) substrates. *Phys. Rev. B*, 100(6):064403, 2019.

[8] A. Moskaltsova, J. Krieft, D. Graulich, T. Matalla-Wagner, and T. Kuschel. Impact of the magnetic proximity effect in Pt on the total

magnetic moment of Pt/Co/Ta trilayers studied by x-ray resonant magnetic reflectivity. *AIP Advances*, 10(1):015154, 2020.

[9] D. Dyck, A. Becker, J. Koo, T. Matalla-Wagner, J. Krieft, and G. Reiss. Anomalous Hall Effect and Magnetoresistance in Sputter Deposited Magnetic Weyl Semimetal Co_2TiGe Thin Films. *Phys. Status Solidi B*, 258(1):2000067, 2021.

[10] A. Becker, D. Ramermann, I. Ennen, B. Büker, T. Matalla-Wagner, M. Gottschalk, and A. Hütten. The Influence of Martensitic Intercalations in Magnetic Shape Memory NiCoMnAl Multilayered Films. *Entropy*, 23(4):462, 2021.

[11] (Editorial) Upping the anti. *Nature Phys.*, 14(3):199, 2018.

[12] T. Jungwirth, J. Sinova, A. Manchon, X. Marti, J. Wunderlich, and C. Felser. (Comment) The multiple directions of antiferromagnetic spintronics. *Nature Phys.*, 14(3):200, 2018.

[13] L. Néel. Magnetism and the local molecular field. *Noble Lecture*, 1970.

[14] L. Néel. Influence des fluctuations du champ moléculaire sur les propriétés magnétiques des corps. *Ann. Phys.*, 10(18):5, 1932.

[15] C. G. Shull and J. S. Smart. Detection of Antiferromagnetism by Neutron Diffraction. *Phys. Rev.*, 76(8):1256, 1949.

[16] W. H. Meiklejohn and C. P. Bean. New Magnetic Anisotropy. *Phys. Rev.*, 102(5):1413, 1956.

[17] J. Nogués and I. K. Schuller. Exchange bias. *J. Magn. Magn. Mater.*, 192(2):203, 1999.

[18] S. Tehrani, J. M. Slaughter, E. Chen, M. Durlam, J. Shi, and M. DeHerren. Progress and outlook for MRAM technology. *IEEE Transactions on Magnetics*, 35(5):2814, 1999.

[19] S. A. Wolf, D. D. Awschalom, R. A. Buhrman, J. M. Daughton, S. von Molnár, M. L. Roukes, A. Y. Chtchelkanova, and D. M. Treger. Spintronics: A Spin-Based Electronics Vision for the Future. *Science*, 294(5546):1488, 2001.

[20] A. V. Khvalkovskiy, D. Apalkov, S. Watts, R. Chepulskii, R. S. Beach, A. Ong, X. Tang, A. Driskill-Smith, W. H. Butler, P. B. Visscher, D. Lottis, E. Chen, V. Nikitin, and M. Krounbi. Basic principles of STT-MRAM cell operation in memory arrays. *J. Phys. D: Appl. Phys.*, 46(7):074001, 2013.

[21] J. Železný, H. Gao, K. Výborný, J. Zemen, J. Mašek, A. Manchon, J. Wunderlich, J. Sinova, and T. Jungwirth. Relativistic Néel-Order Fields Induced by Electrical Current in Antiferromagnets. *Phys. Rev. Lett.*, 113(15):157201, 2014.

[22] P. Wadley, B. Howells, J. Železný, C. Andrews, V. Hills, R. P. Campion, V. Novák, K. Olejník, F. Maccherozzi, S. S. Dhesi, S. Y. Martin, T. Wagner, J. Wunderlich, F. Freimuth, Y. Mokrousov, J. Kuneš, J. S. Chauhan, M. J. Grzybowski, A. W. Rushforth, K. W. Edmonds, B. L. Gallagher, and T. Jungwirth. Electrical switching of an antiferromagnet. *Science*, 351(6273):587, 2016.

[23] J. Železný, P. Wadley, K. Olejník, A. Hoffmann, and H. Ohno. Spin transport and spin torque in antiferromagnetic devices. *Nature Phys.*, 14(3):220, 2018.

[24] L. Baldrati, H. Gomonay, A. Ross, M. Filianina, R. Lebrun, R. Ramos, C. Leveille, T. Forrest, F. Maccherozzi, E. Saitoh, J. Sinova, and M. Kläui. Mechanism of Néel Order Switching in Antiferromagnetic Thin Films Revealed by Magnetotransport and Direct Imaging. *Phys. Rev. Lett.*, 123(17):177201, 2019.

[25] T. Moriyama, K. Oda, T. Ohkochi, M. Kimata, and T. Ono. Spin torque control of antiferromagnetic moments in NiO. *Sci. Rep.*, 8(1):14167, 2018.

[26] R. Groß and A. Marx. *Festkörperphysik*. Walter de Gruyter GmbH, 2nd edition, 2014.

[27] C. Kittel. *Einführung in die Festkörperphysik*. Oldenbourg Wissenschaftsverlag GmbH, 15th edition, 2013.

[28] S. Hunklinger. *Festkörperphysik*. Oldenbourg Wissenschaftsverlag GmbH, 3rd edition, 2011.

[29] H. Ibach and H. Lüth. *Festkörperphysik*. Springer-Verlag Berlin Heidelberg, 7th edition, 2009.

[30] K. Kopitzki and P. Herzog. *Einführung in die Festkörperphysik*. Springer-Verlag GmbH, 7th edition, 2017.

[31] S. Blundell. *Magnetism in Condensed Matter*. Oxford University Press, 1st edition, 2001.

[32] T. L. Brown, H. E. LeMay, and B. E. Bursten. *Chemie : studieren kompakt*. Pearson, München, 10th edition, 2011.

[33] H. Gomonay and V. M. Loktev. Magnetostriction and magnetoelastic domains in antiferromagnets. *J. Phys. Condens. Matter*, 14(15):3959, 2002.

[34] T. Nagamiya, K. Yosida, and R. Kubo. Antiferromagnetism. *Adv. Phys.*, 4(13):1–112, 1955.

[35] L. Holmes, M. Eibschütz, and H. J. Guggenheim. Spin-flop transition in $BaMnF_4$. *Solid State Commun.*, 7(14):973, 1969.

[36] W. Thompson. On the electro-dynamic qualities of metals: Effects of magnetization on the electric conductivity of Nickel and Iron. *Proc. Roy. Soc.*, 8(1):546, 1857.

[37] T. R. Mc Guire and I. Potter. Amisotropic Magnetoresistance in Ferromagnetic 3*d* Alloys. *IEEE Trans. Mag.*, 11(4):1018, 1975.

[38] D. A. Thompson, L. T. Romankiw, and A. F. Mayadas. Thin Film Magnetoresistance in Memory, Storage, and Related Applications. *IEEE Trans. Mag.*, 11(4):1039, 1975.

[39] D. Meier. *Thermally generated spin and charge transport in magnetic materials*. PhD thesis, Bielefeld University, 2015.

[40] M. Bonfim, G. Ghiringhelli, F. Montaigne, S. Pizzini, N. B. Brookes, F. Petroff, J. Vogel, J. Camarero, and A. Fontaine. Element-Selective Nanosecond Magnetization Dynamics in Magnetic Heterostructures. *Phys. Rev. Lett.*, 86(16):3646, 2001.

[41] K. Garello, C. O. Avci, I. M. Miron, M. Baumgartner, A. Ghosh, S. Auffret, O. Boulle, G. Gaudin, and P. Gambardella. Ultrafast magnetization switching by spin-orbit torques. *Appl. Phys. Lett.*, 105(21):212402, 2014.

[42] (Editorial) Memory with a spin. *Nature Nanotech.*, 10(3):185, 2015.

[43] X.-Y. Feng, Q.-H. Zhang, H.-W. Zhang, Y. Zhang, R. Zhong, B.-W. Lu, J.-W. Cao, and X.-L. Fan. A review of current research on spin currents and spin–orbit torques. *Chin. Phys. B*, 28(10):107105, 2019.

[44] K. Olejník, V. Schuler, X. Marti, V. Novák, Z. Kašpar, P. Wadley, R. P. Campion, K. W. Edmonds, B. L. Gallagher, J. Garces, M. Baumgartner, P. Gambardella, and T. Jungwirth. Antiferromagnetic CuMnAs multi-level memory cell with microelectronic compatibility. *Nat. Commun.*, 8(1):15434, 2017.

[45] K. Olejník, T. Seifert, Z. Kašpar, V. Novák, P. Wadley, R. P. Campion, M. Baumgartner, P. Gambardella, P. Němec, J. Wunderlich, J. Sinova, P. Kužel, M. Müller, T. Kampfrath, and T. Jungwirth. Terahertz electrical writing speed in an antiferromagnetic memory. *Science Advances*, 4(3):eaar3566, 2018.

[46] S. Y. Bodnar, L. Šmejkal, I. Turek, T. Jungwirth, O. Gomonay, J. Sinova, A. A. Sapozhnik, H.-J. Elmers, M. Kläui, and M. Jourdan. Writing and reading antiferromagnetic Mn_2Au by Néel spin-orbit torques and large anisotropic magnetoresistance. *Nat. Commun.*, 9(1):348, 2018.

[47] X. F. Zhou, J. Zhang, F. Li, X. Z. Chen, G. Y. Shi, Y. Z. Tan, Y. D. Gu, M. S. Saleem, H. Q. Wu, F. Pan, and C. Song. Strong Orientation-Dependent Spin-Orbit Torque in Thin Films of the Antiferromagnet Mn_2Au. *Phys. Rev. Appl.*, 9(5):054028, 2018.

[48] S. LaShell, B. A. McDougall, and E. Jensen. Spin Splitting of an Au(111) Surface State Band Observed with Angle Resolved Photoelectron Spectroscopy. *Phys. Rev. Lett.*, 77(16):3419, 1996.

[49] S. D. Ganichev, S. N. Danilov, P. Schneider, V. V. Bel'kov, L. E. Golub, W. Wegscheider, D. Weiss, and W. Prettl. Can an electric current orient spins in quantum wells? *arXiv:cond-mat/0403641v1*, 2004.

[50] S. D. Ganichev, E. L. Ivchenko, V. V. Bel'kov, S. A. Tarasenko, M. Sollinger, D. Weiss, W. Wegscheider, and W. Prettl. Spin-galvanic effect. *Nature*, 417:153, 2002.

[51] S. D. Ganichev, S. N. Danilov, P. Schneider, V. V. Bel'kov, L. E. Golub, W. Wegscheider, D. Weiss, and W. Prettl. Electric current-induced spin orientation in quantum well structures. *J. Magn. Magn. Mater.*, 300(1):127, 2006.

[52] K. Momma and F. Izumi. *VESTA*: a three-dimensional visualization system for electronic and structural analysis. *J. Appl. Crystallogr.*, 41(3):653, 2008.

[53] P. Wadley, S. Reimers, M. J. Grzybowski, C. Andrews, M. Wang, J. S. Chauhan, B. L. Gallagher, R. P. Campion, K. W. Edmonds, S. S. Dhesi, F. Maccherozzi, V. Novak, J. Wunderlich, and T. Jungwirth. Current polarity-dependent manipulation of antiferromagnetic domains. *Nat. Nanotechnol.*, 13(5):362, 2018.

[54] P. Wadley, V. Hills, M. R. Shahedkhah, K. W. Edmonds, R. P. Campion, V. Novák, B. Ouladdiaf, D. Khalyavin, S. Langridge, V. Saidl, P. Nemec, A. W. Rushforth, B. L. Gallagher, S. S. Dhesi, F. Maccherozzi, J. Železný, and T. Jungwirth. Antiferromagnetic structure in tetragonal CuMnAs thin films. *Sci. Rep.*, 5(1):17079, 2015.

[55] C.-Y. You, I. M. Sung, and B.-K. Joe. Analytic expression for the temperature of the current-heated nanowire for the current-induced domain wall motion. *Appl. Phys. Lett.*, 89(22):222513, 2006.

[56] O. Gomonay, T. Jungwirth, and J. Sinova. High Antiferromagnetic Domain Wall Velocity Induced by Néel Spin-Orbit Torques. *Phys. Rev. Lett.*, 117(1):017202, 2016.

[57] D. L. Smith. *Thin-Film Deposition: Principles and Practice*. McGraw-Hill, 1st edition, 1995.

[58] K. Wasa, K. Isaku, and K. Hidetoshi. *Handbook of Sputter Deposition Technology*. William Andrew Publishing, 2nd edition, 2012.

[59] C. Mack. *Fundamental principles of optical lithography: the science of microfabrication*. John Wiley & Sons, 1st edition, 2008.

[60] R. F. W. Pease. Electron beam lithography. *Contemporary Physics*, 22(3):265, 1981.

[61] W. Beiglböck. *X-ray and Neutron Reflectivity*. Lecture Notes in Physics; 770. Springer-Verlag Berlin Heidelberg, 1st edition, 2009.

[62] L. Spieß, G. Teichert, R. Schwarzer, H. Behnken, and C. Genzel. *Moderne Röntgenbeugung*. Vieweg+Teubner, 2nd edition, 2009.

[63] T. D. T. Oyedotun. X-ray fluorescence (XRF) in the investigation of the composition of earth materials: a review and an overview. *Geology, Ecology, and Landscapes*, 2(2):148, 2018.

[64] A. Ikai and R. Afrin, editors. *Einführung in die Nanobiomechanik*. Wiley-VCH, Weinheim, 1st edition, 2010.

[65] M. Björck and G. Andersson. GenX: an extensible X-ray reflectivity refinement program utilizing differential evolution. *J. Appl. Crystallogr.*, 40(6):1174, 2007.

[66] Stanford Research Systems (SRS). About Lock-In Amplifiers. www.thinksrs.com/downloads/pdfs/applicationnotes/AboutLIAs.pdf.

[67] S. Xie. Practical Filter Design Challenges and Considerations for Precision ADCs. *Analog Dialogue*, 50(4):5, 2016.

[68] P. Brandimarte. *Handbook in Monte Carlo Simulation*. Wiley handbooks in financial engineering and econometrics. John Wiley & Sons, Inc., Hoboken, New Jersey, 1st edition, 2014.

[69] A. P. J. Jansen. *An Introduction to Kinetic Monte Carlo Simulations of Surface Reactions*. Lecture Notes in Physics; 856. Springer-Verlag Berlin Heidelberg, 1st edition, 2012.

[70] M. G. Larson and F. Bengzon. *The Finite Element Method: Theory, Implementation, and Applications*. Texts in Computational Science and Engineering 10. Springer-Verlag Berlin Heidelberg, 1st edition, 2013.

[71] C. Mehlhaff. Untersuchung der Symmetriebrechung des elektrischen Widerstands durch elektrische Ströme in metallischen Mikrostrukturen. Master's thesis, Bielefeld University, 2018.

[72] L. Neumann. Influence of the device geometry on spin-orbit torque experiments. Master's thesis, Bielefeld University, 2018.

[73] K. Baltzis. The FEMM Package: A Simple, Fast, and Accurate Open Source Electromagnetic Tool in Science and Engineering. *J. Eng. Sci. Technol. Rev.*, 1(1):83, 2008.

[74] D. C. Meeker. Finite Element Method Magnetics, Version 4.2 (28. Feb 2018 Build). http://www.femm.info.

[75] D. Graulich. Néel Order Spin Orbit Torque Switching in Mn_2Au. Master's thesis, Bielefeld University, 2018.

[76] P. Wadley, V. Novák, R. P. Campion, C. Rinaldi, X. Martí, H. Reichlová, J. Železný, J. Gazquez, M. A. Roldan, M. Varela, D. Khalyavin, S. Langridge, D. Kriegner, F. Máca, J. Mašek, R. Bertacco, V. Holý, A. W. Rushforth, K. W. Edmonds, B. L. Gallagher, C. T. Foxon, J. Wunderlich, and T. Jungwirth. Tetragonal phase of epitaxial room-temperature antiferromagnet CuMnAs. *Nat. Commun.*, 4(1):2322, 2013.

[77] CrysTec GmbH Kristalltechnologie. III – V Semiconductor data sheets. https://www.crystec.de/iiiv-d.html.

[78] D. C. Johnston. Stretched exponential relaxation arising from a continuous sum of exponential decays. *Phys. Rev. B*, 74(18):184430, 2006.

[79] K. O'Grady, L. E. Fernandez-Outon, and G. Vallejo-Fernandez. A new paradigm for exchange bias in polycrystalline thin films. *J. Magn. Magn. Mater.*, 322(8):883, 2010.

[80] M.-F. Rath. *Optimierung der Magnetronsputterdeposition von CuMnAs auf GaAs*. Bachelor's thesis, Bielefeld University, 2019.

[81] *Elektrotechniker-Handwerk: DIN-Normen und technische Regeln für die Elektroinstallation (Normen-Handbuch)*. Beuth Verlag GmbH, 9th edition, 2018.

[82] D. Errandonea, L. Burakovsky, D. L. Preston, S. G. MacLeod, D. Santamaría-Perez, S. Chen, H. Cynn, S. I. Simak, M. I. McMahon, J. E. Proctor, and M. Mezouar. Experimental and theoretical confirmation of an orthorhombic phase transition in niobium at high pressure and temperature. *Commun. Mater.*, 1(1):60, 2020.

[83] P. S. Ho and T. Kwok. Electromigration in metals. *Rep. Prog. Phys.*, 52(3):301, 1989.

[84] D. Pierce and P. Brusius. Electromigration: A review. *Microelectron. Reliab.*, 37(7):1053, 1997.

[85] K. Lee. Electromigration recovery and short lead effect under bipolar- and unipolar-pulse current. *IEEE International Reliability Physics Symposium (IRPS) Anaheim, CA*, pages 6B.3.1–6B.3.4, 2012.

[86] I. A. Blech and C. Herring. Stress generation by electromigration. *Appl. Phys. Lett.*, 29(3):131, 1976.

[87] K. A. Jackson. *Kinetic Processes: Crystal Growth, Diffusion, and Phase Transitions in Materials*. WILEY-VHC Verlag GmbH & Co. KGaA, 1st edition, 2004.

[88] J. R. Black. Electromigration - A brief survey and some recent results. *IEEE Trans. Electron Devices*, 16(4):338, 1969.

[89] M. Kunz, N. Tamura, K. Chen, A. A. MacDowell, R. S. Celestre, M. M. Church, S. Fakra, E. E. Domning, J. M. Glossinger, J. L. Kirschman, G. Y. Morrison, D. W. Plate, B. V. Smith, T. Warwick, V. V. Yashchuk, H. A. Padmore, and E. Ustundag. A dedicated superbend x-ray microdiffraction beamline for materials, geo-, and environmental sciences at the advanced light source. *Rev. Sci. Instrum.*, 80(3):035108, 2009.

[90] Y. Cheng, S. Yu, M. Zhu, J. Hwang, and F. Yang. Reliable Electrical Switching of Tri-State Antiferromagnetic Néel Order in $\alpha-Fe_2O_3$ Epitaxial Films. *arXiv:1906.04694v1*, 2019.

[91] Y. Cheng, S. Yu, M. Zhu, J. Hwang, and F. Yang. Electrical Switching of Tristate Antiferromagnetic Néel Order in $\alpha-Fe_2O_3$ Epitaxial Films. *Phys. Rev. Lett.*, 124(2):027202, 2020.

[92] C. C. Chiang, S. Y. Huang, D. Qu, P. H. Wu, and C. L. Chien. Absence of Evidence of Electrical Switching of the Antiferromagnetic Néel Vector. *Phys. Rev. Lett.*, 123(22):227203, 2019.

[93] B. K. Liew, N. W. Cheung, and C. Hu. Electromigration interconnect lifetime under AC and pulse DC stress. *27th Annual Proceedings., International Reliability Physics Symposium*, pages 215–219, 1989.

List of Acronyms

AFM	antiferromagnet	9
ALS	Advanced Light Source	83
AMR	anisotropic magnetoresistance	17
CCD	charge-coupled device	84
C-DIP	ceramic dual inline package	39
DSP	Digital Signal Processing	42
EBL	electron-beam lithography	38
EDX	Energy-dispersive x-ray spectroscopy	55
FEM	Finite-Element-Method	104
FiM	ferrimagnet	9
FM	ferromagnet	9
FS	fused silica	35
FWHM	full-width-at-half-maximum	84
HCl	technical hydrochloric acid 37%	36
HT	high temperature	76
ip	in plane	12
iSGE	inverse Spin Galvanic effect	22
kMC	kinetic Monte Carlo	44

LLGE	Landau-Lifshitz-Gilbert-Equation	20
MBE	Molecular Beam Epitaxy	22
MC	Monte Carlo	44
MTF	mean-time-to-failure	78
µXRD	microdiffraction	103
NSOT	Néel-order spin-orbit torque	101
oop	out of plane	12
PDE	partial differential equation	45
PES	potential-energy surface	29
PHE	planar Hall effect	101
PSD	Phase Sensitive Detection	41
ROI	region of interest	84
RT	room temperature	76
SEM	scanning electron microscopy	103
SFM	scanning force microscopy	37
SOI	spin-orbit interaction	12
SOT	spin-orbit torque	22
STT	spin-transfer torque	22
TEM	transmission electron microscopy	37
UVL	ultra-violet lithography	38
XRD	x-ray diffraction	36
XRF	x-ray fluorescence	35
XRR	x-ray reflectivity	35

List of Figures

List of Tables